Study of heavy quark production at HERA using the ZEUS microvertex detector

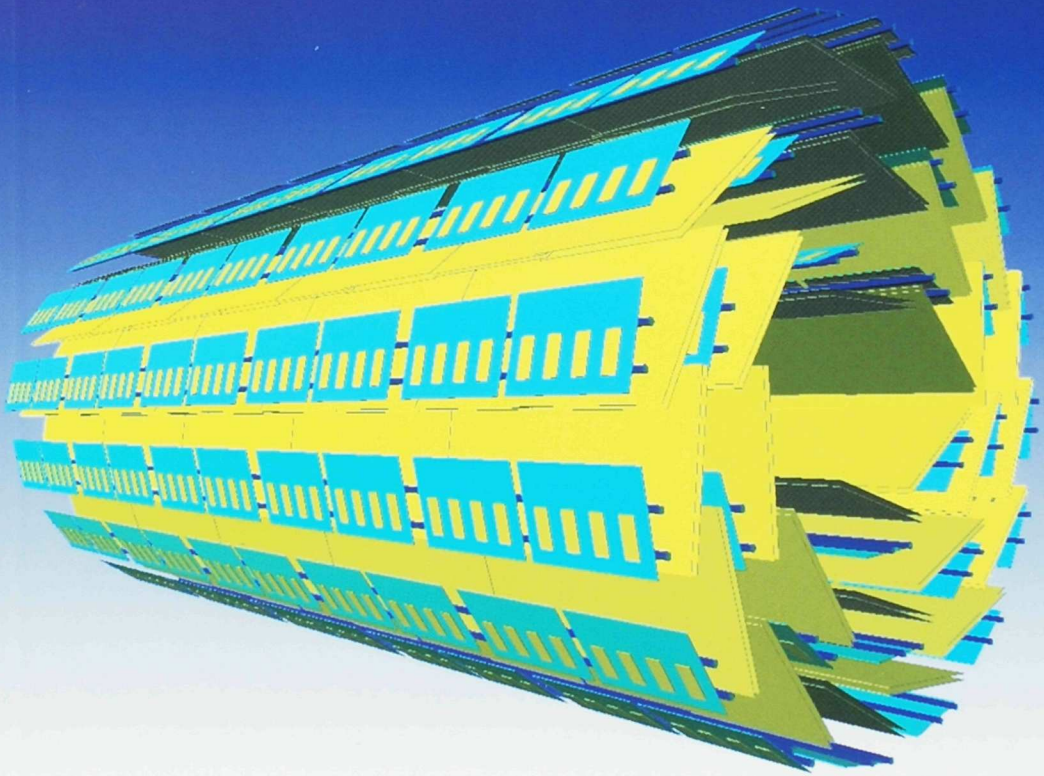

Erik Maddox

Study of heavy quark production at HERA using the ZEUS microvertex detector

Study of heavy quark production at HERA using the ZEUS microvertex detector

ACADEMISCH PROEFSCHRIFT

TER VERKRIJGING VAN DE GRAAD VAN DOCTOR
AAN DE UNIVERSITEIT VAN AMSTERDAM
OP GEZAG VAN DE RECTOR MAGNIFICUS
PROF.MR. P.F. VAN DER HEIJDEN
TEN OVERSTAAN VAN EEN DOOR HET COLLEGE VOOR PROMOTIES
INGESTELDE COMMISSIE, IN HET OPENBAAR TE VERDEDIGEN
IN DE AULA DER UNIVERSITEIT
OP DINSDAG 7 DECEMBER 2004, TE 10:00 UUR

door

Erik Maddox

geboren te Rijnsburg

Promotor: prof.dr. J.J. Engelen
Co-Promotor: dr.ir. E.N. Koffeman

Faculteit der Natuurwetenschappen, Wiskunde en Informatica

ISBN 90-9018-763-4

The work described in this thesis is part of the research programme of 'het Nationaal Instituut voor Kernfysica en Hoge-Energie Fysica' (NIKHEF) in Amsterdam, the Netherlands. The author was financially supported by the University of Amsterdam.

Contents

Introduction **1**

1 Heavy quark production in electron-proton collisions **5**
1.1 Deep inelastic scattering . . . 6
1.1.1 DIS kinematics . . . 6
1.1.2 Structure functions . . . 8
1.1.3 Parton density functions . . . 9
1.2 Heavy quark production at HERA . . . 11
1.3 Properties of charm and bottom hadrons . . . 13
1.3.1 Charmed hadrons . . . 13
1.3.2 Bottom hadrons . . . 15
1.3.3 Fragmentation . . . 15
1.3.4 ZEUS measurements . . . 16
1.4 Conclusion and outlook . . . 17

2 HERA and ZEUS and the upgrade project **21**
2.1 The HERA collider . . . 21
2.2 The ZEUS detector . . . 25
2.2.1 The super conducting solenoid . . . 25
2.2.2 The calorimeter . . . 29
2.2.3 Tracking detectors . . . 31
2.2.4 Trigger, data acquisition and event simulation . . . 36
2.2.5 Measuring the luminosity . . . 39
2.3 Running experience in 2002 and 2003 . . . 40
2.3.1 Backgrounds in the CTD . . . 40
2.3.2 Backgrounds in the MVD . . . 44

3 The ZEUS microvertex detector **47**
3.1 Design . . . 47
3.1.1 Detection principle . . . 48
3.1.2 Layout . . . 51
3.1.3 Readout . . . 54
3.1.4 Cluster and position reconstruction . . . 56
3.1.5 Cooling and cables . . . 60
3.2 Construction . . . 60

3.2.1 Mechanical precision . . . 63
3.2.2 Dead material . . . 66

4 Track fitting **71**
4.1 Track reconstruction . . . 71
4.1.1 Track parameterisation . . . 72
4.1.2 Kalman filter track fit . . . 73
4.1.3 Multiple scattering . . . 82
4.2 Track finding . . . 83
4.3 Vertex reconstruction . . . 84
4.3.1 The full vertex fit . . . 86
4.3.2 The Kalman filter vertex fit . . . 87
4.4 Summary . . . 89

5 Cosmic rays in the MVD **91**
5.1 Introduction . . . 91
5.2 Cosmic ray test before installation . . . 91
5.2.1 Trigger . . . 93
5.2.2 Track fit . . . 93
5.2.3 Residuals, alignment and efficiency . . . 97
5.3 Cosmic rays inside ZEUS . . . 100
5.3.1 Trigger and timing . . . 100
5.3.2 Track fit . . . 104
5.4 Alignment . . . 106
5.5 Monte Carlo comparison . . . 110
5.5.1 Single track Monte Carlo events . . . 110
5.5.2 Hit assignment . . . 110
5.5.3 Track finding . . . 112
5.5.4 Quality of the track fit . . . 114
5.5.5 The track impact parameters . . . 118
5.5.6 Tracks through the MVD wheels . . . 118
5.5.7 Effect of the multiple scattering corrections . . . 122
5.5.8 Transverse momentum resolution . . . 123
5.6 Conclusion . . . 123

6 Charm in the HERA-II data **127**
6.1 Event selection . . . 127
6.1.1 DIS sample . . . 128
6.1.2 Beam spot studies . . . 129
6.1.3 Secondary vertexing . . . 134
6.2 Track selection . . . 135
6.3 $D^{*\pm}$ reconstruction . . . 137
6.3.1 Reconstruction method . . . 138
6.3.2 CTD and MVD comparison . . . 139
6.3.3 Comparison with Monte Carlo simulation and HERA-I data . . . 140

6.4 $D^{\pm}$ reconstruction 142

7 Conclusions **147**

References **149**

Summary **153**

Samenvatting **154**

Acknowledgements **156**

Introduction

In the 20th century enormous progress has been made in the theoretical and experimental understanding of the fundamental forces and the basic building blocks of matter. The four known forces are: gravity, electromagnetism, the weak and the strong (nuclear) force.

Electromagnetism, the weak and the strong interactions are described in the "Standard Model" of particle physics. In brief, this model is "a beautiful scheme with well defined rules, agreeing well with experiment" [1]. In the Standard Model the interactions between particles are described by the exchange of gauge bosons. These are respectively: photon (γ), $W^{\pm}$ or Z boson and gluon (g).

It is well known that atoms have a nucleus, built from protons and neutrons, with electrons circling around it. Particle physics studies sub-nuclear particles (smaller than the size of the nucleus). An elementary particle is defined as having no observable sub-structure. Three classes of elementary particles are known: quarks, leptons and the earlier mentioned gauge bosons. Quarks are found inside hadrons, like the proton and the neutron.

Three types of charged leptons (electron (e), muon (μ) and tau (τ)) and three types of neutral leptons (neutrino (ν)) are known. In total 6 types (flavours) of quarks are known. These are, from the lightest to the heaviest: up (u), down (d), strange (s), charm (c), bottom (b) and top (t). The estimated mass and the quark charges are summarised in table 1. For each particle an anti-particle exists, which has the same mass but opposite charge. For example the positron is the anti-particle of the electron.

light quarks

	u (up)	d (down)	s (strange)
Mass	1.5 to 4.5 MeV	5 to 8.5 MeV	80 to 155 MeV
Charge [e]	2/3	$-1/3$	$-1/3$

heavy quarks

	c (charm)	b (bottom)	t (top)
Mass	1.0 to 1.4 GeV	4.0 to 4.5 GeV	174.3 ± 5.1 GeV
Charge [e]	2/3	$-1/3$	2/3

Table 1: Mass and charge of the six different quark "flavours" [2].

Quarks are not observed directly. They are confined in hadrons[1]. Two types exist: mesons, which are bound states of a quark and an anti-quark ($q\bar{q}$), and baryons, which are bound states of three quarks (qqq). The proton is the lightest baryon with the configuration uud. Recently scientists have claimed that they observe bound states of five quarks [3].

The strong force keeps the quarks together inside hadrons. The theory describing the strong interactions of the Standard Model is quantum chromo dynamics (QCD). In QCD gluon exchange is responsible for the interactions between quarks.

QCD can be tested by scattering electrons off protons. If the energy transfer is large enough the electron scatters off a quark inside the proton. When the quark is kicked out of the proton, the process is called deep inelastic scattering. If the energy involved in the collision is sufficiently high a heavy quark anti-quark pair can be produced.

The first deep inelastic scattering experiments were done in 1969 at the Stanford Linear Accelerator Center (SLAC). Electrons of 7 GeV were collided with a proton in a hydrogen target [4]. At these experiments the structure of the proton was measured for the first time.

To probe the proton even deeper a new particle accelerator was built in Hamburg. Electrons and protons are accelerated up to 27.5 GeV and 920 GeV. Collisions are observed with two detectors, the ZEUS and H1 experiments. In such high energy collisions many particles are produced. The task of the experiments is to measure this complex final state as accurately as possible.

The produced charm and bottom quarks form hadrons, that decay into other particles. The properties (energy, momentum, charge, etc.) of these final state particles are measured with several particle detector components. The measurement of heavy quarks gives additional information about the proton structure and is specifically suited to test QCD calculations.

A recently installed vertex detector allows reconstruction of the actual decay point of some of the heavy hadrons. To separate such a detached track from the interaction point the impact parameter resolution is important. This is the shortest distance from the primary interaction point to the trajectory. The vertex detector is designed to have a track impact parameter resolution of 100 μm. To achieve such a precision all properties of the detector have to be well understood and calibrated.

Thesis outline

This thesis is organised as follows. In chapter 1 an overview is given of the physics of deep inelastic electron-proton collisions. In these collisions heavy quarks are produced, which subsequently form hadrons.

In chapter 2 the HERA accelerator, the ZEUS detector and especially the upgrade programs of both are described. The accelerator and the experiments were modified during summer 2000. The operation of "HERA-II" started in August 2001. The aim was

[1] The top quark decays as $t \to bW^+$, because the top decay time is much shorter than the hadron formation time, no top hadrons have been observed.

to reach a higher luminosity (more collisions per second). The start up was slowed down because of beam related background problems which took up to the end of 2003 to be solved.

The ZEUS collaboration designed and constructed a microvertex detector (MVD). In chapter 3 the design, readout and assembly of this microvertex detector are explained in detail.

A track finding and fitting algorithm was developed for the vertex detector. The new track fit makes use of the Kalman filter. In chapter 4 the fit is described in detail, including the treatment of scattering of charged particles in the detector material. After the tracks are fitted they are combined to vertices. The used vertex algorithm, also based on the Kalman filter, is described at the end of chapter 4.

The performance of the microvertex detector is evaluated in chapter 5. First, results from the pre-installation system test are presented. Secondly its performance after installation is discussed using data from cosmic runs. Results are compared with a Monte Carlo simulation.

The first HERA-II beam data (up to April 2004) is studied in chapter 6. The track fit and the vertex fit from chapter 4 are applied to find a signal of charmed hadrons. In chapter 7 conclusions are presented.

Chapter 1

Heavy quark production in electron-proton collisions

The measurement of heavy quarks in high energy collisions results in valuable experimental data to study the strong interactions of the Standard Model. The strong interactions between quarks and gluons are described by Quantum Chromo Dynamics (QCD). The dynamics of quarks and gluons are calculable with perturbation theory (pQCD), provided that the scale of the interaction is larger than the fundamental cut-off value $\Lambda_{\mathrm{QCD}} \approx 200\,\mathrm{MeV}$. The masses of heavy quarks are above Λ_{QCD} (while the light quarks are not). Hence, the production of heavy quarks can be treated completely perturbatively.

In particular deep inelastic electron proton scattering is a clean environment to study heavy quark production. The quarks in the proton are "probed" directly by the exchange of electroweak gauge bosons. The produced heavy quark is related to the "hard QCD process".

The main QCD production process for heavy quarks in ep scattering is boson-gluon fusion, and this process strongly depends on the gluon density of the proton. The gluon density is determined indirectly, from the scaling violation of the proton structure function.

For the c (charm) and b (beauty or bottom) quarks the masses are $m_c \approx 1.3\,\mathrm{GeV}$ and $m_b \approx 4.5\,\mathrm{GeV}$. The production ratio is approximately 200:1. The mass and the charge of the b quark decrease the production rate.

After the initial heavy quark is produced it fragments into hadrons. (No free quarks are observed in nature.) Most of these hadrons are very instable and decay shortly after production. Some travel just far enough to allow a measurement of the distance between the decay point and the production point.

In this chapter the production of heavy quarks (c and b) is discussed, after a brief introduction to deep inelastic ep scattering and proton structure functions. The experimental signatures of heavy quarks are studied in the last section.

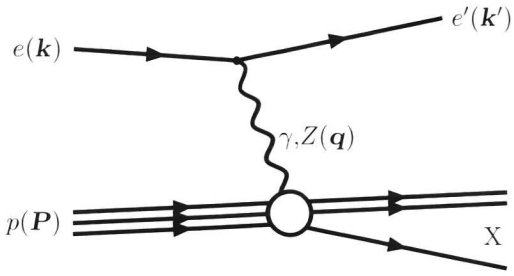

Figure 1.1: *ep* scattering at HERA: an electron (e) exchanges a photon (γ) which scatters off a constituent of the proton (p). The final state consists of the scattered electron, the proton remnant and a scattered quark.

1.1 Deep inelastic scattering

The dynamics of deep inelastic *ep* scattering (DIS) depend on the internal structure of the proton. This structure can be represented by so called form factors or structure functions. Analysis of the structure functions, mostly from fits of the data, results in parton density functions, which describe the content of the proton in the context of different quark flavours and the gluon.

1.1.1 DIS kinematics

At HERA electrons[1] and protons collide at high energies. The scattering process is called elastic, if the proton stays intact, otherwise the scattering is called inelastic. The elasticity of the scattering depends on the momentum transfer from the electron to the proton. Breakup of the proton is interesting to study, because it reveals the internal structure: the incoming lepton can be viewed as a source of gauge bosons that resolves the composite hadron.

The scattering process can be characterised by the type of the exchanged gauge boson: in neutral current events photons or Z bosons are exchanged, where due to interference effects no clear separation is possible, while in charged current events the electron emits a W^- boson and the scattered lepton is in this case a neutrino.

In figure 1.1 a diagram of neutral current (NC) DIS *ep* scattering is drawn. In the diagram an electron scatters off a quark in the proton. The final state consists of a scattered electron, a scattered quark and the proton remnant. The squared four-momentum transfer from the electron to the proton is:

$$\boldsymbol{q}^2 = (\boldsymbol{k} - \boldsymbol{k}')^2 \equiv -Q^2, \tag{1.1}$$

where $\boldsymbol{q}$, $\boldsymbol{k}$ and $\boldsymbol{k}'$ denote the four momentum of the exchanged gauge boson and of the incoming and outgoing electron respectively.

[1] In fact, both electrons and positrons can be stored in HERA. Here the electron case is discussed. The situation is similar for positrons.

In optics the resolving power depends linearly on the wave length of the light source. Equivalently, the wave length ($\hbar c/|\boldsymbol{q}|$) of the exchanged gauge boson describes the resolving power available for probing the proton's internal structure. Viewed in this way HERA is a microscope to study the constituents of the proton.

The Q^2 of a scatter (or event) gives a physical scale to distinguish three different regimes at HERA:

- $Q^2 < 1\,\mathrm{GeV}^2$ (photoproduction, or not DIS)

  The propagator of the gauge bosons is proportional to $1/(Q^2 + M^2)$. The exchange of $Z(W^\pm)$ bosons which have a rest mass of 80.2(91.2) GeV is therefore heavily suppressed. The $1/Q^2$ dependence for the exchange of photons makes photoproduction the dominating scattering process at HERA. Photoproduction events can be used to study the hadronic structure of the photon arising from the fluctuation of a photon into a quark anti-quark pair ($\gamma \to q\bar{q}$).

- $1\,\mathrm{GeV}^2 < Q^2 < 100\,\mathrm{GeV}^2$ (DIS at moderate Q^2)

  This is the regime where most HERA measurements concerning the structure of the proton are performed. The scattering cross section is still large and the contribution of the Z exchange can be neglected. At this momentum transfer photon fluctuations are strongly suppressed.

- $Q^2 > 100\,\mathrm{GeV}^2$ (DIS at high Q^2)

  The cross section expected from the Standard Model becomes small in this regime. These data (only available at HERA) are useful to examine the existing theories or to discover new phenomena. For $Q^2 \approx M_Z^2 \approx 8300\,\mathrm{GeV}^2$ the charged and neutral current interaction become comparable in strength.

The squared centre of mass energy s of the reaction is given by the initial state:

$$s = (\boldsymbol{P} + \boldsymbol{k})^2 \approx 4E_e E_p, \tag{1.2}$$

where $\boldsymbol{P}$ and E_p denote the four-momentum and the energy of the incoming proton. The approximation neglects the masses of the proton and the electron. At HERA a centre of mass energy $\sqrt{s} = 318\,\mathrm{GeV}$ is achieved.

Besides Q^2 and s the kinematics of the scattering process are fully determined by one additional variable. Convenient choices are either the inelasticity y or the so called Bjorken x_{Bj} variable:

$$y = \frac{\boldsymbol{P}\cdot\boldsymbol{q}}{\boldsymbol{P}\cdot\boldsymbol{k}}, \quad x_{\mathrm{Bj}} = \frac{-\boldsymbol{q}^2}{2\boldsymbol{P}\cdot\boldsymbol{q}}. \tag{1.3}$$

The variables are related through:

$$Q^2 = x_{\mathrm{Bj}} y s. \tag{1.4}$$

In the proton rest frame y represents the fraction of four momentum transfered from the electron to the proton. x_{Bj} can be interpreted as the fraction of the proton four momentum carried by the struck parton.

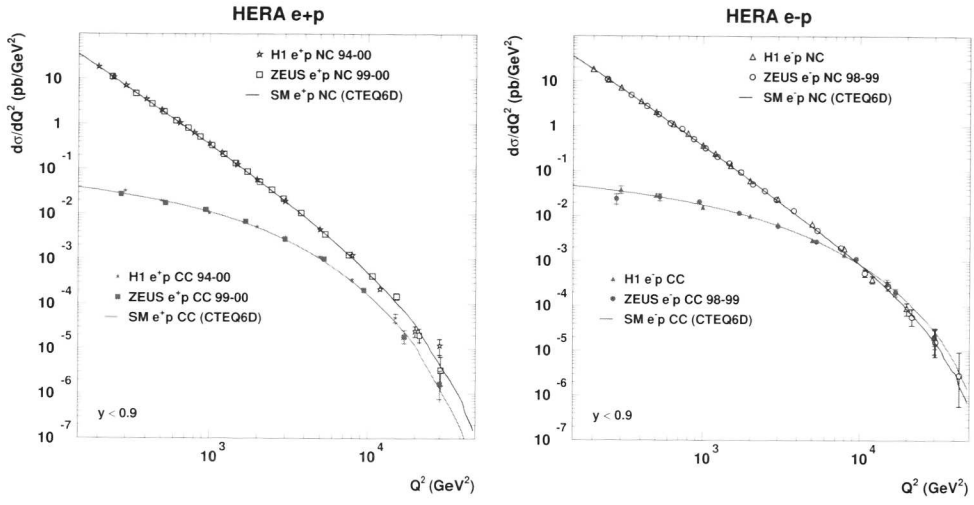

Figure 1.2: The HERA measured neutral current and charged current high Q^2 cross sections. The left plot shows the cross sections for e^+p data and the right plot for e^-p data. The data are compared with the standard model predictions.

There are several experimental methods to determine the ep scattering kinematics. They rely on the angle and energy measurement of the scattered lepton and the so called hadronic system.

Figure 1.2 shows the neutral and charged current cross sections for deep inelastic e^+p and e^-p scattering in bins of Q^2. It is seen that the cross sections decrease rapidly and for high Q^2 the charged current cross section and the neutral current cross section become similar. This is the effect of the electromagnetic and the weak force reaching comparable strength. The measurements at high Q^2 have the largest experimental errors. The ep cross sections also depend on the structure of the proton. This is described in the next section.

1.1.2 Structure functions

A detailed overview of deep inelastic scattering and structure functions can be found elsewhere [5]. The neutral current $e^\pm p \to e^\pm X$ unpolarised cross section is:

$$\frac{d^2\sigma_{\mathrm{NC}}(e^\pm p)}{dxdQ^2} = \frac{2\pi\alpha^2}{xQ^4}\left[Y_+F_2(x,Q^2) - y^2F_L(x,Q^2) \mp Y_-xF_3(x,Q^2)\right], \tag{1.5}$$

where $Y_\pm = 1 \pm (1-y)^2$. In this equation α denotes the electromagnetic coupling constant. The longitudinal structure function, F_L, describes the coupling of the proton to longitudinally polarised virtual photons. The parity violating structure function xF_3 arises from

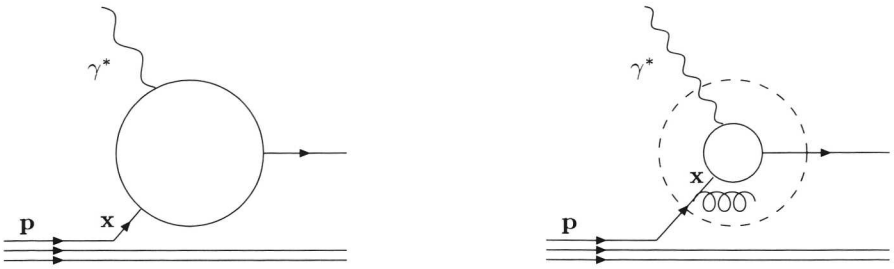

Figure 1.3: The Q^2 evaluation is schematically shown. At higher Q^2 smaller distances are resolved, consequently the probability to scatter on a low x quark increases.

the weak Z boson exchange. At low Q^2 the contribution of the weak interactions is negligible.[2]

When the above ep cross section is compared to the cross section of an electron scattering on a free quark ($eq \rightarrow eq$) it is found that F_2 can be interpreted as

$$F_2(x) = \sum_q e_q^2(xq(x) + x\bar{q}(x)), \tag{1.6}$$

where $q(x)$ are the quark momentum densities inside the proton of the different quark flavours (u, d, s) and e_q are their charges. Because the quarks are spin 1/2 particles, $F_L = 0$ (for massless quarks and leading order).

Probing of the proton with a virtual photon with increasing Q^2 is similar to decreasing the wavelength of the probe. This is depicted schematically in figure 1.3. Quarks can emit or absorb gluons and gluons can fluctuate into quark anti-quark pairs. (The gluon can even interact with itself). These fluctuations take place on very short time/distance scales. So at higher Q^2, more of these fluctuations can be observed. Furthermore the fluctuating partons have a smaller momentum fraction, hence more low x partons are observed. This mechanism is known as the violation of scaling and leads to a steeply increasing structure function at low x (see figure 1.4 [2]).

The evolution (in Q^2) of the quark and gluon density is described theoretically with the DGLAP evolution equations [7]. Input for the DGLAP formalism are the quark and gluon splitting functions which are known for leading order and next-to-leading logarithmic contributions.

1.1.3 Parton density functions

The quark density functions are also known as the parton density functions (PDFs) of the proton. The PDFs are not calculable from theory and have to be obtained from experiments. Partons are both the gluons and quarks in the proton. Since the gluons do not couple electroweakly they are not probed directly. They can be observed indirectly,

[2]This follows from the fact that the propagator for single Z exchange is $1/(Q^2 + M_Z^2)$ and M_Z is 91.2 GeV.

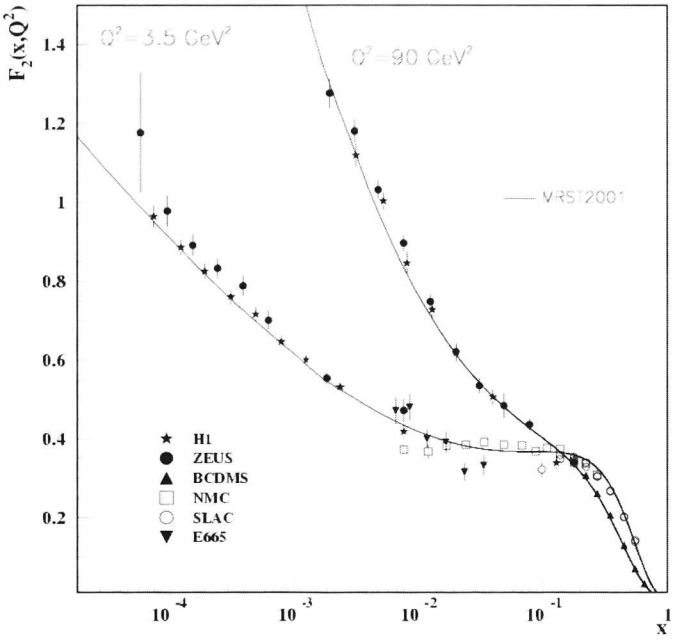

Figure 1.4: The proton structure function F_2 given at two Q^2 values ($3.5\,\mathrm{GeV}^2$ and $90\,\mathrm{GeV}^2$), which exhibit scaling at the "pivot" point $x \sim 0.14$. The data are compared with the MRST prediction [6].

through the violation of scaling. Approximately 50% of the proton momentum is carried by the gluons. Precise knowledge of the parton density functions is important for calculating reliable cross sections.

In the most simple model, the "static" quark parton model, the proton is only built from three quarks (uud): the valence quarks, which carry the quantum numbers of the proton. In improved parton models these quarks can radiate gluons and the gluons can split into quarks and anti-quarks. The radiated quarks are called the sea quarks.

The structure functions depend on the parton density functions. From the measured proton structure function the parton densities can be derived. The approach is to parametrise the parton density functions as a function of x. The following equation is often used:

$$xf(x) = p_1 x^{p_2}(1-x)^{p_3}(1 + p_4\sqrt{x} + p_5 x). \tag{1.7}$$

Furthermore there are other constraints. For example the number of u quarks is twice the number of d quarks and in the sea the number of quarks and anti-quarks is equal.

Subsequently the parameters are fitted to the structure function data. This is done by minimising the following χ^2 equation:

$$\chi^2 = \sum_i \frac{[F_i(p) - F_i(meas)]^2}{\sigma^2_{i,\mathrm{tot}}}. \tag{1.8}$$

The symbol $F_i(meas)$ represents a measured data point. The symbol $F_i(p)$ represents the prediction from next-to-leading order QCD in terms of the fit parameters. This is non-trivial because one has to consider: electroweak mixing, next-to-leading order splitting functions and the treatment of heavy quarks. On the experimental side one has to propagate all measurement errors correctly and in reality a more complex χ^2 definition is used.

Such fits are also performed by the ZEUS collaboration [8]. The results for $Q^2 = 10\,\mathrm{GeV}^2$ are shown in figure 1.5. The figure shows that the u_v and d_v distributions dominate a high x. The error band represents the uncertainty. The sea quarks ($q\bar{q}$ fluctuations) and the gluons become dominant at low x. The results are compared with PDFs from several PDF fitting groups, MRST [6] and CTEQ [9]. Both MRST and CTEQ use the available world ep, νp and pp scattering data to determine the parton density functions. The differences are due to the use of different input data sets, heavy quark mass effects and the gluon parametrisation [9].

1.2 Heavy quark production at HERA

While the u, d and s quarks have masses below the Λ_{QCD} parameter, the masses of the heavy quarks are already sufficient to serve as a hard scale for perturbative calculations. At HERA the produced heavy quarks are c and b quarks. The t (top) quark is out of reach because of its large mass. The following discussion focuses on charm production, but is also applicable for beauty production.

In figure 1.6 the leading order boson-gluon fusion (BGF) diagram is shown which is the main production mechanism of charm in deep inelastic scattering. In BGF a photon

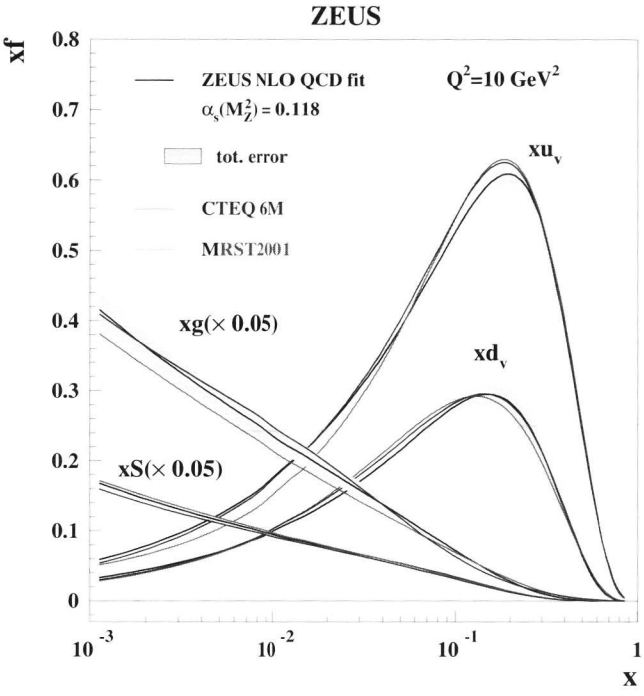

Figure 1.5: The gluon, sea, u and d valence distributions extracted from the standard ZEUS NLO QCD fit at $Q^2 = 10\,\mathrm{GeV}^2$. The error bands show the uncertainty. The ZEUS fit is compared with the MRST and CTEQ fits.

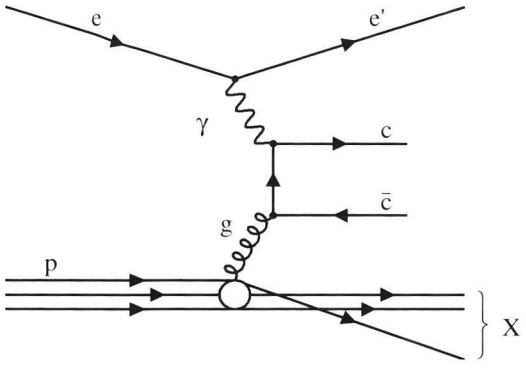

Figure 1.6: The dominant charm production mechanism at HERA is shown: a photon (γ) emitted by the electron (e) and a gluon (g) originating from the proton (p) form a $c\bar{c}$ pair. This process is called boson-gluon fusion (BGF).

interacts with a gluon in the proton to form a charm anti-charm pair. Because the proton serves as a source of gluons, charm production at HERA is sensitive to the gluon density inside the proton.

The cross section for charm production in DIS follows directly from equation 1.5, which can be restricted to the charm only case:

$$\frac{d^2\sigma^{c\bar{c}}}{dxdQ^2} = \frac{2\pi\alpha^2}{xQ^4}\left[(1+(1-y)^2)F_2^{c\bar{c}}(x,Q^2) - y^2F_L^{c\bar{c}}(x,Q^2)\right], \tag{1.9}$$

where the inclusive structure functions have been replaced by the charm specific functions. The charm structure functions dependence on the parton densities (specifically the gluon density) are known to next-to-leading order [10].

The production rate of c quarks is a factor 200 larger than for b quarks. The b quark is heavier and F_2 depends on the charge squared of the quark. The b quark has charge $-1/3e$ and the c quark has charge $+2/3e$, where e is the electron charge. The total charm cross section for $ep \to ec\bar{c}$ plus anything, at a centre-of-mass energy of $\sqrt{s} = 318\,\text{GeV}$, is of the order of $0.5\,\mu\text{b}$. For beauty production it is about 1 nb.

The parton density functions, including the gluon density are input for QCD predictions of heavy quark cross sections and dynamics. These can be observed in the experiment. Hence, the measurement of heavy quarks provides a powerful check on the validity of QCD.

1.3 Properties of charm and bottom hadrons

The cross section of the hard scatter, which produces the c and b quarks, is calculated with perturbative QCD. In experiments the quarks are observed as hadrons (mesons and baryons) which are produced in the hadronisation or fragmentation process.

For the hadronisation process perturbative QCD is not applicable. Therefore, predictions on hadron level rely on data from previous experiments and on empirical models. In this section the fragmentation ratios of c and b quarks to certain hadrons are discussed. Also the Peterson parametrisation, which describes the momentum transfer from the quark to the hadron is discussed.

1.3.1 Charmed hadrons

The produced charm quarks fragment into charmed hadrons. The fragmentation of c quarks is shown schematically in figure 1.7. The numbers indicate the branching ratios. Charmed hadrons are D^+, D^0, D_s^+ mesons and the charmed baryon Λ_c (excited states are also observed). The excited state D mesons are written as D^*. The important properties (mass, lifetime) of the different charmed hadrons are summarised in table 1.1. Also the branching fraction for the clearest observable decay channel is given.

Rather than looking at these exclusive hadronic channels, final states can be studied, where the charm quark decays to an electron. This is called the semi-leptonic decay of the charmed hadron, for example $c \to se^+\nu_e$ (and c.c.). In the spectator model the c quark

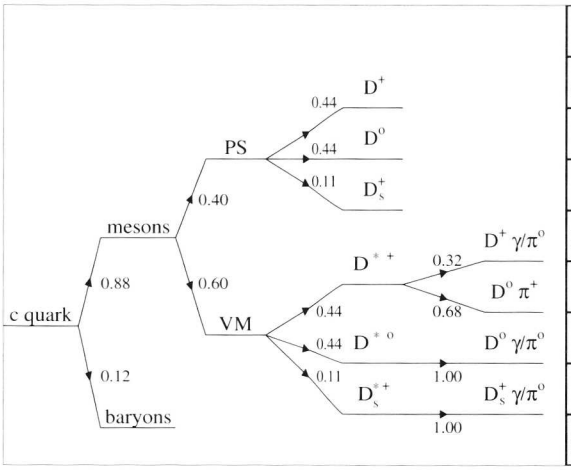

D+	D0	D+s
0.156		
	0.156	
		0.040
0.076		
	0.159	
	0.234	
		0.061
0.232	0.549	0.101

Figure 1.7: The charm quark fragmentation tree into D and D^* mesons is shown. In addition the decay channels of the spin excited D^* mesons are given. The charm fragmentation ratios are from reference [11] and the branching ratios of the D^* mesons are from reference [12]. The table to the right sums the contributions of the directly and indirectly produced scalar mesons to their $f(c \to D)$ factors.

charm hadrons properties	D^+	D^0	D_s^+	D^{*+}	Λ_c^+
valence quarks	$c\bar{d}$	$c\bar{u}$	$c\bar{s}$	$c\bar{d}$	udc
mass [GeV]	1.869	1.865	1.969	2.010	2.285
$c\tau$ [μm]	315	123	147	-	60
$f(c \to D, \Lambda)$ [%]	23.2	54.9	10.1	23.5	7.6
$f(b \to D)$ [%]	23.7	60.5	18	17.3	
decay channel	$K^-\pi^+\pi^+$	$K^-\pi^+$	$\phi\pi^+$ $\phi \to K^+K^-$	$D^0\pi^+$ $D^0 \to K^-\pi^+$	$pK^-\pi^+$
branching fraction [%]	9.1	3.8	1.8	2.6	5.0

Table 1.1: The table summarises the D meson and Λ_c^+ properties. For each hadron the channel with the clearest signature is given.

bottom hadrons properties	B^+	B^0	B_s^0	B_c^+	Λ_b^0
valence quarks	ub	db	sb	cb	udb
mass [GeV]	5.279	5.279	5.369	6.4	5.624
$c\tau$ [μm]	495	468	438	138	369
$f(b \to B, \Lambda)$ [%]	38.8	38.8	10.6		11.8 (*)

(*) The fraction b to baryons is 11.8%

b meson decay	$e^+\nu_e X$	$\mu^+\nu_\mu$	$\tau^+\nu_\tau$	$\bar{D}^0 X$	$D^- X$	$D^{*+} X$
branching fraction [%]	10.9	11.0	2.5	60.9	23.5	17.3

Table 1.2: The tables summarises B meson and Λ_b^0 properties.

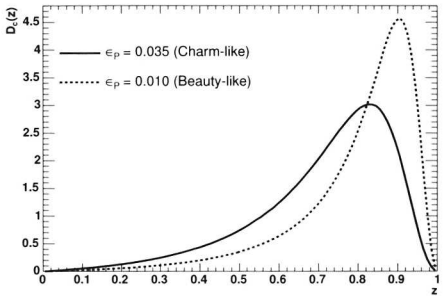

Figure 1.8: The normalised Peterson fragmentation function for charm and beauty fragmentation. The value for the ϵ_P follows from experimental data.

of the hadron decays in an s quark. The composition of the hadron is then changed and also a positron and a neutrino appear in the final state. The average branching ratio is 11% [13].

1.3.2 Bottom hadrons

Bottom or beauty hadrons consist of at least one b valence quark. The properties of the B mesons and the Λ_b^0 are summarised in table 1.2. The bottom hadrons are heavier and have a longer average $c\tau$ than charmed hadrons.

The b quark decays predominantly weakly to a c quark. A charmed hadron is then formed. The study of a particular hadronic decay channel can only be done with a low branching ratio (lower than 1%). The semi-leptonic decay $b \to cl^+\nu_l$ where the lepton is an electron or a muon (or a τ) has a branching fraction of about 10% (2.5%).

1.3.3 Fragmentation

When a hadron carries a large part of the parent quark momentum, the fragmentation is called "hard". In order to model the momentum distribution of the meson with the c or

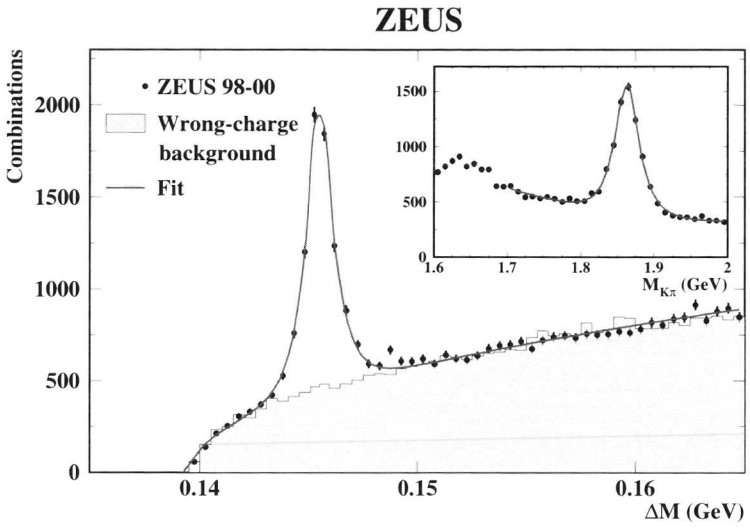

Figure 1.9: The distribution of the mass difference, $\Delta M = (M_{K\pi\pi_s} - M_{K\pi})$, for $D^{*\pm}$ candidates (solid dots). The ΔM distribution from wrong-charge combinations, normalised in the region $0.15 < \Delta M < 0.165\,\mathrm{GeV}$, is shown as a histogram. The solid line shows the result of the fit described in the text. The $M_{K\pi}$ invariant mass distribution is shown as an inset. The fit is the sum of a modified Gaussian to describe the signal and a second order polynomial to describe the background. [15]

b quark, the fragmentation function is used. The fragmentation function is derived from experimental data. It describes the momentum fraction of the hadron with respect to the initial quark. One of the commonly used parametrisations is the Peterson function [14]:

$$f(z) = \frac{1}{z(1 - 1/z - \epsilon_P/(1-z))^2}. \tag{1.10}$$

This model only depends on one parameter: ϵ_P. In figure 1.8 the Peterson function is drawn for charm and beauty fragmentation. Beauty fragmentation is in general harder. From measurements at different experiments fragmentation seems universal.

1.3.4 ZEUS measurements

In this section two results from ZEUS on charm and bottom production in DIS are discussed.

Charm production in DIS

The well known method to study charm production is the reconstruction of the decay $D^{*+} \to D^0\pi_s^+$ with the subsequent decay $D^0 \to K^-\pi^+$. The small mass difference (ΔM) between the D^0 and the D^{*+} gives a clean signal to count the number of produced D^{*+}

mesons. Figure 1.9 shows the ΔM signal for ZEUS DIS events [15] from HERA data recorded until 2000.

From these data the structure function $F_2^{c\bar{c}}$ has been derived. The results are presented in figure 1.10. The data are well described by the theory curves. The experimental errors are still large. For increasing Q^2 and decreasing x, we see $F_2^{c\bar{c}}$ rising, as expected from the proton gluon density increase.

Bottom production in DIS

Measurements of b quark production have been done for the semi-leptonic decay channels e and μ [16, 17]. The b quark is assumed to decay to a lepton and a jet of other hadrons. The variable under study is then the transverse momentum of the lepton with respect to the jet axis ($p_{t,rel}$). The large mass of the decaying b quark gives the lepton on average a larger $p_{t,rel}$ than a lighter quark would do.

With the help of Monte Carlo programs the shapes of the $p_{t,rel}$ distributions are studied. This results in a $p_{t,rel}$ shape for light, charm and beauty quarks. These templates are used to determine the fraction of the light, charm and beauty component of the data.

The fraction of b quarks decaying to muons in DIS has been determined [17]. From this the b quark cross section has been calculated for a few bins in x and Q^2. The results are presented in figure 1.11. The data are compared with NLO calculations and leading order Monte Carlo programs RAPGAP and CASCADE. The measurements and the predictions do not agree for all the bins.

1.4 Conclusion and outlook

The measurements at HERA have already provided a large amount of data on the structure of the proton and about quantum chromo dynamics. When probing the proton at higher Q^2 it turns out that the proton consists of a quark and gluon sea. With QCD we can describe most of the cross section measurements. The ZEUS results show that for high Q^2 and for heavy flavour measurements the experimental uncertainty is still large.

A larger data sample of high Q^2 events would be useful for more stringent tests of the theory. The installation of a microvertex detector would provide better and additional methods to tag heavy quark production.

In the following chapters is described how the ZEUS detector has been improved to profit from the second phase of HERA data.

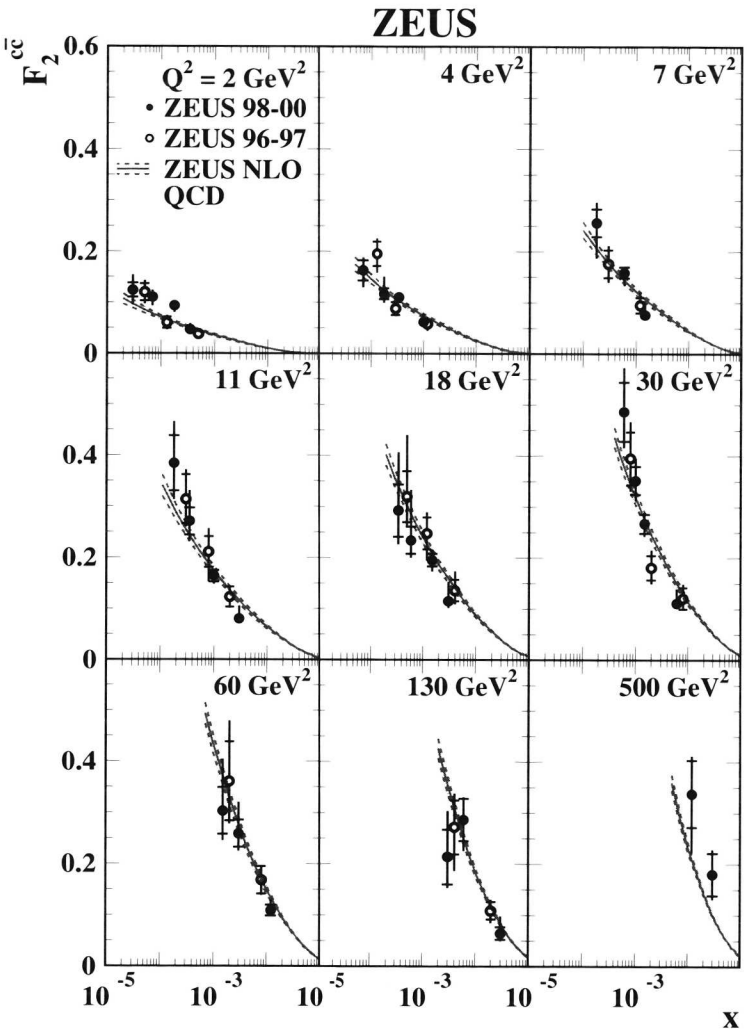

Figure 1.10: The measured $F_2^{c\bar{c}}$ at Q^2 values between 2 and 500 GeV^2 as a function of x. The current data (solid points) are compared with the previous ZEUS measurement (open points). The data are shown with statistical and systematic uncertainties added in quadrature (outer bars). The lower and upper curves show the fit uncertainty propagated from the experimental uncertainties of the fitted data.

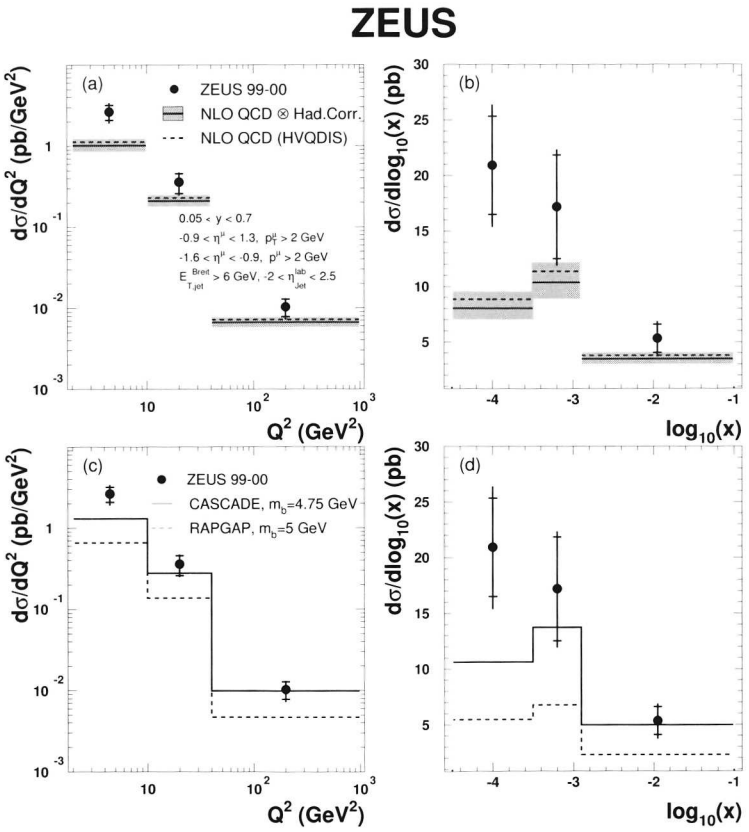

Figure 1.11: Differential b quark cross section as a function of Q^2 (a) and Bjorken x (b) for events with at least one jet reconstructed in the Breit frame and a muon, compared to the NLO calculations. The error bars on the data correspond to the statistical uncertainty (inner error bars) and systematic uncertainty added in quadrature (outer error bars). The solid lines show the NLO QCD prediction including hadronisation corrections and the dashed line the same calculation without hadronisation corrections. The shaded band shows the uncertainty of the NLO QCD prediction due to the variation of the factorisation and the renormalisation scale, μ, and the b quark mass, m_b. Figures (c) and (d) present the differential b quark cross sections as a function of Q^2 and Bjorken x compared with LO QCD MC programs CASCADE (solid line) and RAPGAP (dashed line).

Chapter 2

HERA and ZEUS and the upgrade project

In this chapter the HERA electron-proton collider is described. The ZEUS experiment is one of the four HERA experiments. The layout and the instrumentation of the ZEUS detector is also presented.

HERA has delivered in total an integrated luminosity of $120\,\mathrm{pb}^{-1}$ in the years 1991 to 2000. To enhance the luminosity an upgrade of the accelerator was foreseen for 2001. For this reason a one year long shutdown was necessary, that started in the fall of 2000. To profit from the HERA upgrade, the ZEUS experiment also made an upgrade plan. A summary of the resulting modifications is given in this chapter.

The startup of HERA-II, in the summer of 2001, came with various unexpected problems. As a consequence only a small sample of data was collected until the end of 2003. More details can be found in the last section of this chapter.

2.1 The HERA collider

The HERA collider is a unique particle accelerator for the study of high energy electron-proton (ep) collisions. The HERA ring is located at the research centre DESY in Hamburg, Germany. The HERA ring is located inside a tunnel with a circumference of 6.3 km and approximately 30 m below ground level. Figure 2.1 shows an aerial view of (a part of) Hamburg with the locations of the HERA tunnel and the experimental halls.

A schematic drawing of the HERA accelerator complex is given in figure 2.2. After passing a chain of pre-accelerators, electrons and protons are injected in opposite directions into two separate rings, where they are accelerated to their final energies of 27.5 GeV (electrons) and 920 GeV (protons). The beams can be stored for several hours, during this period collisions can be made. The beams are not continuous but are concentrated in a number of bunches.

These bunches of electrons and protons are brought into collision in the interaction regions of the H1 and the ZEUS experiment. Every 96 ns two bunches cross, corresponding to a maximum collision rate of 10.4 MHz. Table 2.1 summarises the main HERA parameters.

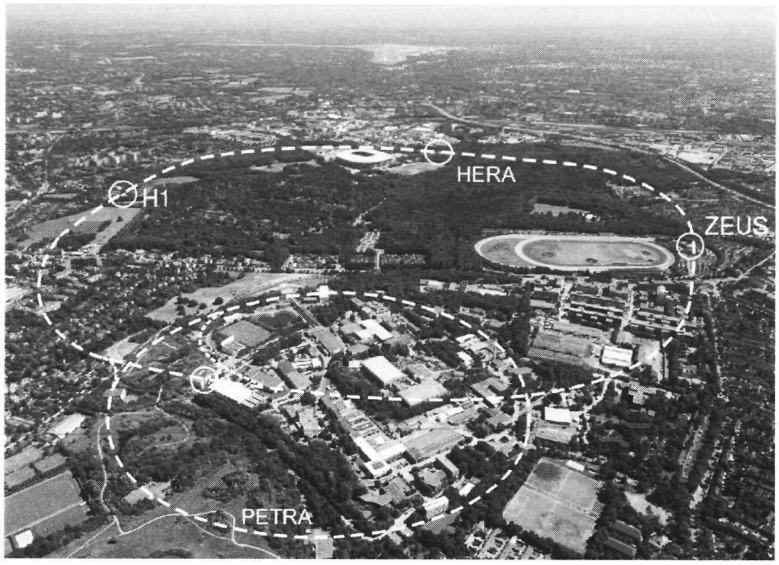

Figure 2.1: View from the sky of the DESY laboratory grounds in the city of Hamburg. The location of the HERA tunnel is marked.

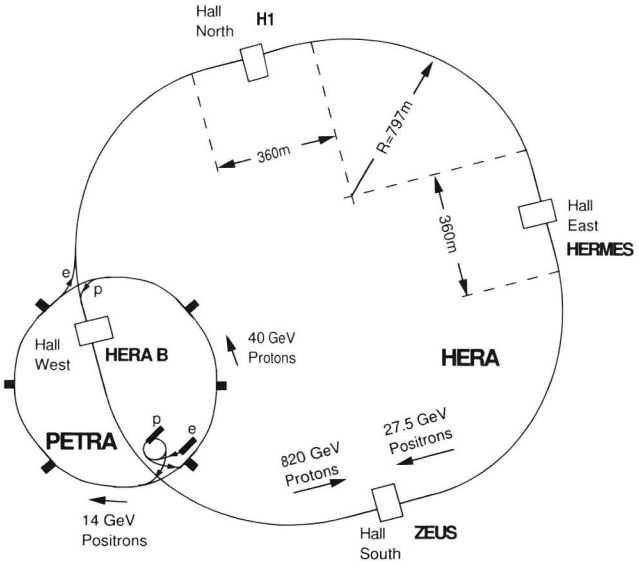

Figure 2.2: Schematic drawing of the HERA electron-proton collider. Until 1997 the HERA proton beam was accelerated up to 820 GeV. Starting from 1998 the proton beam energy has been 920 GeV.

Tunnel circumference	6336.83 m		
Bunch spacing (in time)	96 ns		
Bunch spacing (in distance)	28.8 m		
Number of buckets	220		
Beam crossing angle	0 mrad		
	Design	2000	Upgrade
Centre of mass energy [GeV]	313.7	318	318
Number of colliding bunches	210	174	174
Peak luminosity $[\mathrm{cm}^{-2}\,\mathrm{sec}^{-1}]$	$1.5 \cdot 10^{31}$	$1.5 \cdot 10^{31}$	$7.5 \cdot 10^{31}$
Specific luminosity $[\mathrm{cm}^{-2}\,\mathrm{sec}^{-1}\,\mathrm{A}^{-2}]$	$3.4 \cdot 10^{29}$	$7.4 \cdot 10^{29}$	$1.8 \cdot 10^{30}$
Integrated luminosity $[\mathrm{pb}^{-1}\mathrm{y}^{-1}]$	50	70	150
max. I_p [mA]	160	95	140
max. I_e [mA]	58	45	58
$\beta_x^*(\beta_y^*)$ p-ring [mm]	10.0(1.0)	7.0(0.5)	2.45(0.18)
$\beta_x^*(\beta_y^*)$ e-ring [mm]	2.2(0.9)	0.90(0.60)	0.63(0.26)
Width of interacting beams [mm]	0.247	0.190	0.120
Height of interacting beams [mm]	0.078	0.050	0.030

Table 2.1: HERA collider parameters from the original design, the performance during the year 2000 and the goals for the luminosity upgrade.

The key parameter of particle colliders is the *luminosity* $\mathcal{L}$. The luminosity is defined as the number of collisions per unit area and per unit time $[\mathrm{cm}^{-2}\,\mathrm{sec}^{-1}]$. The *specific luminosity* is the luminosity divided by the beam currents $[\mathrm{cm}^{-2}\,\mathrm{sec}^{-1}\,\mathrm{A}^{-2}]$. The specific luminosity quantifies the intrinsic quality of the colliding beams. The *integrated luminosity* is the luminosity summed over a given period of time $[\mathrm{cm}^{-2}]$.

In particle physics the probability for a given process (cross section) is expressed in pb. ($[1\,\mathrm{pb}] = [10^{-36}\,\mathrm{cm}^2]$ and $\mathcal{L}$(integrated) in pb^{-1}). To calculate the number of occurrences (events) of a process with cross section σ the following equation is used:

$$N = \sigma \times \mathcal{L}(\text{integrated}). \tag{2.1}$$

From the previous equation it is seen that the higher the luminosity, the larger is the event rate for a given process. High luminosity is obtained by optimising the transverse size of the beams, the number of particles per bunch, the lifetime of the beams and the number of bunches in the machine:

$$\mathcal{L} = f\frac{n_1 n_2}{4\pi\sigma_x\sigma_y}, \tag{2.2}$$

where n_1 particles collide on n_2 particles with frequency f and where σ_x and σ_y are the Gaussian transverse beam profiles in the x and y direction [12].

Usually the beam size is expressed in term of the transverse emittance ϵ, denoting the beam quality, and the amplitude function β, determined by the magnet configuration. The emittance, the β-function and the beam width are related through:

$$\epsilon = \frac{\pi\sigma_x\sigma_y}{\beta}. \tag{2.3}$$

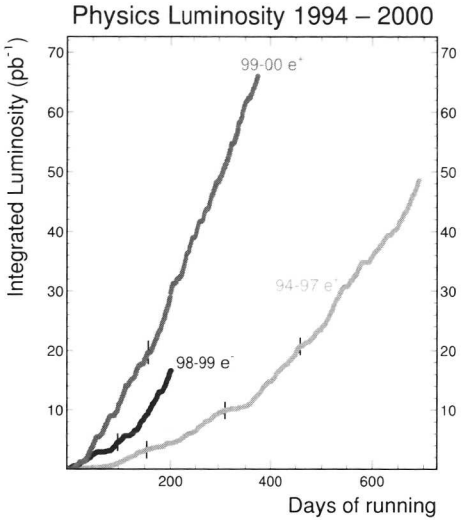

Figure 2.3: Integrated luminosity for the three data samples recorded by ZEUS until 2000. The average data taking efficiency is 70%.

The first ep collisions in ZEUS were observed in 1992 [18]. The ZEUS data sample can be divided in three periods. One short period with e^-p running and two large ones with e^+p running. Figure 2.3 shows the integrated luminosity that is useful for physics analysis for these three periods.

In the year 2000 the design value of $L = 1.5 \cdot 10^{31}\,\mathrm{cm}^{-2}s^{-1}$ was routinely surpassed at the start of a luminosity fill. However, for a substantial further increase large modifications of the interaction regions were unavoidable.

To reach a total luminosity of $1\,\mathrm{fb}^{-1}$ an upgrade project was planned. The choice was made to decrease the β-functions at the interaction point. This means that the focusing of the beam becomes stronger and that the transverse region of the interacting beams becomes smaller. Also spin-rotators were installed to polarise the lepton beam longitudinally. Polarisation is outside the scope of this thesis.

In the old focusing scheme the first proton quadrupole was at a distance of 26 m from the interaction point (IP). In order to focus the proton beam more strongly these magnets had to be moved closer to the experiments requiring an earlier magnetic separation of the electron and proton beam. The new machine lattice around the IP is shown in figure 2.4a. Key elements are:

- New half-quadrupoles (GM) at $\pm 11\,\mathrm{m}$ from the IP. A modified (thinner) mirror plate allows protons to be focused without large disturbance on the electron beam which is only 7 cm away.

- Two super conducting magnets (GO and GG) inside the experiments. These mag-

Inner radius	0.875 m
Outer radius	0.957 m
Length	2.460 m
Magnetic field (B_z)	1.43 T
Thickness in radiation lengths	0.9
Operating temperature	4.5 K

Table 2.2: Parameters for the ZEUS solenoid.

nets perform the final focusing of the proton and electron beam.

The reduction of the e beam bending radius from 1200 m to 400 m results in a significantly increased amount of synchrotron radiation. At the design value of 58 mA electron current a total power of 28 kW would be produced which has to pass through the interaction region and has to be absorbed at absorbers placed at 11, 19 and 25 m downstream the experiment. Figure 2.4b shows an enlarged view of the region around the beam line. To make sure that the major part of the synchrotron radiation (SR) does not hit the beam pipe wall a large vacuum pipe is designed. Due to the large tail of SR in the horizontal plane the shape of this beam pipe needs to be elliptical (46 mm (vertical) $\times$ 119 mm (horizontal)).

The foreseen luminosity increase after the upgrade as quoted in table 2.1 is an effect of the reduced β functions at the IP and the somewhat increased beam currents. The result will lead to a luminosity of $7.5 \cdot 10^{31}\,\mathrm{cm}^{-2}\,\mathrm{sec}^{-1}$ which is a factor five higher than before the upgrade.

2.2 The ZEUS detector

The ZEUS detector is a multi-purpose detector. It has tracking detectors close to the collision point to detect the path of charged particles. Then surrounding the tracking detectors, calorimeters measure the energy of particles. Finally a muon detection system surrounds the detector. A detailed description of the ZEUS detector can be found elsewhere [19]. A brief outline of the components relevant for this thesis is given below. A three dimensional view of the ZEUS detector is shown in figure 2.5.

2.2.1 The super conducting solenoid

Charged particles follow a curved track in the magnetic field provided by a thin super conducting solenoid, cooled with liquid helium. Table 2.2 gives some parameters of the ZEUS solenoid. The transverse momentum of a charged particle in a homogeneous magnetic field is:

$$p_t = |kqBr|, \tag{2.4}$$

where q is the charge in elementary charge units, B is the magnetic field strength in Tesla. If r is the radius in m and p_t is measured in GeV, then the curvature constant k equals $0.2998\,\mathrm{GeV\,T^{-1}\,m^{-1}}$.

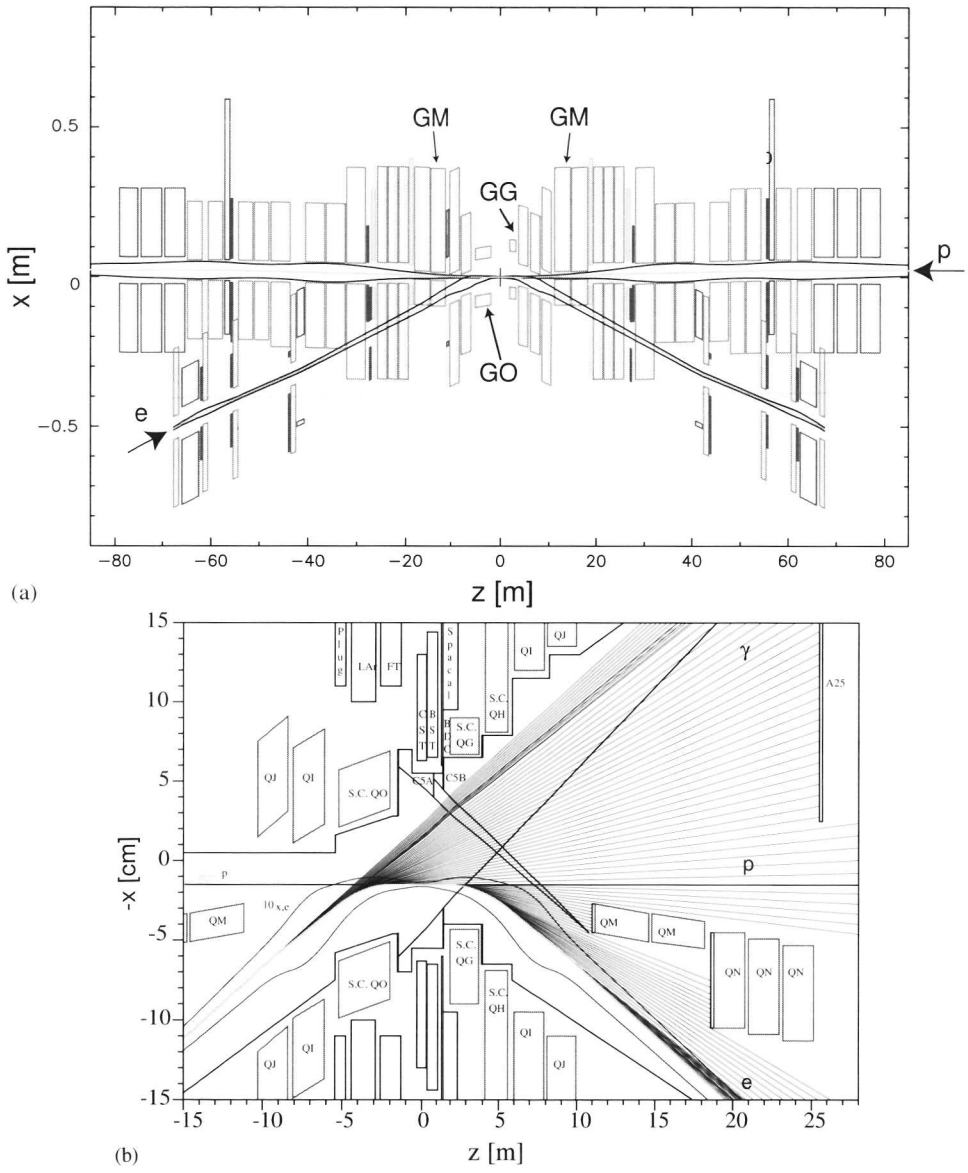

Figure 2.4: (a) Layout of the modified interaction region. (b) Synchrotron radiation produced inside the experiments has to pass the detector through the elliptical beam pipe. This figure shows the H1 interaction region, but the situation in ZEUS is similar.

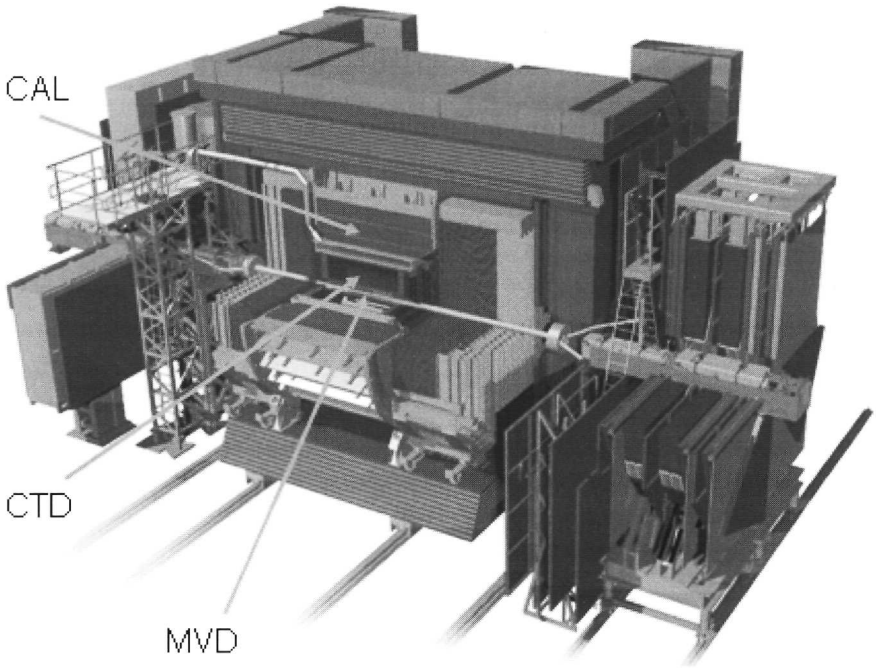

Figure 2.5: Three dimensional view of the ZEUS detector. The height of the detector is 10 m and the length along the beam line is approximately 20 m. In the drawing one quadrant of the detector is cut out to show the interior of the experiment.

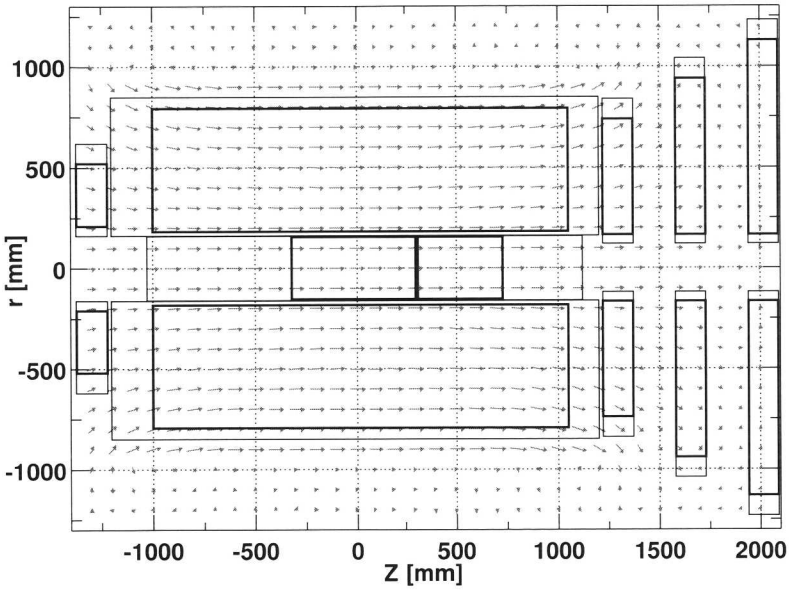

Figure 2.6: The magnetic field map of the ZEUS central detector. The length of the arrows shows the magnitude of the field. The direction of the arrow is given by the radial and axial component of the field. The different tracking chambers are named in figure 2.10.

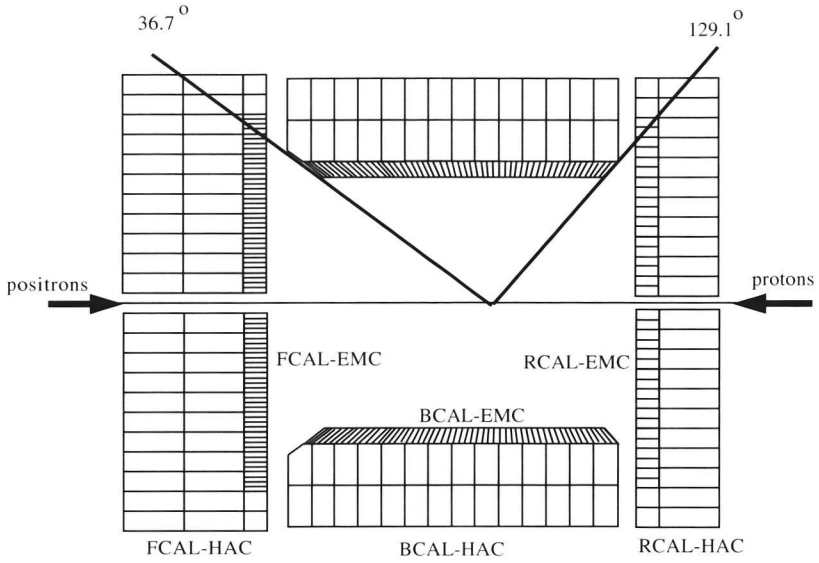

Figure 2.7: A schematic picture of the calorimeter. The different EMC and HAC sections are shown, as well as the angular coverage of the BCAL.

The field at the nominal centre of the ZEUS detector is axial with a strength of 1.43 T. In figure 2.6 the direction and the size of the field is given for a grid of space points in the tracking volume. This figure is a plot of the 1998 field map. During the upgrade the configuration of the beam magnets has changed, but it is expected that the magnetic field in the tracking volume is unchanged.

2.2.2 The calorimeter

The calorimeter is designed to stop all particles except muons and neutrinos and tries to determine the energy of the particles. The calorimeter (CAL) [20] consists of multiple layers of uranium and scintillator. The CAL has three parts: the forward[1] (FCAL), the barrel (BCAL) and the rear (RCAL) calorimeters. A cross section of the CAL in the yz plane is shown in figure 2.7.

Each part is subdivided transversely into towers and longitudinally into one electromagnetic section (EMC) and either one (in RCAL) or two (in BCAL and FCAL) hadronic sections (HAC). One EMC section has a depth of $25X_0$ (radiation lengths). This is similar to one hadronic interaction length (1λ). One HAC section has a depth of 3λ. A schematic cross section of a BCAL tower is shown in figure 2.8.

The smallest subdivision of the calorimeter is called a cell. A tower contains four electro-magnetic cells of $5 \times 20\,\mathrm{cm}^2$ in the FCAL and BCAL and two electro-magnetic

[1]Forward means in the proton direction.

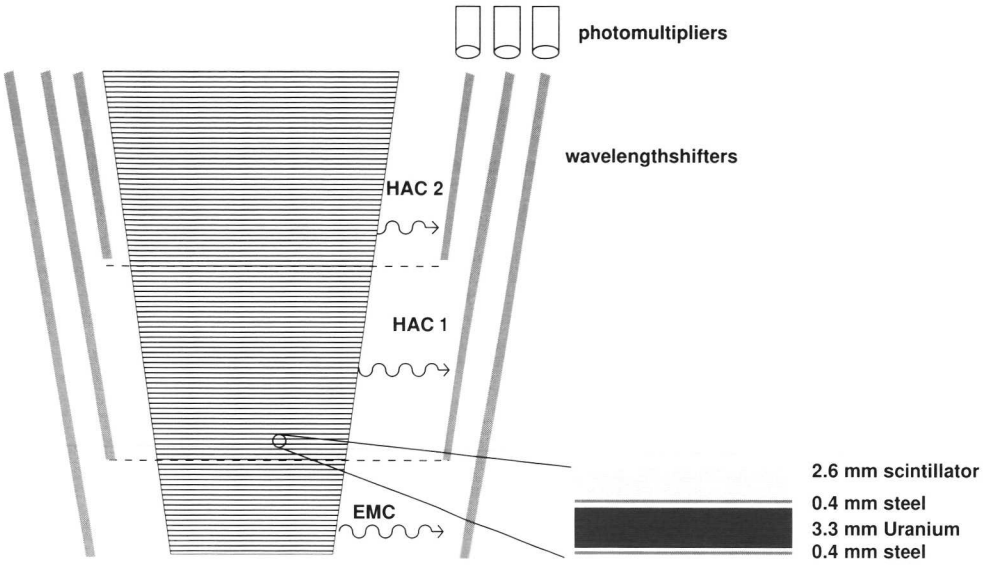

Figure 2.8: Schematic cross section of a BCAL tower.

cells of $10 \times 20\,\mathrm{cm}^2$ in the RCAL. The tower contains one hadronic cell of $20 \times 20\,\mathrm{cm}^2$ in the RCAL and two in the BCAL and FCAL.

The light produced in the scintillator material of each cell is read out via wavelength shifter planes on the left and right side of the cell. A photomultiplier tube (PMT) is connected to each wavelength shifter. Not only the signal of each cell is measured, also the arrival time of the pulse is recorded with the precision of a few ns.

The thickness of the scintillator and depleted uranium layers were chosen such that the CAL is compensating. This means that on average the response of the calorimeter (that is the measured light output) for hadrons and electrons is equal when these particles have the same energy. The CAL energy resolutions, as measured under test beam conditions, are $\sigma(E)/E = 0.18/\sqrt{E}$ for electrons and $\sigma(E)/E = 0.35/\sqrt{E}$ for hadrons (E in GeV).

Using the longitudinal and transverse shape of the "particle showers" inside the calorimeter three different classes of particles can be identified:

- electrons, positrons and photons start to shower as soon as they enter the calorimeter. They are identified in the calorimeter by the limited shower size both longitudinally and transversally,
- hadrons start to shower later and produce deeper and wider showers,
- muons lose energy in the CAL mostly through ionisation. The deposited energy is largely independent of the momentum of the muon.

Typical shower profiles for these particles are shown in figure 2.9.

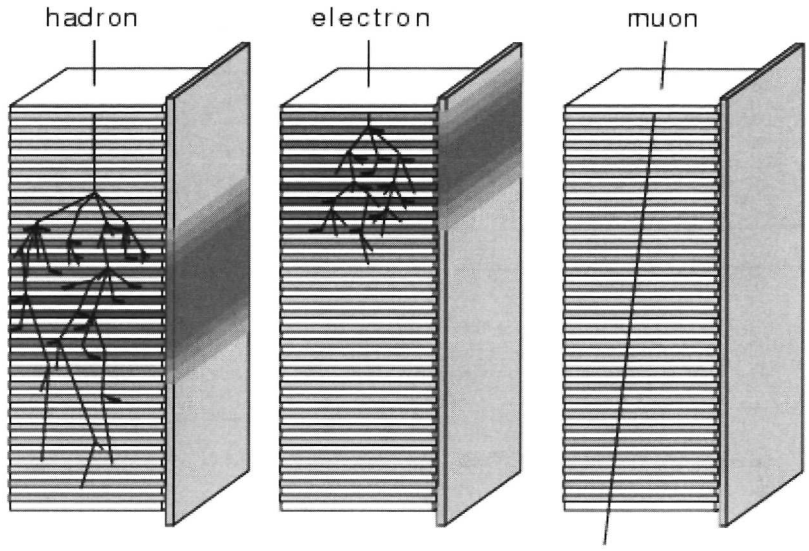

Figure 2.9: Electro-magnetic, hadronic particles and muons shower differently in the calorimeter.

Region	$\theta_{\min}$	$\theta_{\max}$
≥ 3 CTD super layers and ≥ 2 BMVD layers	19	160
≥ 3 BMVD layers	22	160
FMVD and FDET hits	7	19

Table 2.3: Different ranges in θ are covered by different tracking components.

Due to the natural radioactivity of the depleted uranium all scintillator plates of the calorimeter are uniformly irradiated, thus providing a monitoring and calibration of the scintillator light transmission and the gain of the PMTs. The measured uranium activity provides a long term calibration at the level of 1%.

2.2.3 Tracking detectors

The ZEUS detector has various tracking components. Figure 2.10 gives an overview of the tracking detectors inside the inner part of the ZEUS detector. The angular coverage in θ of the different components is found in table 2.3.

The tracking of charged particles is done with wire chambers. The wire chambers are divided in 3 regions: forward, central and rear. The ZEUS detector upgrade consists of a new silicon microvertex detector (MVD) and a new straw tube tracker (STT). The MVD has a forward (FMVD) and a barrel (BMVD) part. The MVD is the main component for this thesis and is described extensively in chapter 3.

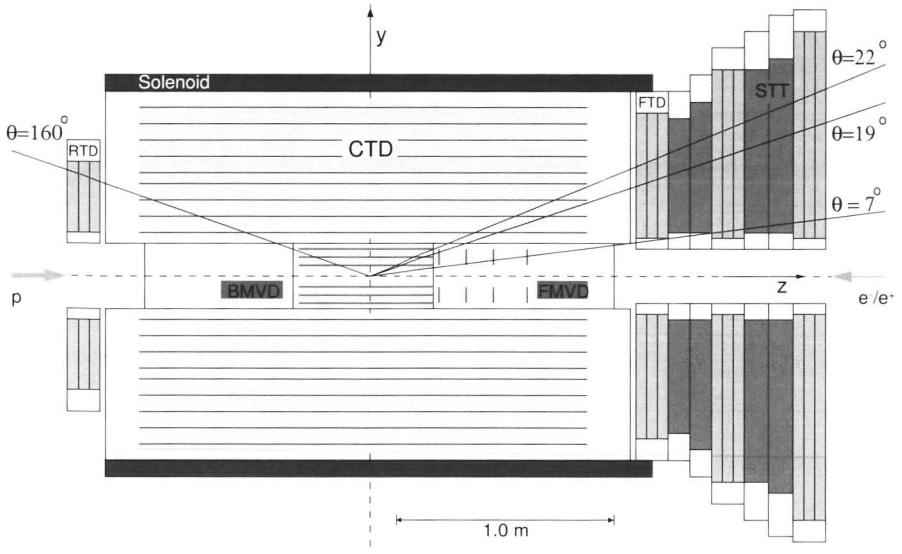

Figure 2.10: The ZEUS post-upgrade tracking system.

The central tracking detector

The central tracking detector (CTD) is a cylindrical drift chamber with 72 layers of sense wires, organised in 9 super layers. Electrons, created by the traversing charged particles that ionise the gas atoms in the CTD volume, drift towards these sense wires. Near the wire, where the field is very strong, ionisation avalanches are created. The pulse measured with the sense wires is proportional to the energy loss of the initial particle.

The time of arrival of the signal can be translated to a drift distance which gives information about the trajectory of the particle. A cosmic muon and the raw hits in the CTD are shown in the xy view in figure 2.11. The marked wires measure a signal above threshold.

Figure 2.12 shows a cross section of one octant of the CTD. Super layers 1, 3, 5, 7 and 9 are axial super layers with the wires parallel to the beam. The wires of super layers 2, 4, 6 and 8 have a stereo angle of approximately 5°. This angle can be used to give a z measurement (z by stereo), by finding the z position where the axial and stereo hits give the best fit to a track. The stereo angle is optimised to give an equal angular resolution in θ and ϕ.

Also in figure 2.12 the different track segments of a track are drawn. The ghost segments are indicated by the dotted lines and are not compatible with a track coming from the interaction point. The offset effect of the stereo layers can be clearly seen.

The sense wires of super layer 1, 3 and 5 are equipped with so called z by timing read out. The z position of the hit along the wire can be reconstructed using the difference in time of arrival of the pulse at the two wire ends. In table 2.4 some important parameters of the CTD are summarised.

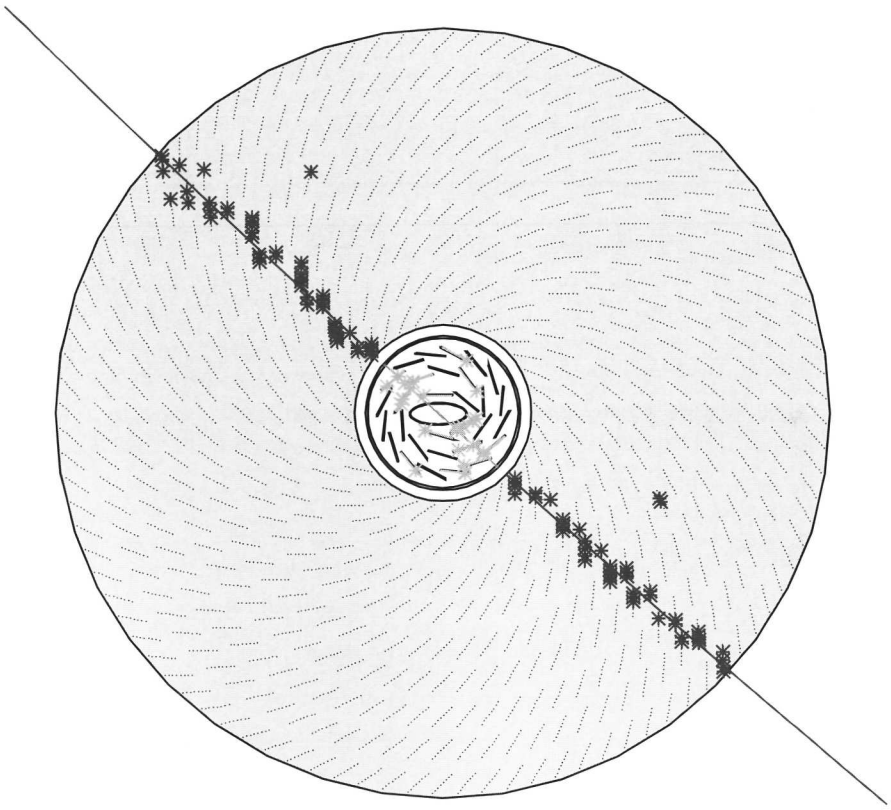

Figure 2.11: A cosmic track (in the xy view) passing through the CTD and MVD. Also shown are the raw CTD and MVD hits.

Inner radius	162 mm
Outer radius	850 mm
Length	2.41m
Position resolution	190 μm
z resolution (stereo)	1 mm
z resolution (timing)	< 3 cm
θ range super layer 3	$19^\circ < \theta < 160^\circ$

Table 2.4: Parameters for the ZEUS central tracking detector.

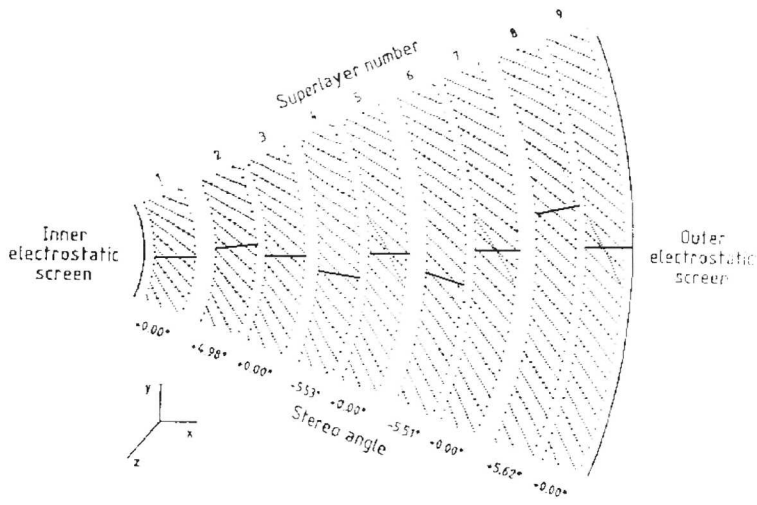

Figure 2.12: One octant of the CTD showing the super layer structure. The measured track segments in the various layers are drawn by the solid lines.

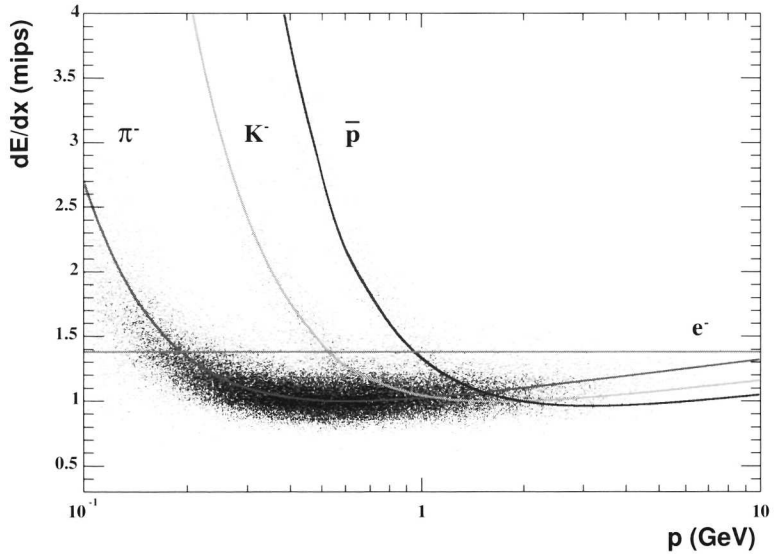

Figure 2.13: The measured dE/dx versus momentum for a sample of tracks with negative charge in the CTD. The lines show the Bethe-Bloch prediction for different particles.

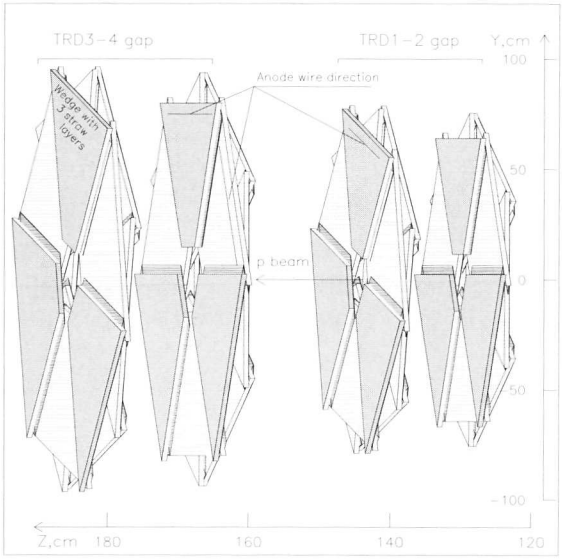

Figure 2.14: Three dimensional view of the two STT super modules.

Because the pulse height for each wire is proportional to the energy loss of a charged particle, the average energy loss per unit length (dE/dx) can be measured. The dE/dx has to be calibrated for differences in track angle, pressure and gain of the gas in the tracking chamber. The calibrated dE/dx is plotted versus the momentum of the track in figure 2.13. This is done for a sample of negatively charged particles. So in the figure different bands (π^-, K^- and $\bar{p}$) are seen which follow the Bethe-Bloch expectations for the particles. Particle identification is possible for certain momentum ranges using the dE/dx information.

Straw tube tracker (STT)

The pattern recognition capabilities of the ZEUS forward tracking have been improved by the replacement of two layers of transition radiation detector by layers of straw tubes (straw tube tracker or STT). The STT was proposed in 1998 [21] and was installed during the 2000-2001 shutdown. The layout of the STT is shown in figure 2.14. The STT covers the region of $5° < \theta < 25°$. A well measured track in this region will traverse 4 layers with in total 24 layers of straw tubes.

The straws are approximately 7.5 mm in diameter and range in length from around 20 cm to just over 1 m. They are constructed from two layers of 50 µm kapton foil coated with a 0.2 µm layer of aluminium, surrounding a 50 µm wire at the centre. The straws are arranged in wedges consisting of three layers rotated with respect to each other, to give a three dimensional reconstruction. Each of the two "super modules" consists of four layers of such wedges.

2.2.4 Trigger, data acquisition and event simulation

The HERA bunch crossing rate is very high: 10.4 MHz or every 96 ns the ZEUS detector needs to be read out. So for this reason a fast read out is necessary. Even under good data taking conditions there is a high rate of background events. More on background events can be found in section 2.3.

The challenge is to find from the ten million bunch crossings per second, the approximately five most interesting physics events. (The limitation of the 5 Hz event rate is based on the maximum data size of the offline tape storage). Approximately in 1 out of 100 bunch crossings a detectable collision occurs. This reduces the rate to 100 kHz

The approach adopted for the ZEUS data acquisition is a three level trigger system. A diagrammatic representation of this system is shown in figure 2.15.

First level trigger

The first level trigger (FLT) is a hardware based trigger which uses programmable logic to make a quick rejection of background events. The FLT reduces the input rate of 100 kHz to an output rate of 1 kHz. Because it is not possible to take a decision within the bunch crossing time (96 ns), the data are pipelined until the trigger decision is taken. The individual component decisions use a subset of the total data, and are made within 1.0 2.5 μs. The global first level trigger (GFLT) calculations then take up to 20 bunch crossings. The FLT delivers the abort/accept decision after 4.4 μs.

Typical criteria used by the FLT in taking the trigger decision are the event vertex, the transverse energy of the event, and energy sums in sections of the calorimeter. The FLT has a good efficiency for ep physics ($\sim 100\%$), but still has a very low purity ($\sim 1\%$).

Second level trigger

The SLT is a parallel processor utilising a network of transputers [22]. It reduces the FLT output rate of ~ 1 kHz to an output rate of ~ 100 Hz. Similarly to the FLT, the outputs of the component SLT decisions are passed to the global SLT (GSLT) where the event decision is made. The GSLT takes its decision after 5.2 6.8 ms. The decision is based upon limited charged particle tracking, vertex determination, calorimeter timing, $E - p_z$, jet or scattered electron tagging.

The data from an event accepted by the SLT trigger is sent directly from the component to the event builder (EVB). The EVB stores the data from the components until the third level trigger (TLT) is ready to process it, and combines the data from the different components into one consistent record: the event. One event is stored in a single record of ADAMO [23] database tables.

Third level trigger

The TLT has been designed to cope with an input rate of 100 Hz from the SLT at design luminosity. The output rate is reduced to about 5 Hz.

The TLT algorithms run on a farm of processors which processes the events in parallel. For speed reasons the TLT uses a simplified version of the offline reconstruction software

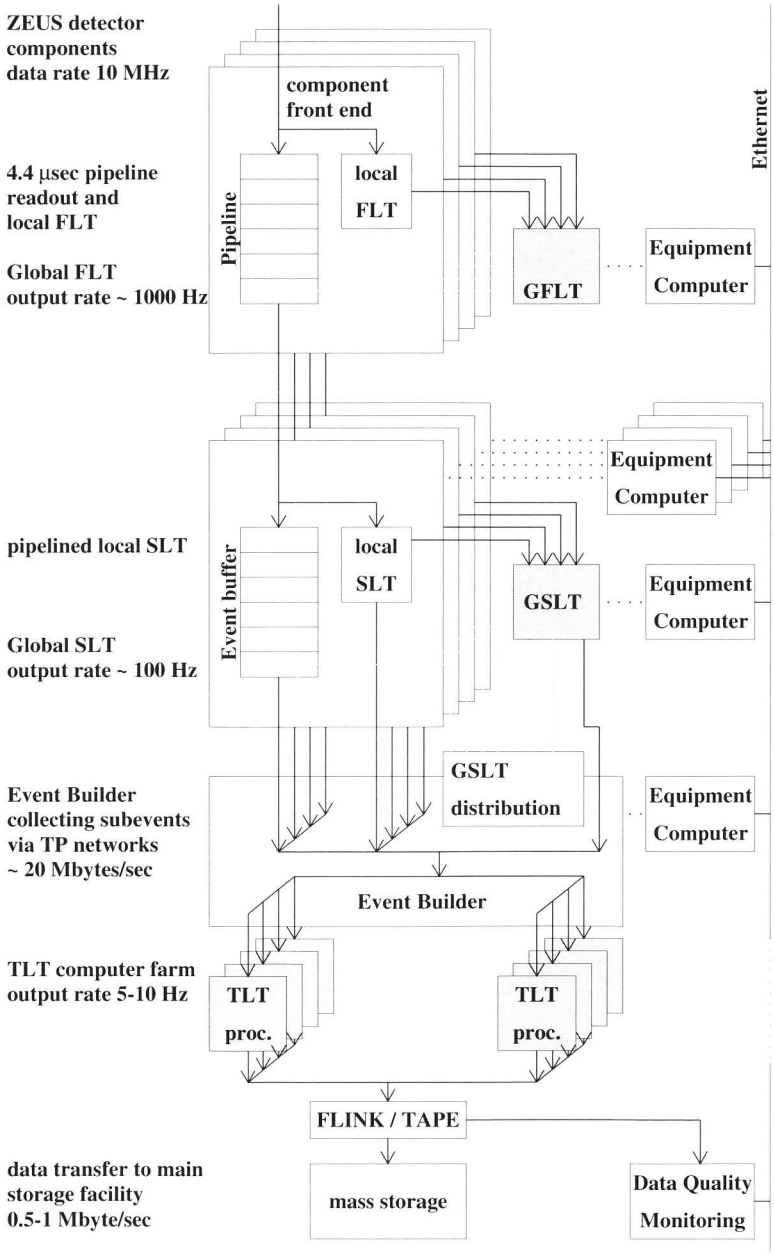

Figure 2.15: Flow diagram of the ZEUS three level trigger system used for the data acquisition.

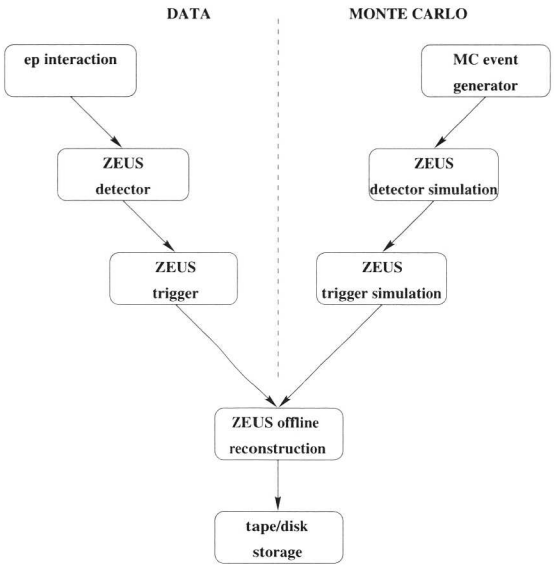

Figure 2.16: Schematic representation of the ZEUS data acquisition chain and the corresponding Monte Carlo software chain.

to calculate the kinematics of the event. Detailed tracking is performed as well as a number of jet finding routines. Neutral current DIS events are tagged using electron finders on the calorimeter deposits. Events that pass the trigger criteria get an additional tag which specifies which category the event belongs to. (For example a high Q^2 neutral current event.) These tags are known as trigger bits/slots.

Events which have triggered a TLT bit are written to tape via a tape robot, over a dedicated connection to the DESY computing centre (FLINK). During data taking the shift crew in the ZEUS control room monitors all the various trigger rates and fired trigger bits to ensure the quality of the data.

Reconstruction

The raw data are processed offline typically a few days after the data were taken. Calibration constants which are not available online are implemented here. The more CPU intensive parts of the reconstruction code are implemented here rather than in the TLT. A filter also runs over the events which is similar to a 4^{th} level trigger. This again uses physics motivated criteria to select samples of similar events, which are then allocated a code, known as a DST bit. Furthermore the most important quantities for physics studies are stored in so called MDSTs (mini data summary tapes).

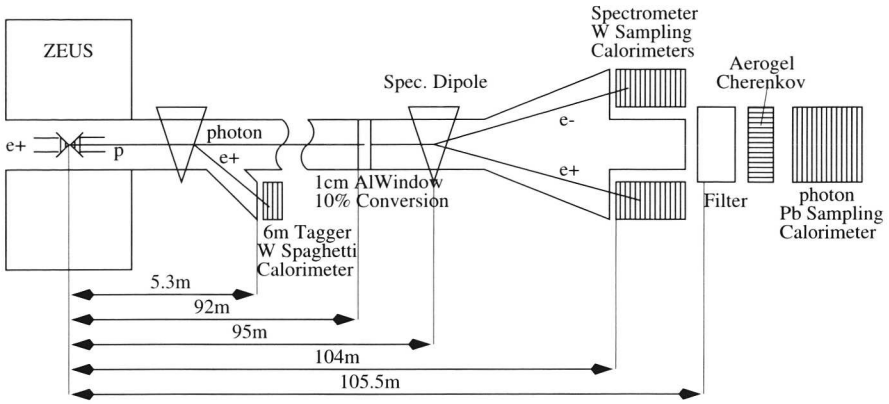

Figure 2.17: Schematic diagram of the post upgrade ZEUS luminosity measurement.

Monte Carlo simulation

Figure 2.16 gives a flow diagram of the ZEUS data taking. Each block in the diagram has an analogous block in the Monte Carlo simulation. The *ep* interactions can be simulated using event generator programs. The generated final state particles are then passed to the ZEUS detector simulation. This program is based on GEANT [24].

The next step in the simulation chain is the trigger simulation. Finally the Monte Carlo events are reconstructed with the same programs as were used to reconstruct the data.

2.2.5 Measuring the luminosity

The delivered luminosity at ZEUS is determined by measuring the bremsstrahlung process $ep \rightarrow ep\gamma$. The cross section of this (Bethe-Heitler) process has been calculated to high accuracy [25]. This process is measured using a lead-scintillator calorimeter that is placed at z equals -107 m from the interaction point. It accepts photons at angles ≤ 0.5 mrad with respect to the electron beam direction. The luminosity corresponding to the events stored on tape is measured with an uncertainty of $\sim 3\%$ [26].

The measurement of the luminosity at HERA-II must cope with the greatly increased synchrotron radiation background and the higher probability for multiple bremsstrahlung photons in a single beam crossing. To compensate for the latter, two devices have been constructed with very different systematic uncertainties.

First the old photon calorimeter has been upgraded to obtain better shielding. Secondly a new setup is added to measure photon conversions ($\gamma \rightarrow e^+e^-$). This setup consists of two separate calorimeters which measure coincidences of the e^-e^+ pairs which come from conversions in the photon pipe exit window. A schematic diagram of the new luminosity measuring system is shown in figure 2.17.

Both devices use the information from a small calorimeter placed around 6 m from the interaction point which detects the radiating electron. By using the two measuring devices a reduction of the systematic errors is expected to produce a precision of about 1%.

2.3 Running experience in 2002 and 2003

Shortly after the HERA restart, in the fall of 2001, it was observed that already at low beam currents the backgrounds in the ZEUS detector were very high. One problem was that there was not enough shielding to protect the ZEUS detector from direct synchrotron radiation generated by the positron beam. The radiation came from more than 100 m downstream the interaction point. During a shutdown in the winter of 2002 the additional shielding was installed.

During 2002 it was noticed that the backgrounds in the ZEUS (and H1) detector were still something like 10 times larger than had been anticipated. A large effort was done by the experimental groups and the HERA machine physicists to understand the source of the backgrounds [27]. There are at least three sources that contribute to the problem:

- off-momentum positrons in time with the positron beam,
- indirect synchrotron radiation back-scattered mainly from an absorber about 11 m on the upstream proton side of the ZEUS interaction point,
- a very large increase in proton beam-gas background, due to the poor dynamic vacuum in the region immediately surrounding the interaction region.

The "commissioning" period for HERA and the experiments, from October 2002 to March 2003, aimed at diagnosing the background problems and delivering luminosity to the experiments for commissioning of the detectors.

Following this, there was a 3 months shutdown in the spring for modifications close to the interaction region that reduce the level of backgrounds in the detector. Since October 2003 there has been a period of stable running, which has provided physics quality luminosity for the detectors.

Figure 2.18 shows the integrated luminosity delivered to ZEUS by HERA and the integrated luminosity recorded by the experiment. Also shown is the integrated luminosity with the MVD turned on. As can be seen, the total amount of recorded data is about 15 pb^{-1}. For 85% of the data the MVD was turned on and delivered good data.

2.3.1 Backgrounds in the CTD

The CTD has been an essential tool in understanding the backgrounds. It was expected that the backgrounds would inevitably be higher after the upgrade, particularly a higher level of synchrotron radiation caused by the more intensely focused beams and new beam optics needed for HERA-II. New interaction region collimators were designed to avoid any direct synchrotron radiation reaching the sensitive components of the detector. In

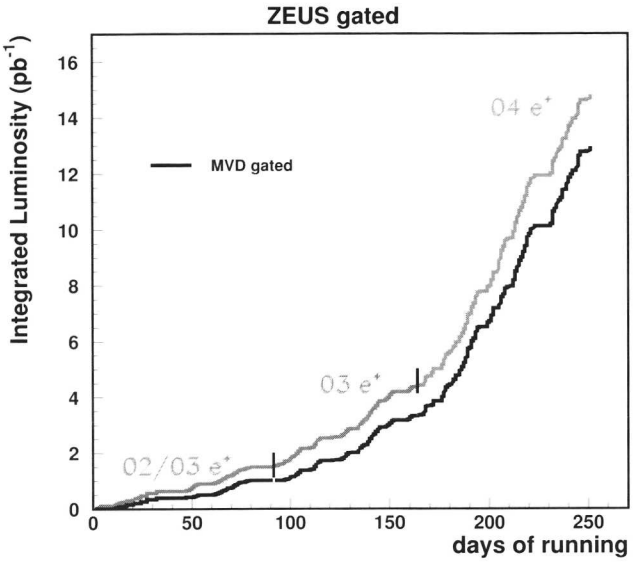

Figure 2.18: Luminosity gated by the ZEUS experiment until April 2004. Also shown is the integrated luminosity recorded with the microvertex detector delivering good data.

this respect the new collimators have been successful, but unfortunately a rather large amount of radiation back-scattered from the main absorber, positioned 11 m downstream the interaction point. The back-scattered radiation was then hitting the collimator nearest to the MVD and was scattered into the CTD.

It was also expected that the vacuum in and around the interaction point would be worse because the new final-focus superconducting magnets, positioned just inside the ZEUS calorimeter on both sides, do not allow space for as many high-vacuum pumps as before. However while the static vacuum seemed not to be a problem, the dynamic vacuum (positron-beam induced degradation of the vacuum) was much worse than expected. The combination of a narrower beam pipe, cold surfaces, more collimators, fewer pumps and new optics complicated the diagnosis of the problems.

To absorb the reflected synchrotron radiation better, the collimator nearest to the MVD was redesigned and re-installed in the 2003 shutdown. The reduction in the reflected synchrotron radiation is demonstrated in figure 2.19b, which shows the distributions of CTD hits before and after the summer 2003 shutdown. The z distribution of the hits is now flat, with the characteristic peak from the reflections having disappeared. The drift time distribution is now dominated by contributions in time with the beam. The clear reflections seen in 2002 are no longer present. It can be concluded that the reflected synchrotron contribution to the background is now small.

The operation of the CTD suffered from the high currents caused by the beam related backgrounds. Too high currents form a problem for the lifetime of this wire chamber. To prepare for the worse running conditions in the future, the high voltage of the sense

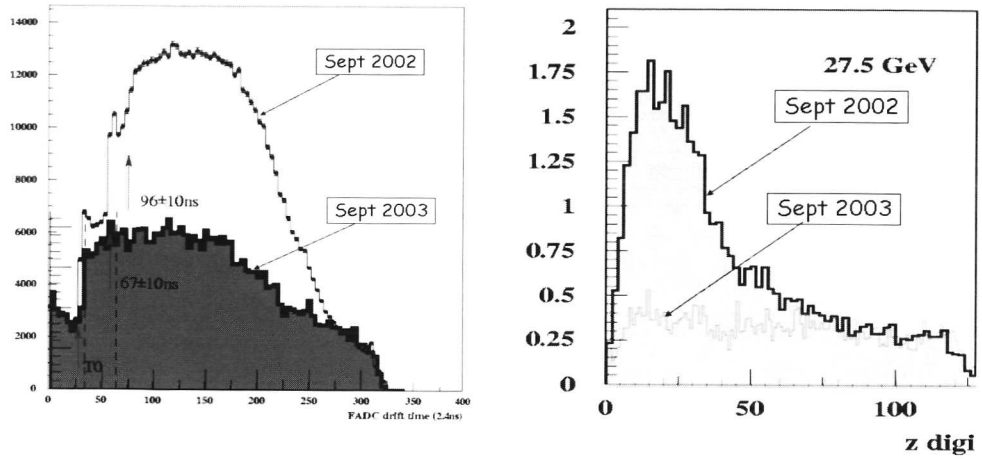

(a) (b)

Figure 2.19: Distribution of the CTD hits before and after the summer 2003 shutdown. In (a) is shown the drift time distribution with respect to the HERA bunch crossing, marked T0 on the plot. The major contributions from synchrotron radiation reflections are indicated. In (b) is shown the z distribution of the CTD hits.

wires in the CTD was lowered to 95% of the nominal voltage. To compensate for the lost efficiency, the noise threshold was reduced.

The measures taken to reduce the reflected synchrotron radiation were expected also to improve the dynamic vacuum, because the heating of the beam pipe would be reduced.

An additional effect of the proton induced background was the showering of particles inside the material of the collimator close to the interaction point ($-80\,\text{cm}$). By reshaping this collimator and making it thinner an additional reduction in background was expected.

Changes in the commissioning procedure were introduced in an attempt to reduce the amount of gas "stored" in the beam pipe walls: The beam pipe near the interaction region was heated prior to the luminosity running period, to free the gas present in the walls. In addition during August 2003 there was a period, when the machine ran with high positron currents for several weeks, to try and "bake-out" remnant gas from the beam pipe walls. This combined with a procedure for regular warm-ups of the cold final focusing magnets in the interaction regions to room temperature to remove frozen gas on the inner surface of the magnets was shown to significantly improve the observed dynamic vacuum.

The overall effect of these changes on the running conditions for the experiment are demonstrated in figure 2.20, which shows the measured CTD sense wire currents, normalised to particular proton beam currents. The improvement with time, at monthly intervals during the luminosity run, due to the integrated positron beam current is clearly seen.

Extrapolating from the present running conditions, it should be possible to run the CTD within the safe operating limit on the sense wire currents even at the maximum

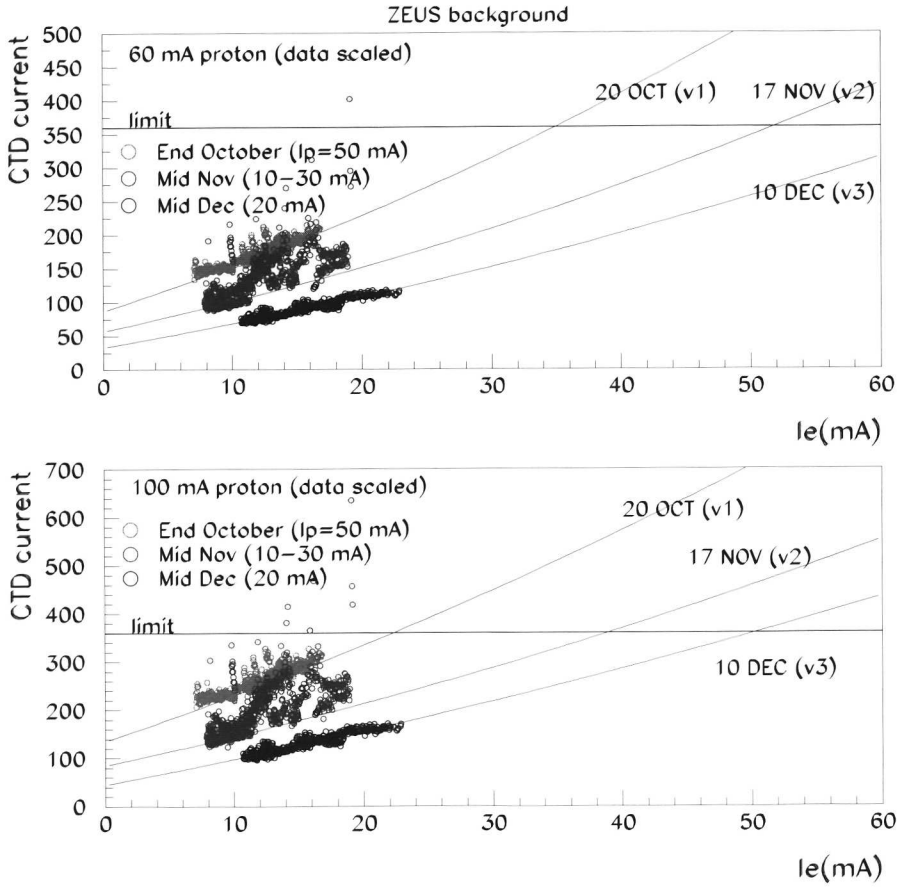

Figure 2.20: Background conditions during the last three months of 2003, in terms of the drawn CTD sense wire currents (in ADC counts). The safety limit is set to 360. The CTD currents drawn are rescaled to the proton currents indicated.

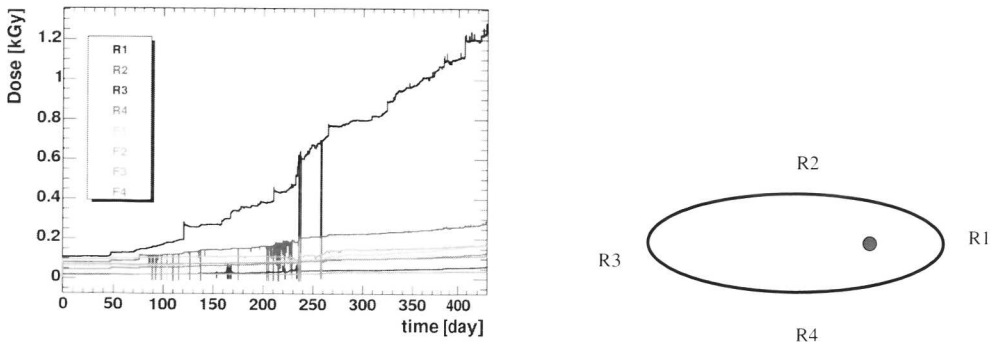

Figure 2.21: Integrated radiation dose measured with the ZEUS RADMON system during 2002/2003 running.

predicted beam currents.

2.3.2 Backgrounds in the MVD

The first *ep* collisions in the MVD were recorded in the fall of 2002. That first data taking period lasted until March 2003 and was characterised by the large backgrounds, a small integrated luminosity and a significant radiation dose. Nevertheless, that period was used for the commissioning of the MVD as described in this thesis.

The MVD sensors and in particular the Helix front end chip are not implemented in radiation hard technology. A moderate level of radiation tolerance is achieved by the flexibility of the Helix architecture which permits the tuning of a large number of the chip's parameters. On the basis of results from irradiation tests, a radiation budget of 3 kGy accumulated dose in the electronics has been established for the entire lifetime of the detector [28].

The absorbed dose during operation of the detector is carefully monitored with a system of radiation sensitive devices:

- The instantaneous dose rate is measured with a system of 16 PIN diodes mounted both in front and in the rear of the detector at four locations close to the beam pipe. This system is connected to the general ZEUS alarm and interlock system. In addition to giving warnings to the ZEUS and HERA shift crews both in the case of very large instantaneous rates as well as high rates over extended periods, it can also abort the lepton beam in HERA.

- Integrated doses are measured with 8 radiation field-effect transistors (RADFET) placed close to the PIN diodes.

- The doses measured in the RADFETs are cross calibrated with six removable thermoluminescent dosimeters (TLD).

Figure 2.21 shows the integrated dose rates measured in the 8 RADFETs during the first running period after the HERA upgrade. The RADFET R1 placed behind the detector on the inside of the HERA ring registered an integrated dose rate in excess of 1.2 kGy or more than one third of the radiation budget of the MVD for its entire lifetime. The continuous rise of the line R1 represents normal detector operation. The jumps are caused by beam accidents.

The strong asymmetry of the radiation dose seen in the RADFETs indicate that the dose originates predominantly from so-called off momentum positrons in the HERA machine which hit a synchrotron radiation collimator close to the rear RADFETs. The estimation of the effective dose received by the detector electronics is complicated. Simulations of this background component suggest that the dose measured in the RADFET R1 should be scaled down by approximately a factor 30 to obtain the dose seen in the MVD electronics.

The effect of the backgrounds on the data taking are explained in figure 2.22. For this study the data of the first 3 months of 2003 are used. Using some simple criteria (timing, energy, vertex, etc.) events are divided in different classes: halo muon, proton-gas, off-momentum positron, deep inelastic scattering and photoproduction. In the figure is seen that a small fraction of the data are real physics events. The physics events are measured with a low number of hits in the MVD (less than 200). It is seen that the large tail for high occupancy in the MVD is caused by the background events.

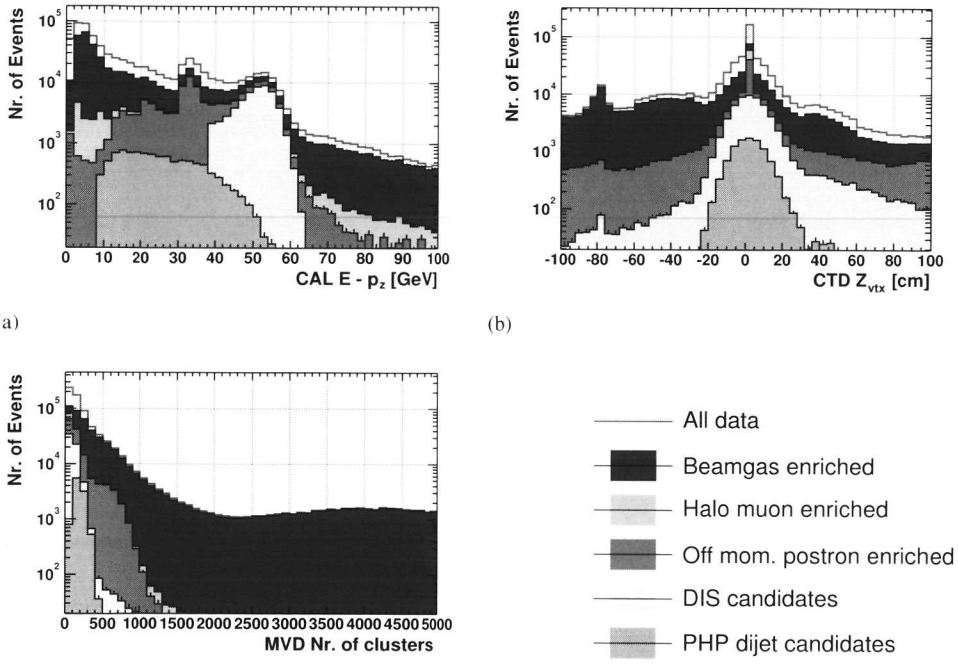

Figure 2.22: Data from good runs of the first 3 months of 2003, including the MVD. The solid line represents all the data. The events are divided in halo muons, proton-gas, positron-gas, deep inelastic scattering and photoproduction candidates using a number of criteria (timing, energy, vertex, etc.). In (a) the $E-p_z$ measured with the CAL is plotted. In (b) the z vertex measured with the CTD and in (c) the number of hits in the MVD are shown. It is seen that mainly the background events are the reason for the large tail in distribution of the number of MVD hits.

Chapter 3

The ZEUS microvertex detector

During the 2000-2001 shutdown the ZEUS experiment has installed a new component called the microvertex detector (MVD). In this chapter details about the detection principle, layout and readout can be read.

To profit from a detector with a high resolution the mechanical precision and the distribution of the dead material are very important.

3.1 Design

Before the upgrade the central tracking detector (CTD) was the most inner detector component. The CTD inner shell starts at a radius of 16.2 cm from the beam line. This results in large uncertainty on the track positions close to the interaction point. To recognise a secondary vertex using the CTD only, it has to be separated from the primary vertex by at least 0.5-1 cm. Since the typical decay length of charmed particles is of the order of 100-300 μm, heavy quark tagging using secondary vertices is very inefficient with the CTD.

Therefore it was decided by the ZEUS collaboration to build a vertex detector, to improve the tracking in general. The resulting improvement provides the possibility to select a very pure heavy quark sample by selecting events with displaced vertices. The microvertex detector (MVD) was proposed in January 1997 [29]. The design and construction took four years. In March 2001 the detector was installed in ZEUS. The design specifications for the MVD were:

1. polar angular coverage of 10-170°
2. three space points along each track
3. better than 20 μm intrinsic hit resolution
4. impact parameter resolution, for tracks with momentum larger than 2 GeV, of 100 μm for a polar angle of 90°
5. noise occupancy $< 10^{-3}$

6. hit efficiency > 97%

7. alignment accuracy better than 20 μm

8. two track separation of 200 μm

In the remainder of this chapter the choice for a silicon detector, the principles of charged particle detection in semiconductors, signal processing, the layout of the MVD, the precision of the construction and the material distribution are discussed

3.1.1 Detection principle

There are many advantages in using semiconductor (or silicon) detectors. When a charged particle traverses a silicon sensor many more charge carriers are produced per unit traversed length than in gaseous detectors, allowing the use of thin detectors ($\sim 300\,\mu m$) which still yield significant signals. The charge carriers move very quickly through the silicon lattice, thus the charge collection can be fast ($\sim 10\,ns$). For a position sensitive silicon sensor one or both sides of the diode are segmented into strips. The strip pitch can be very small, of the order of $\sim 10\,\mu m$. Such a small strip pitch makes very precise position reconstruction possible.

The precision is eventually limited by multiple scattering (the particle trajectories are disturbed in material of the silicon, support structure and readout electronics, see also section 4.1.3). Furthermore to achieve the high precision a very accurate and stable design of the detector is required.

Electron-hole pair generation

When a charged particle traverses matter, the particle loses energy. The amount per unit length is given by the Bethe-Bloch equation:

$$-\frac{dE}{dx} = 2\pi N_A m_e r_e^2 c^2 \rho \frac{z^2}{\beta^2}\frac{Z}{A}\left[\ln\left(\frac{2m_e\gamma^2 c^2 W_{max}}{I^2}\right) - 2\beta^2 - \delta - 2\frac{C}{Z}\right], \qquad (3.1)$$

where N_A is Avogadro's number, m_e the electron mass, r_e the classic electron radius, ρ is the density of the traversed material, z the charge of the incident particle, $\beta = v/c$ the velocity of the particle in units of the speed of light, Z and A the atomic number and atomic mass (in g/mol) of the medium, $\gamma = (1-\beta^2)^{-1/2}$, I the effective ionisation potential, W_{max} the maximum energy transfer in a single collision, δ a density correction and C a shell correction. The maximum energy transfer for a particle with mass M is given by:

$$W_{max} = \frac{2m_e c^2 \beta^2\gamma^2}{1 + 2\gamma m_e/M + m_e^2/M^2}. \qquad (3.2)$$

The energy loss of the particle will lead to the generation of electron-hole pairs in the silicon crystal. The average energy necessary to generate an electron-hole pair in silicon is approximately 3.6 eV.

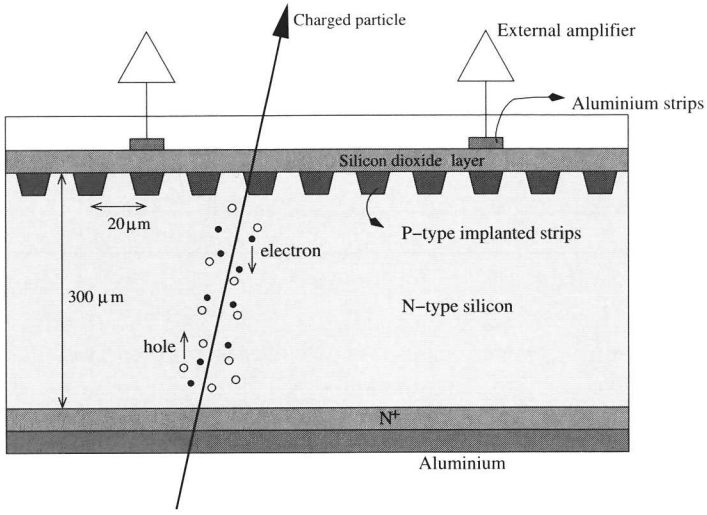

Figure 3.1: Schematic cross section of the ZEUS silicon strip sensor.

In silicon the minimal energy loss $(dE/dx|_{\min})/\rho$ is $1.664\,\mathrm{MeVg^{-1}\,cm^2}$. The density of silicon is $2.33\,\mathrm{g\,cm^{-3}}$. Then for a minimum ionising particle (MIP) traversing 300 μm thick silicon the average number of created electron hole pairs is 39000. The energy loss follows a Landau distribution so the most probably energy loss is approximately 30% lower. This means that typically 27000 electron-hole pairs are generated in the 300 μm of traversed silicon in a "tube" around the track with a radius of about 10 μm. How the generated charge is measured and how the position of the hit is determined are described in the sections 3.1.3 and 3.1.4.

Sensor layout

In the MVD silicon sensors only the p-side is segmented into strips. Since the strips give only one coordinate, two sensor layers are combined. A cross-sectional view of the MVD silicon sensor is shown in figure 3.1.

The sensors are 300 μm thick and the bulk of the sensor is n-doped silicon. At one side parallel p-doped silicon strips are implanted at 20 μm distance from each other. The design and the tests of the silicon sensors are described extensively elsewhere [30]. The important parameters are summarised in table 3.1.

In figure 3.2 a photograph of the top corner of a silicon sensor used for the BMVD is shown. Clearly seen are the readout strips with in between the 5 intermediate p strips. The distance between two readout strips is 120 μm. The bias voltage is applied to the n^+ backplane via the n^+ contact strip. Three guard rings surround the sensor to provide a homogeneous field in the area where the strips are. Also an alignment marker is seen in

	Barrel	Wheels
Nr. of strips	512	480
Read out pitch	120 μm	120 μm
Implant pitch	20 μm	20 μm
Nr. of sensors	600	112
Sensor area	41.2 cm^2	34.9(25.7) cm^2
Strip length	62.2 mm	range: 5.6-73.3 mm (5.6-47.7 mm)
Nr. of strips	307k	54k

Table 3.1: Parameters of the silicon sensors. The values for the wheels only apply to the large (small) sensors. The strip lengths for the forward sensors are not constant, see figure 3.7a.

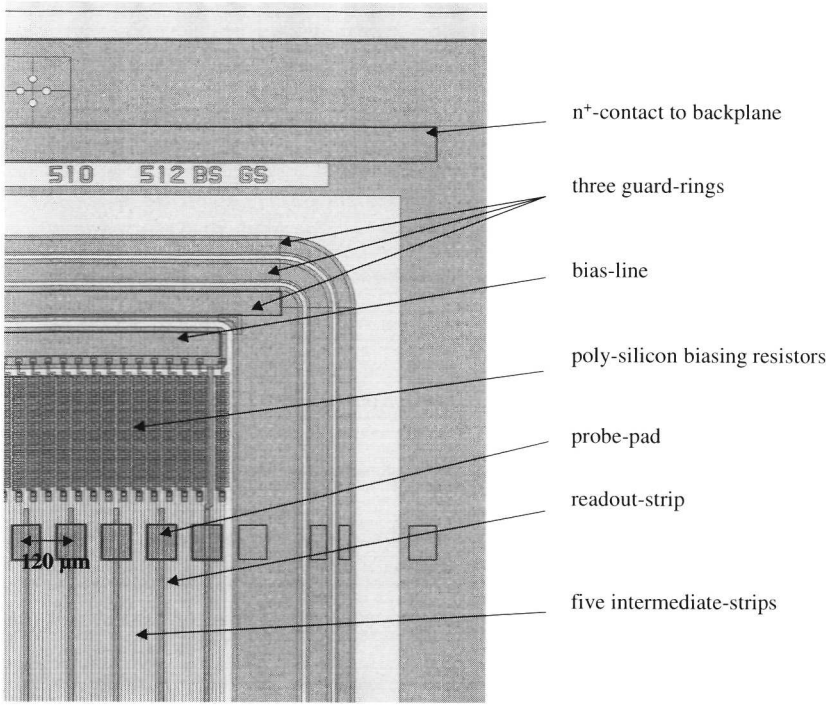

Figure 3.2: Photograph of the corner of a silicon sensor ($1.25 \times 1.85\,mm^2$) used for the barrel MVD. In the upper left corner one of the alignment markers is seen.

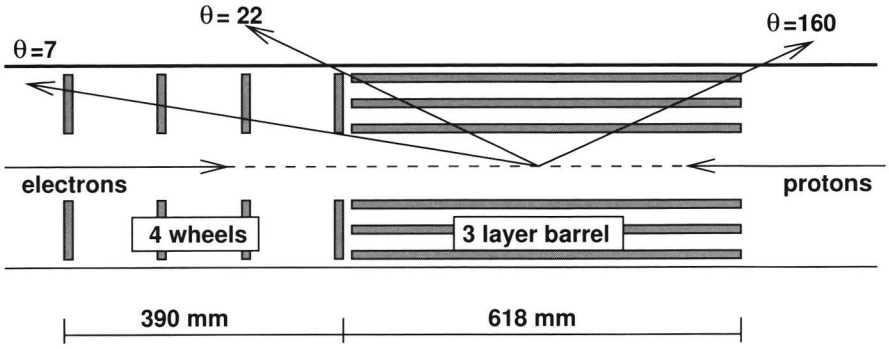

Figure 3.3: Side view of the geometry of the ZEUS microvertex detector.

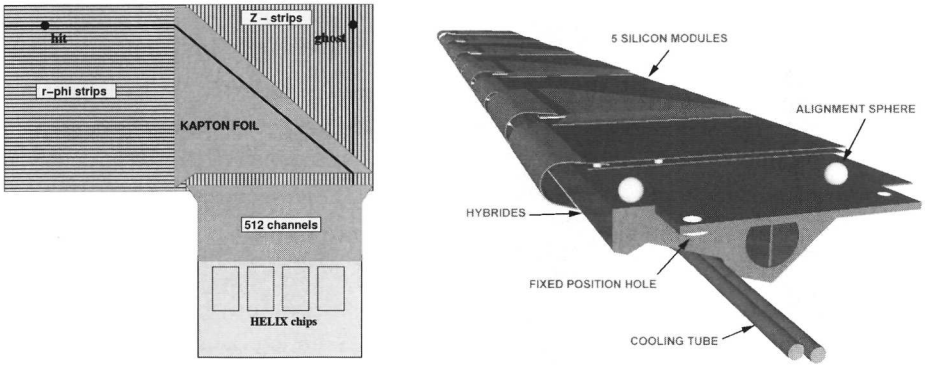

(a) (b)

Figure 3.4: An MVD outer half module (a). The dimensions of a single sensor are $6.2 \times 6.2\,\mathrm{cm}^2$. An MVD barrel ladder structure (b) supports 5 modules, front-end electronics, cooling, power supply and read out cables.

the top left corner. The alignment markers on the sensor are used for precise assembly of the detector. Because the edge of the sensors are unused, the effective area of the sensor is approximately 92.7%.

3.1.2 Layout

The microvertex detector (MVD) is equipped with a total of 712 silicon strip sensors distributed over the barrel MVD (BMVD) and the forward MVD (FMVD). The barrel part is organised in 3 cylinders and the forward part in 4 wheels. The general layout is sketched in figure 3.3.

In the barrel two sensors are glued together to form a *half-module* as depicted in figure 3.4a. It can be seen that two sensors are read out with one hybrid. The hybrid

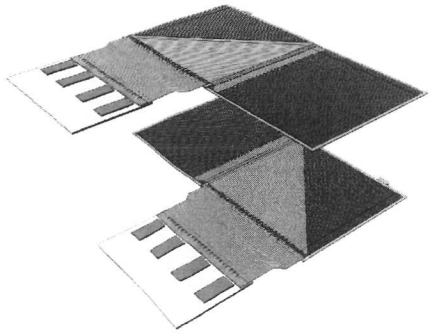

Figure 3.5: The assembly of a full MVD module

supports the readout chips (see section 3.1.3). The strips of the two sensors run perpendicular. When placed in the barrel MVD one sensor gives a z coordinate while the other gives $r\phi$ information. Since the strips are electrically connected with a bond wire, it can not be determined in which of the two sensors a particle has passed. This has to be done in conjunction with the track reconstruction. By combining the information of other hits and the measurements in the CTD the real hit and the "ghost" hit can be disentangled.

A full *module* is formed by gluing a "mirror imaged" half module on top of another half module (see figure 3.5). Information from the "inner" and "outer" half module delivers a 3-dimensional space point.

In the MVD barrel, five modules are glued on a *ladder*, see figure 3.4b. The ladder is made of carbon fiber composite and provides a stiff frame to support not only the modules but also the electronics, the (water) cooling tubes and the cables for read out, power supply and monitoring.

Figure 3.6 shows how 30 ladders are located around the beam pipe. The ladders are divided in 3 *cylinders* containing 4, 10 and 16 ladders respectively. The inner cylinder is not hermetic in ϕ due to the extra space needed for the elliptical beam pipe.

The forward *wheels* support the forward sensors which are wedge shaped as is shown in figure 3.7. A forward sensor is similar to a barrel sensor. It has the same intermediate and readout strip pitch, see table 3.1. One difference is that one sensor has 480 read out strips. Furthermore one hybrid is connected to only one sensor. A wheel has inner sensors and outer sensors. They are mounted back to back. An inner and outer wheel sensor form a sector. The crossing angle between the strips in the inner and outer sensor is $180°/14$.

A total of 112 sensors are supported on 4 wheels, see figure 3.8. Some sensors are shorter to provide sufficient space for the beam pipe.

From measurements after construction and first studies on tracks the main uncertainties in the detector alignment are the z positions of the ladders and wheels [31] and the z position of the MVD with respect to the CTD (see section 5.3). The design geometry is used to describe the positions of the silicon sensor and the positions of the dead material unless otherwise specified. More on the precision of the construction can be read in

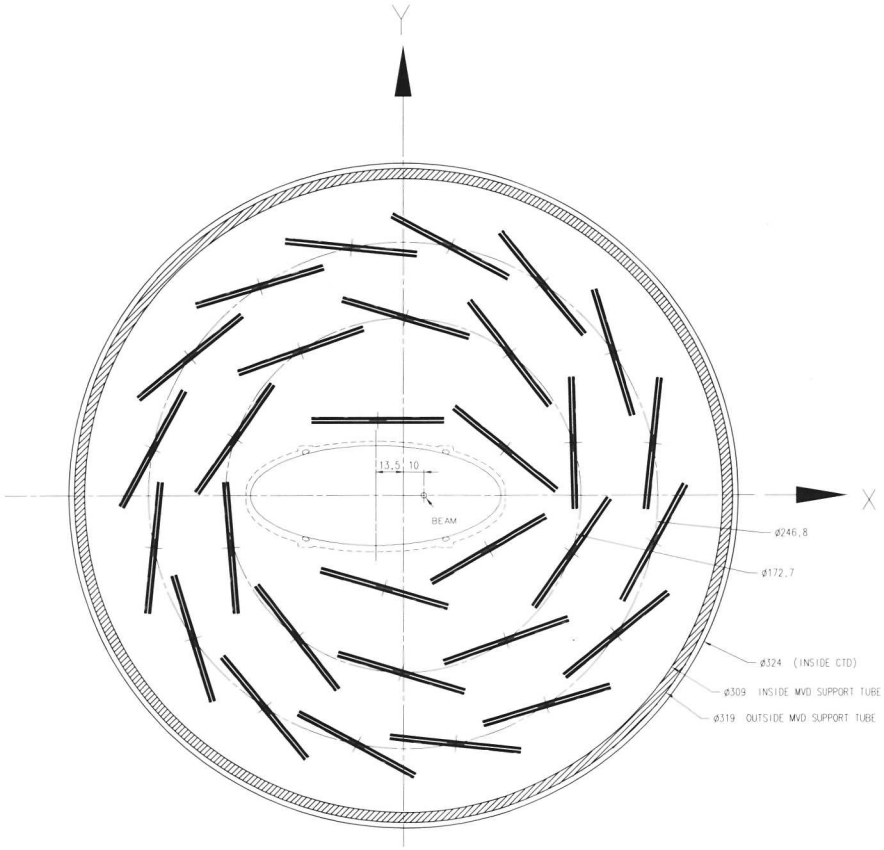

Figure 3.6: Cross section of the MVD barrel, shown are the planes of silicon, which are supported by the carbon fiber ladders.

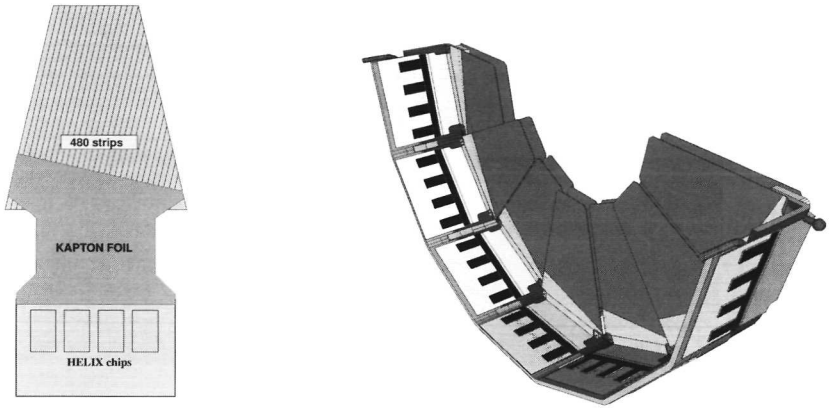

(a) (b)

Figure 3.7: Wedge shaped forward sensor (a) and the layout of a half forward wheel (b) which includes 14 forward sensors.

section 3.2.1.

3.1.3 Readout

To achieve better position resolution the signals from the silicon are read out analogue. The selected chip to perform the front-end readout is the Helix 3.0. The chips are mounted on ceramic structures called the hybrids.

One Helix chip amplifies the charge measured at each of the 128 input channels. Then the signal is shaped in a pulse with a peak height proportional to the measured charge. The width of the pulse is of the order of 50 ns, so the measurement can be done within one HERA bunch crossing. Then at a given clock rate, the peak value of each channel is sampled. To do this with the best signal to noise ratio the sampling has to coincide with the time the pulse is at its peak value. The peak value is stored in a 128 deep pipe line. The signal shapes are depicted schematically in figure 3.9.

When a first level trigger signal arrives, the appropriate channel of the pipeline is selected and the 128 signals are multiplexed. (In this phase the signals are still analogue.) In total 8 chips are read out in sequence. This corresponds to one MVD module in the barrel or one MVD sector in the wheels. The signal is transfered by an analogue link to one ADC unit (10 m away) consisting of a 10 bit 10 MHz ADC, data processor (DSP) and buffer [32].

In general the signal of a charged particle is seen as a cluster of charge on more than one strip. More details about the measured clusters can be found in section 3.1.4. After the ADC module has processed the data, which consists among others of accepting strips within predefined cluster thresholds, three data streams are available for analysing MVD data.

RAW Every channel of the MVD data is saved. This is useful for calibration

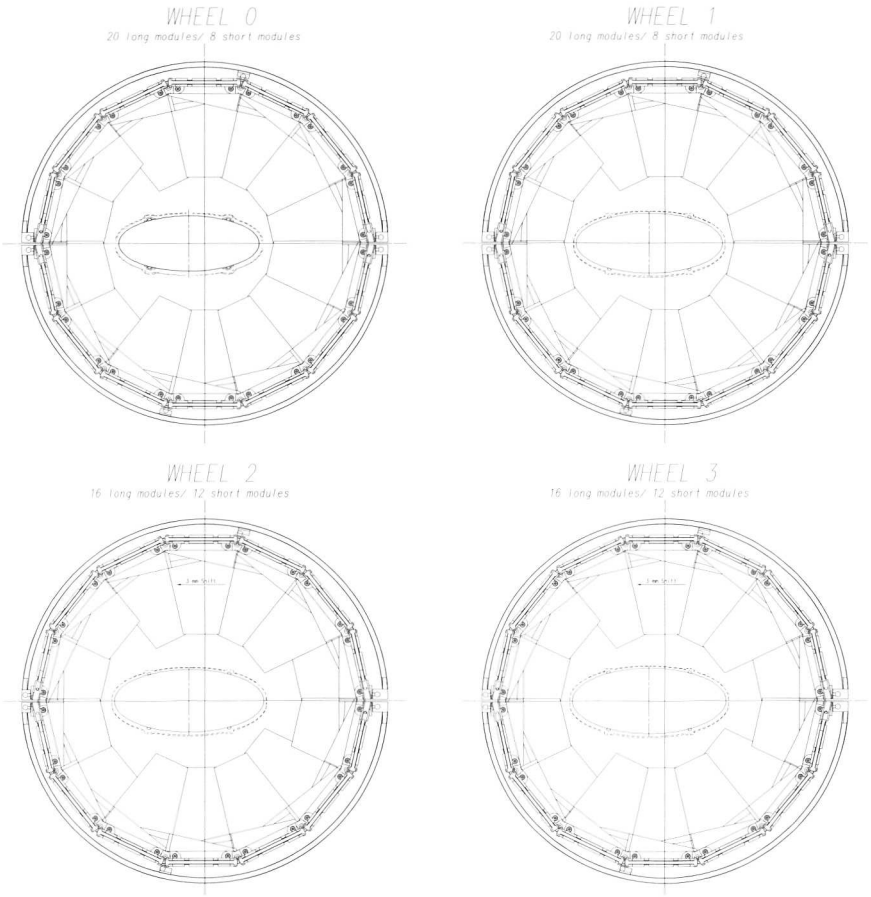

Figure 3.8: Orientation of the wheel sensors for the four forward wheels. Some sectors are accommodated with shorter sensors to fit around the beam pipe.

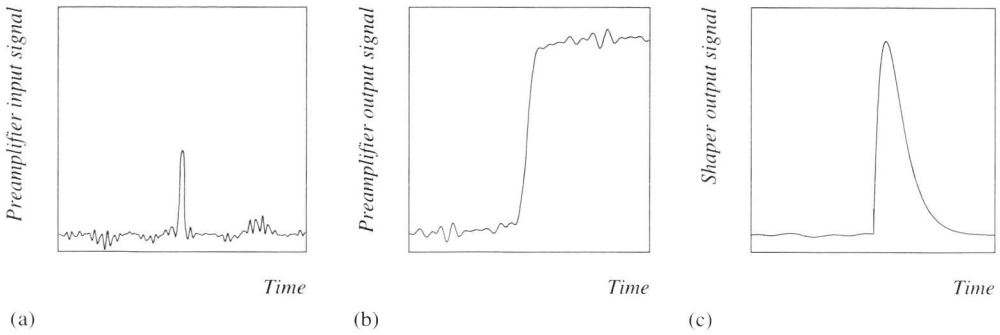

Figure 3.9: The signal coming from the silicon sensor at the input (a) and at the output (b) of the preamplifier and the resulting shaped signal (c).

studies. The data consist of the strip addresses and the number of ADC counts at each strip.

STRIP All channels above threshold and in accepted clusters are stored. The data consist of the strip addresses and the number of ADC counts. This data format is used in the offline event reconstruction.

CLUSTER The data processor evaluates clusters of strips. During the evaluation it stores the total charge of the cluster (measured in ADC counts) and the addresses and ADC counts of the begin and end strip of the cluster. This data stream is used to trigger events with the ZEUS global tracking trigger (GTT) [33–35].

3.1.4 Cluster and position reconstruction

Many of the properties of the MVD silicon sensors and read out chips were studied in a test beam experiment at DESY. In this test prototype sensors were placed on an optical bench between three reference detectors (these were also silicon strip detectors). The test beam consisted of electrons, in an energy range from 1 to 6 GeV. The electrons were triggered with coincidences of scintillator counters upstream and downstream the test stand.

The reference sensors were used to estimate the position of the hit on the prototype sensor. The residual of a hit was defined as the difference between the estimated position and the reconstructed position of a hit in the prototype sensor. First, the hit signal is studied and corrected for noise. Secondly, the position resolution is studied.

In figure 3.10a one event in a prototype MVD sensor is shown. The raw signal is measured for all 512 strips. Corrections are done for each chip and strip resulting in the corrected signal that is shown in figure 3.10b. The peak in the data is called a hit or a cluster. The surrounding strips fluctuate because of the (low) noise in the silicon and electronics.

A cluster is defined as a group of the strips which are above the noise threshold. The

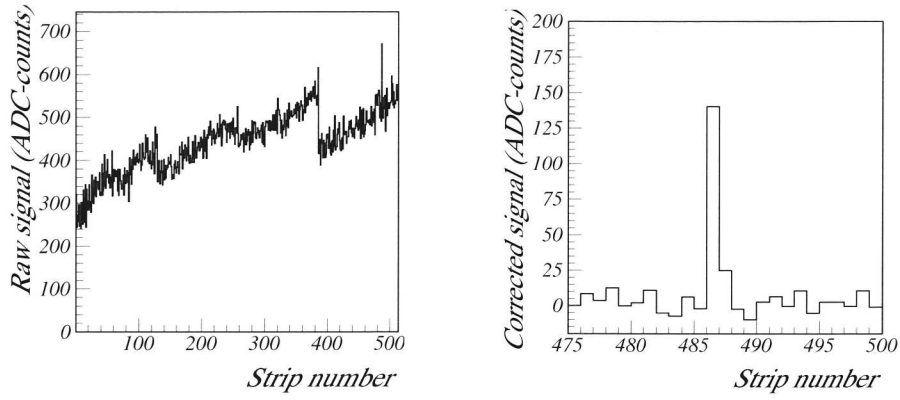

(a) (b)

Figure 3.10: Display of a test beam event in a MVD prototype sensor. In (a) is shown the raw signal for all 512 strips. In (b) is shown the clear signal after corrections.

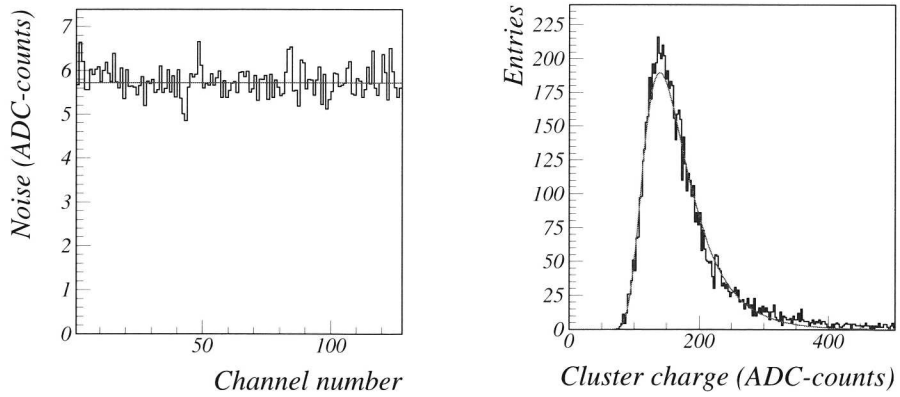

(a) (b)

Figure 3.11: In (a) is shown the noise levels of 128 channels. In (b) is shown the cluster charge distribution for the MVD prototype sensor.

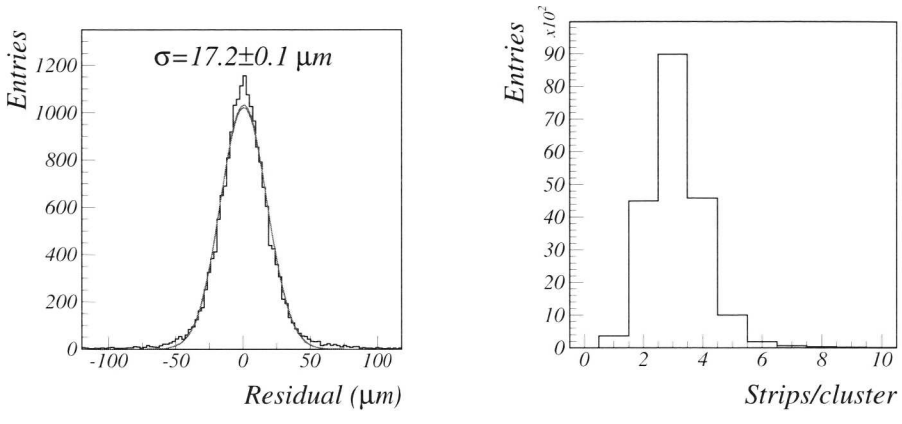

(a) (b)

Figure 3.12: Residual distribution using the cog algorithm and cluster size distribution using a threshold of $4\sigma_{\text{strip}}$ on the seed and $3\sigma_{\text{strip}}$ on the neighbours.

noise is determined for each strip separately in so called pedestal runs. These are runs with a random trigger and no beam. In figure 3.11a the noise is shown for 128 channels. The average noise level is 5.7 ADC counts. The strips that are in the cluster are selected with a cluster finding algorithm. Normally one looks for a strip which is higher than four times the strip noise ($4\sigma_{\text{strip}}$). Then the neighbours are evaluated and if the strip is higher than $3\sigma_{\text{strip}}$ the strip is added to the cluster. In figure 3.11b the sum of the signal of all strips in the cluster is plotted (total signal or charge of a cluster). The Landau fit gives for the most probable energy loss 139.4 ADC counts. This yields a signal to noise ratio of 24.5 for this prototype sensor.

For the ZEUS experiment the clustering is done (on a similar way) on-line by the DSPs (digital signal processors). The following criteria are used for the 2002 to 2004 data:

- At least one strip above the seed threshold. The seed level is around 4-6 times the noise.
- The neighbouring strips are above the threshold. The threshold is set at 2-3 times the noise.
- A gap of one strip is allowed.

The next step is to use the found cluster to reconstruct the position of the hit. Various approaches exist to do this. Here is used the centre of gravity (cog) method which is the weighted mean of strips in the cluster:

$$x_{\text{cog}} = \frac{\sum_i Q_i * i}{\sum_i Q_i}, \tag{3.3}$$

where Q_i is the number of ADC counts for strip i. In figure 3.12a the distribution of the residuals (differences between the expected and measured hit positions) is shown and in figure 3.12b the cluster size distribution.

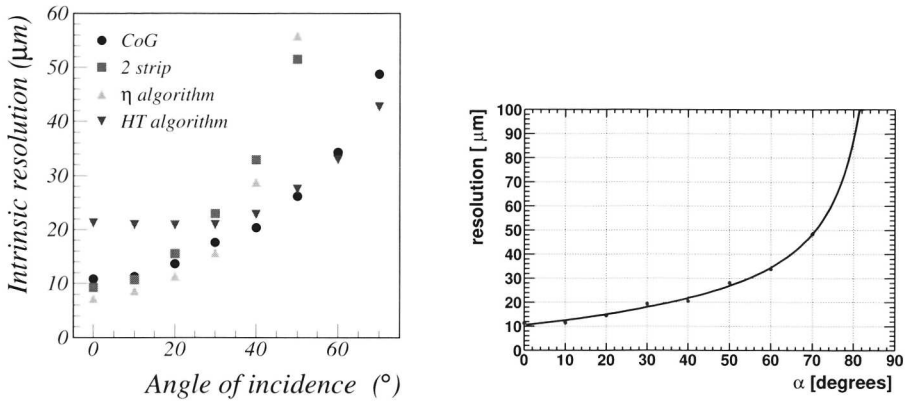

(a) (b)

Figure 3.13: In (a) the resolution of different position reconstruction algorithms are compared. Using the test beam experiment the dependence of the resolution could be estimated as a function of the angle of incidence. In (b) the resolution is calculated using the centre of gravity or weighted mean method for the MVD simulation. The line is the angular parameterisation for the resolution used in the reconstruction program.

Not only the position of the hit is important but also the uncertainty in the position is a necessary input for a good track fit. A precise hit will have a larger weight in the track fit than a less precise hit.

The angle of the track with the sensor is defined with respect to the normal of the prototype sensor plain. A track which passes the sensor at a larger angle induces charge on more strips. The cluster width increases and the standard position reconstruction gets worse. The prototype sensor was rotated in steps of 10° to study this effect.

One of the results of the MVD test program is shown in figure 3.13a. In the figure different position reconstruction algorithms are compared. These are:

- *Centre of gravity* The weighted mean of the cluster is a good method over the whole range of angles.
- *2 strip* Only the charge of the strips with the highest signal are used for the cluster. The performance worsens quickly for increasing angles.
- *η-algorithm* The two highest strips are taken and a correction is applied for the charge sharing which is not proportional with the inter strip position.
- *head-tail algorithm* The position is determined using the first and the last strip of the cluster and an extra term which depends on the charge fractions of these two strips. This method is the most accurate for large angles of incidence.

The results in this thesis are based on the centre of gravity position reconstruction, which gives the best overall performance. Figure 3.13b shows the resolution as determined in the Monte Carlo simulation of the MVD. The line is the parameterisation used

in the track fit to describe the uncertainty in the hit position. The same algorithm and parameterisation is used in data and Monte Carlo. In data an additional error is added in quadrature for the uncertainty of the position of the sensor inside the MVD (see section 3.2.1).

3.1.5 Cooling and cables

The heat dissipation of the Helix chips is about 2 mW per read out channel: with 128 channels per chip, and 4 chips per hybrid, this amounts to 1 W per hybrid or 10 W per ladder. A total heat dissipation of 300 W in the barrel and 120 W for the wheels is expected. To absorb the generated heat a water cooling system is used.

The water is distributed to the ladders and the wheels from a manifold inside the support tube (see figure 3.14). Stainless steel tubes with an inner diameter of 2.5 mm and a wall thickness of 0.1 mm, run underneath the hybrids and are integrated in the support structure (see figure 3.15). Thermal contact between the hybrid and the tube is established with heat conducting paste[1]. The connection between the manifold and the cooling tube is made via polyurethane tubes (outer diameter 4 mm, inner 2.5 mm), which are clamped with a spring onto the stainless steel tube. The input temperature of the water is 15 °C and the flow through one stainless steel tube (one ladder or wheel) is 0.25 l/m.

The MVD has to be supplied with the electrical power for the read out. The electronic racks are approximately 20 m away from the MVD. Figure 3.16 gives a schematic picture of the MVD readout chain. The electronics racks are placed outside the detector. A few meter from the MVD (behind the RCAL) the patch box is used to combine the electrical power, readout lines and control signals into combo cables each connected with a single module on the ladders or sector in the wheels. In addition there are cables for the bias voltage of the sensors.

The connection of the combo cables to the modules is done via a printed circuit board (PCB) with flexible connectors to the hybrids as can be seen in figure 3.15. The five combo cables run along one side of the ladder. The connection for the wheels is similar.

The available space in the MVD is small, so the volume of cables has to be minimised. The amount of copper is minimised to reduce the amount of material used for the vertex detector. The cables enter the MVD at the rear side as can be seen in figure 3.14. The cables and cooling tubes for the MVD wheels run outside the barrel ladders and are mounted against the MVD outer shell. This can be seen schematically in figure 3.22.

3.2 Construction

In section 3.1 the layout of the MVD was explained. Also the silicon strip sensors were discussed. A position resolution of 10 µm was achieved in the test beam experiment. To profit from this good position resolution in the trajectory fit the geometry of the detector should be very precisely known and stable, of the same order as the hit resolution.

[1] Dow Corning 340 Heat Sink compound

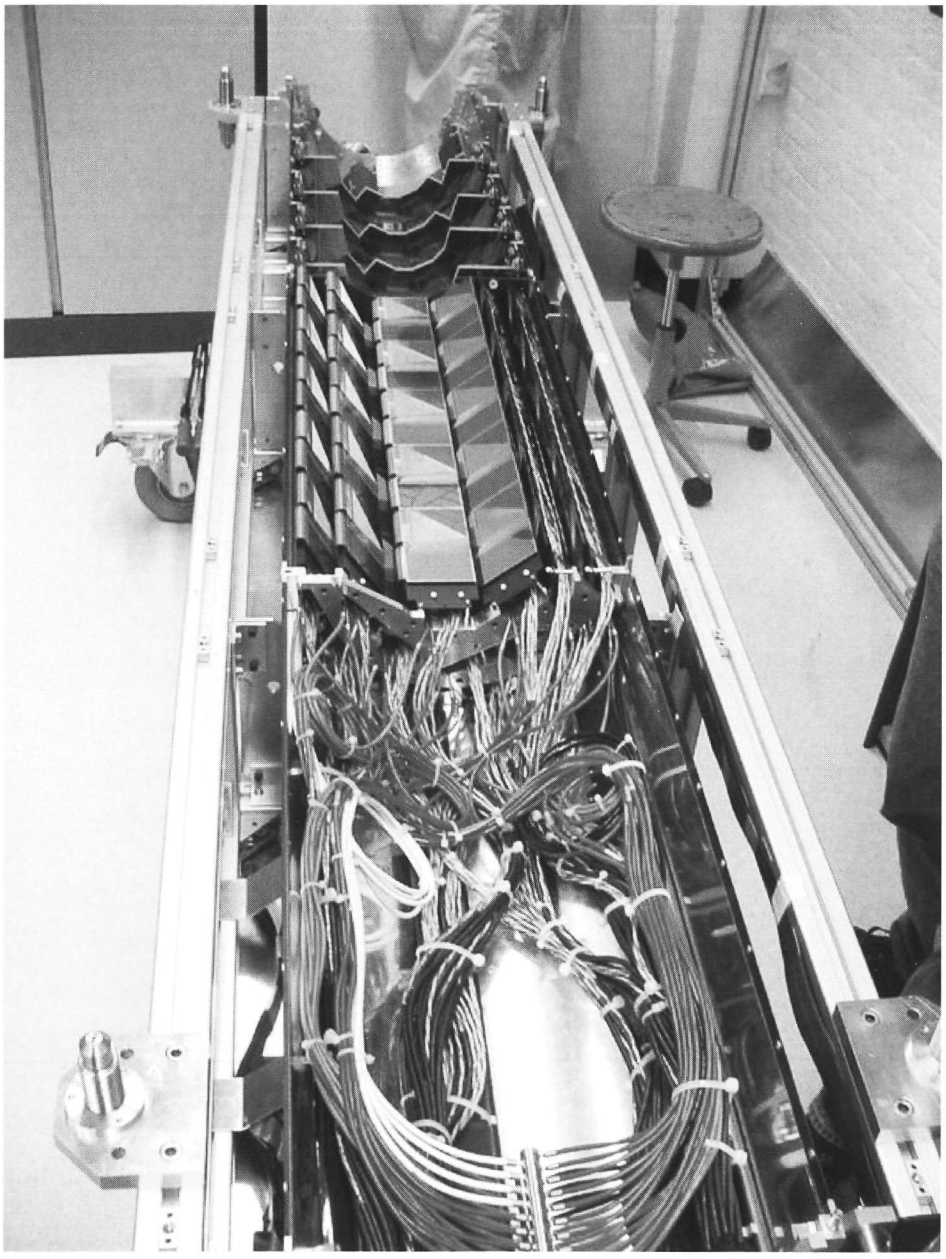

Figure 3.14: Photograph of the top half of the MVD. The cooling water is distributed from the manifold at the bottom of the picture.

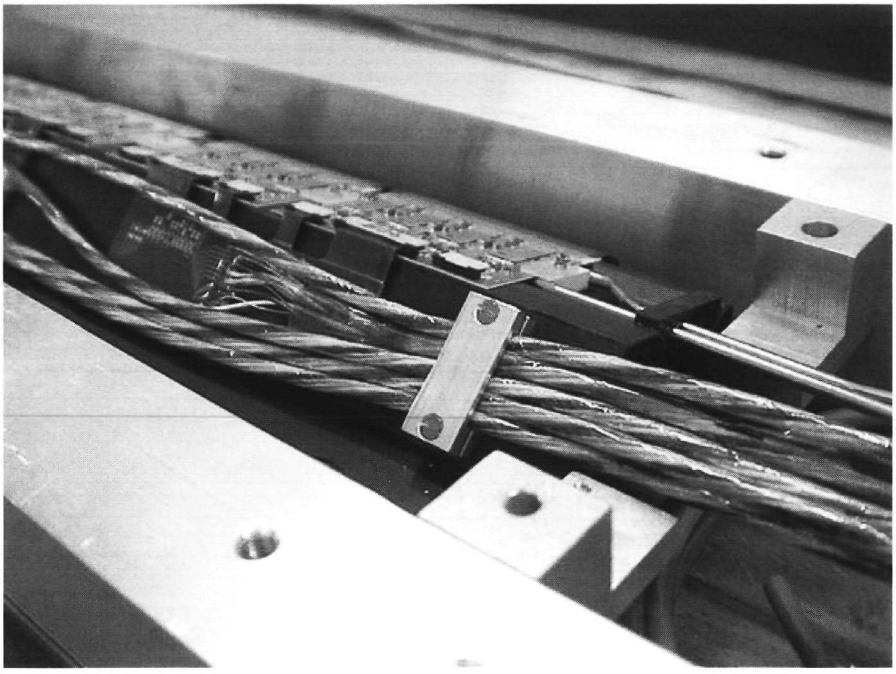

Figure 3.15: Photograph of a MVD ladder in the transport box. The cooling tube runs below the hybrids. The inflow and outflow is at the same side.

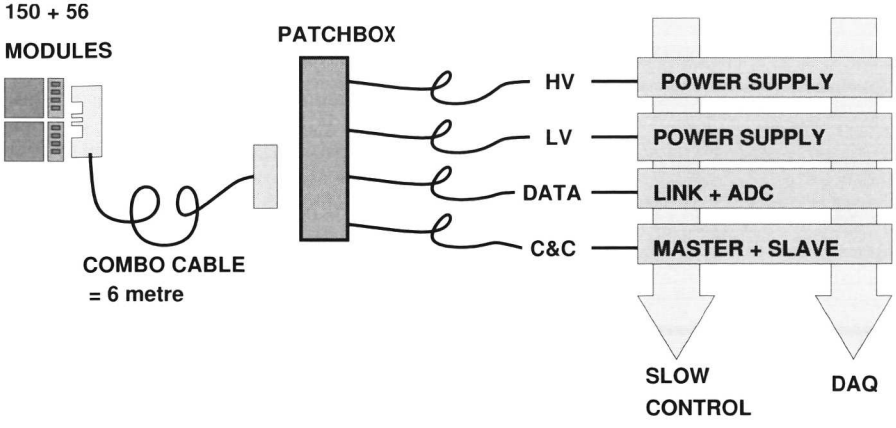

Figure 3.16: Schematic picture of the MVD electronics and cables.

Another requirement is that minimal and lightweight material should be used. If the total weight of the detector gets larger, the more the particles scatter in the material. This results in a deterioration of the track reconstruction. In this section the accuracy of the MVD construction is discussed. Then the resulting material distribution is investigated.

3.2.1 Mechanical precision

When constructing a detector like the MVD it is a fact that the mounting of detector parts is done with a certain inaccuracy. This leads to deviations from the default or design positions. Also the stability of detector has to be considered. The deformations of the objects, for example the ladders, due to changes in temperature or mechanical stress have to be known with a certain accuracy.

The knowledge of the precision of the construction is very important for the finding and fitting of the trajectories of charged particles. In other words the geometry of the detector has to be known as accurately as possible. With the alignment is meant: all knowledge about the positions of the individual parts of the detector.

Three levels of alignment are distinguished:

1. **design** This is the geometry as described by the design drawings of the MVD.

2. **survey** After assembly the positions of the detector parts are measured with respect to well defined points on the detector. From this an off-set from the design position can be determined.

3. **tracking** After the MVD is installed in ZEUS a sample of well measured tracks will be recorded. These tracks can be used to do an alignment fit algorithm which calculates the off-sets from the assumed geometry. This is described further in section 5.4.

In the end the tracking alignment is expected to be the most accurate description of the detector. The precision of the assembly and the survey after assembly is explained in detail in this subsection.

Assembly of the barrel section

The sensors have an intrinsic precision of a few microns, assuming the mask to mask alignment was 2 to 3 µm. The same holds for the uncertainty in the position of the alignment marks on the edge of the sensor with respect to the underlying strip pattern (see figure 3.17). The alignment markers consist of three different patterns on an area of $0.2 \times 0.6\,\mathrm{mm}^2$ and were used both for the construction and for the survey measurements after the assembly.

The module was produced in two half modules. Using precision rotational and translation tools the sensors were glued together with a precision of 10 µm. After assembly and curing of the glue the precision was confirmed with a microscope measurement [36]. The assembly was completed with a glass ear positioned with the same precision at the outer edge of one of the sensors.

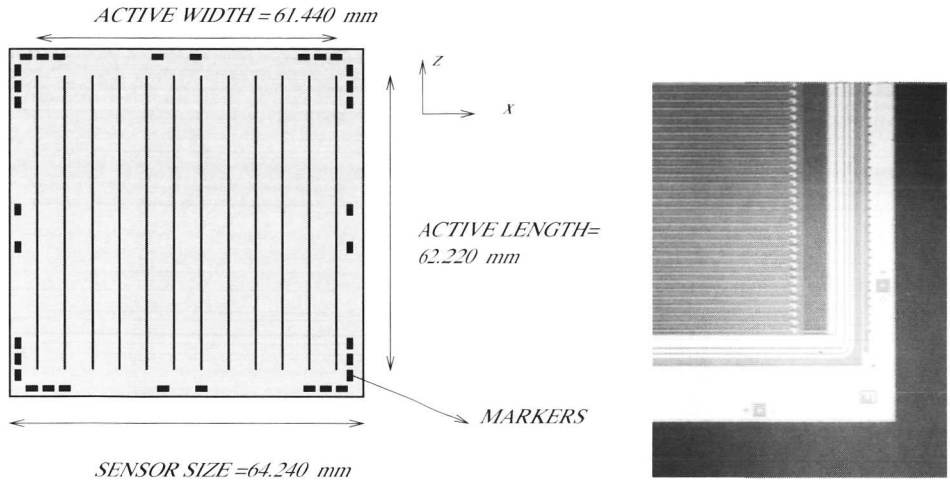

Figure 3.17: In (a) is shown a MVD sensor with the position of the alignment markers. In (b) is shown a photograph of a corner of the silicon sensor. Two alignment markers are seen.

The next step was the mounting of the half modules on the ladder. This was also done using precision tools. The assembly went in two steps. First the outer layer of five half modules was mounted, then the next layer of 5 half modules (inner layer) was mounted. On the ladder three precision ceramic bullets (two on the rear side and one on the front side of the ladder) were mounted.

For the assembly of one layer all 5 half modules were held in place with vacuum tools. The alignment of the half modules with respect to each other relied on the survey marks on the glass ears. The ladder was then glued onto the modules via plastic spacers. In this step the three alignment bullets on the ladder were in a well defined position with respect to the module positions. After mounting, the ladder was placed under a 2-dimensional survey microscope to check the positions of the sensor on the ladder. In figure 3.18 the off-sets of the half modules of the ladder outer layers are shown. Most half modules are within 10 μm of their design positions.

The construction of the barrel was done per half cylinder. The ball-like marker on the front side of the ladder, fits inside a hole inside the forward barrel flange. Along the beam line the ladder is free to expand, but in the perpendicular plane the centre of the hole is within 10 μm of the design position (see figure 3.19a). On the rear side of the barrel section, the ladders were screwed onto the (aluminium) rear barrel flange.

After the assembly of each layer (respectively 8, 5 and 2 ladders) a 3-dimensional survey was performed. The x and y position of the hole, the z position of the forward bullet, the x, y and z position of the two rear bullets of each ladder were measured. The results for the off-set for each ladder are shown in figure 3.19. In the z direction the average spread for the ladders is 50 μm.

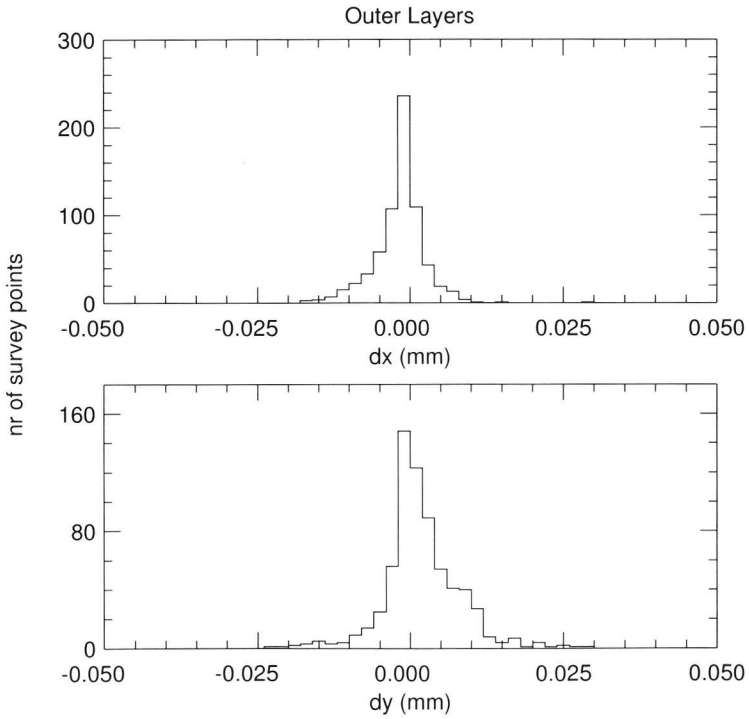

Figure 3.18: The survey of the outer layer of the ladders gives the precision in x and y of the half module placement.

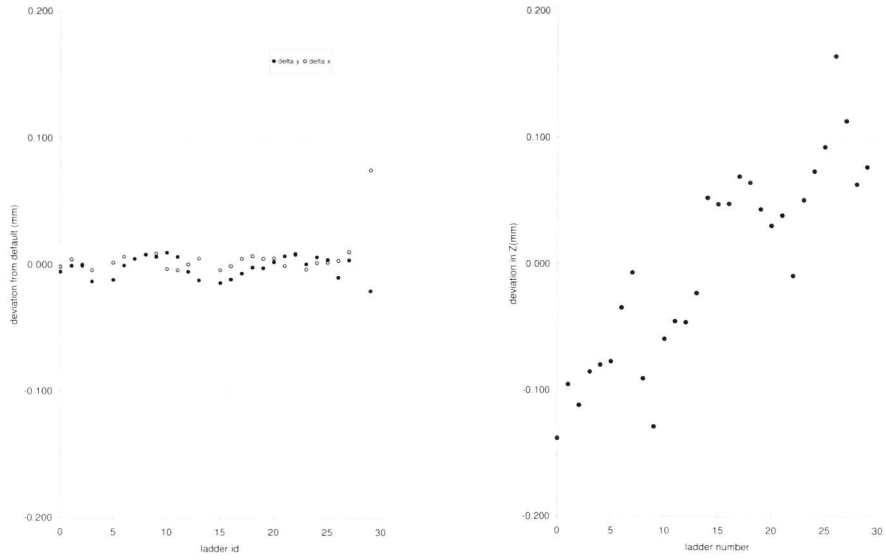

(a) (b)

Figure 3.19: Results from the 3-dimensional survey. The off-sets from the design value are shown for the x and y position of all 30 MVD ladders in (a) and the z position off-sets are shown in (b).

The placement of the MVD inside the CTD (done in March 2001) was a very delicate and precise operation. The xy position is fixed, but the relative z position of CTD and MVD has to be calibrated using tracks (see section 5.4).

The assembly and survey of the wheels was similar to that of the barrel. Alignment offsets of the same order as those in the barrel are expected. Along the MVD shell five laser beams are used to monitor the stability of the detector, both internally and with respect to the CTD. This system is described extensively elsewhere [37].

3.2.2 Dead material

In this section the dead material inside the microvertex detector is described. The active material in the MVD is the silicon in which the signals are generated. The dead material consists of a list of objects, for example: beam pipe, readout chips, carbon ladders, cooling pipes and water.

For a particle traversing one MVD ladder the amount of traversed material is on average 3% of a radiation length. This radiation length is calculated by "smearing out" all ladder components over the ladder surface. In figure 3.20 the contribution of the different components is shown. The active part (the silicon) accounts for 25% of all ladder material.

The more material a particle traverses the more it can scatter. In the offline track

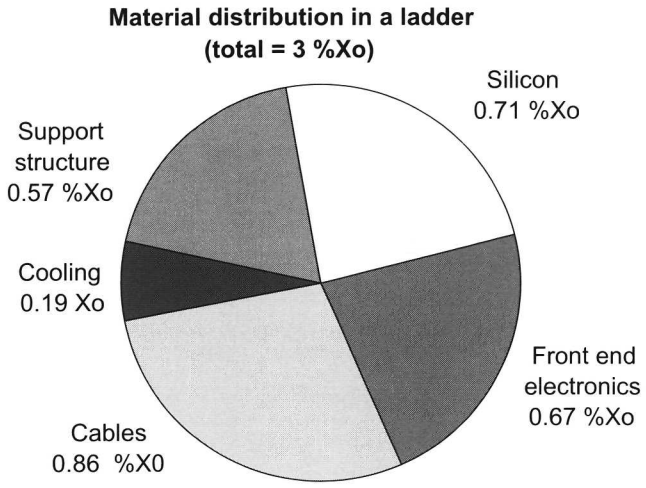

Figure 3.20: The various contributions to the radiation length of one ladder. The estimated average for a ladder is 3% of a radiation length (X_0).

fit corrections for scattering effects can be included. For this a detailed description of the detector is necessary. However it is impossible to add every microscopic detail to the simulation. This would lead to very long simulation and reconstruction times.

Two types of material are distinguished. The first is material with well known shapes and positions. For example the Helix chips on the hybrids. These positions are known within a few 100 µm. The second is material with less known shape and less stable positions. For example the cables on the ladders and inside the rear of the MVD. In this case the amount of material is estimated and averaged inside a certain volume.

The material description for the MVD consists of a list of components and a list containing the positions of these components. Each component is described as a box, disk or a cylinder with certain material properties (silicon, stainless steel, etc.). An effort has been made to store all relevant information from the MVD design drawings in computer files. These files are both input for the MVD simulation and reconstruction.

How is the amount of radiation lengths in the offline trajectory fit estimated? All material is projected on planes and cylinders. The point of intersection is determined and transformed to a local coordinate inside the plane or cylinder. For example the hybrid plane of a ladder is crossed. All subcomponents (hybrids, cooling pipes) are evaluated. If a subcomponent covers the point of intersection its contribution to the radiation length is calculated. This algorithm is iterative, so for example after a hybrid is intersected the components of the hybrid (chips) are evaluated. The last step is to correct the radiation length for the angle of incidence.

Inside the MVD there are 30 similar ladders. The material description for them is

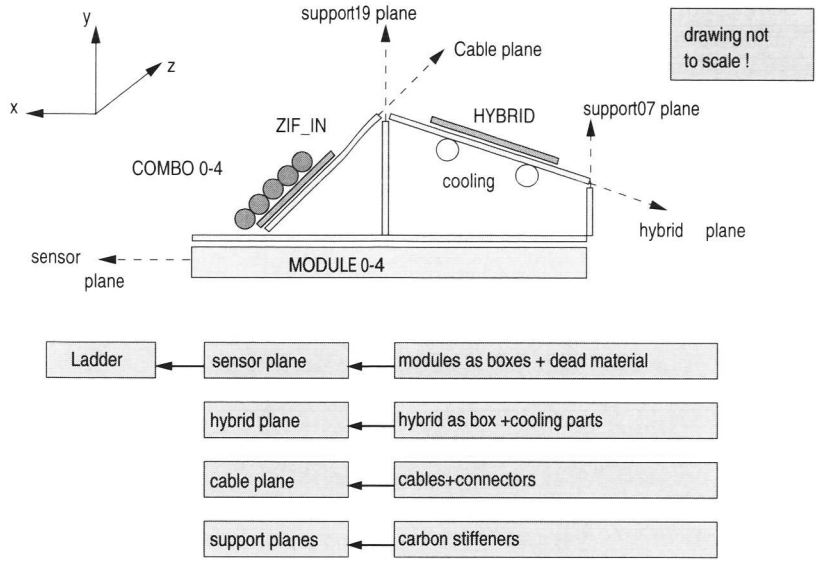

Figure 3.21: The material in an MVD ladder. It is described as a number of different planes

equal. The material of a ladder is described in five planes. This can be seen in figure 3.21. Inside each plane the various components like sensors, hybrids and cables are defined. Because all hybrids are the same also a generic description of a hybrid is made.

As examples two computer generated pictures using the component database are shown in figures 3.22 and 3.23. In figure 3.22 the MVD outer shell, flanges and cables to the wheels are displayed. The material of the cables and cooling tubes in the rear MVD are averaged over a large cylinder, which is also visible in the figure.

An example where the number of radiation lengths is calculated is shown in figure 3.24 where the hybrid plane of the ladder is scanned. The structure of cooling pipes, hybrids and chips is clearly seen.

In the next chapter is discussed how the measured hits are used to give an actual description of the track of the particle. How the material distribution in the MVD contributes to the uncertainty in the trajectory is also described.

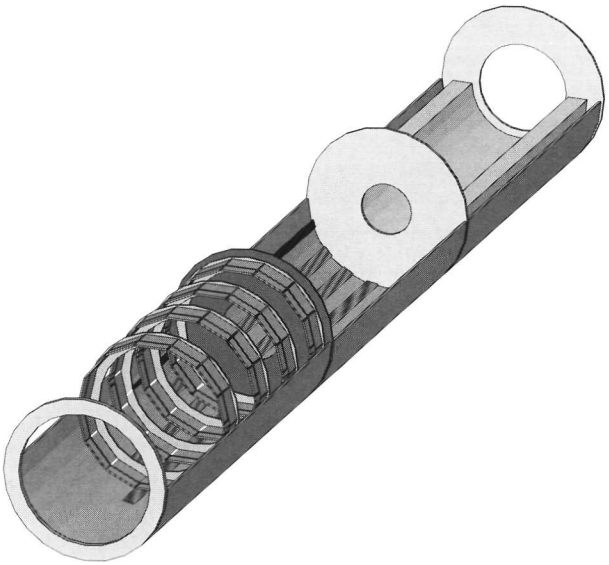

Figure 3.22: Description of the material in the MVD.

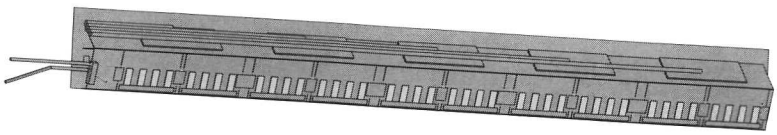

Figure 3.23: Description of the material in a barrel MVD ladder.

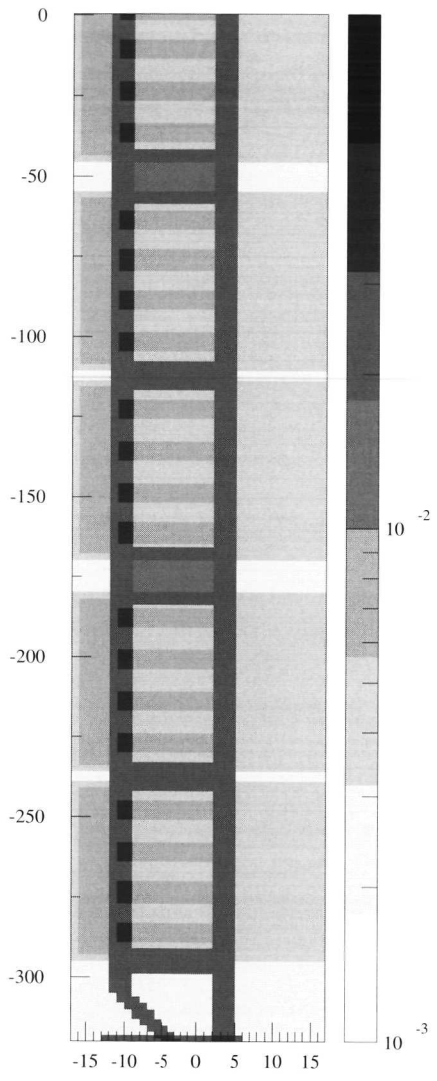

Figure 3.24: Number of radiation lengths in the "hybrid plane" of the ladder. The structure of the cooling pipes and hybrids is clearly seen. Approximately 4% of a radiation length is traversed when a particle traverses the material of a cooling pipe and a read out chip.

Chapter 4

Track fitting

In the previous chapters it was discussed that a microvertex detector was installed by the ZEUS experiment during the HERA upgrade. Before the upgrade (from 1992 to 2000) the central tracking detector (CTD) was the main tracking component. The MVD has been designed to improve the tracking capabilities of ZEUS, by providing additional hits close to the interaction region.

Most charged particles in the MVD give at least 3 space points, although there is enough redundancy to find tracks with the MVD only, the central tracking detector is still important in this task. The MVD is expected to improve the tracking precision significantly.

The outline of this chapter is as follows. In section 4.1 the reconstruction of the tracks in the MVD is explained. With the help of the Kalman filter hits are found and fitted "along the way" and the trajectory of the charged particles is estimated. Multiple scattering effects can be estimated and are included in the track fit. The strategy of the fitting procedure is discussed in section 4.2. Then the Kalman filter vertexing technique is explained in section 4.3. This algorithm is used to find the primary and secondary vertices.

The track fit is used to study the performance of the MVD in chapter 5 and the vertex reconstruction is applied in the physics studies of chapter 6.

4.1 Track reconstruction

Basically, the reconstruction of tracks consists of two phases. The measured hit positions have to be assigned to a candidate track. This is called the pattern recognition phase. Secondly, the track fit phase estimates the trajectory using the hit positions belonging to the track. Using the Kalman filter hits can be found and fitted simultaneously. More on the used Kalman filter is explained in section 4.1.2. First it is discussed how the trajectory of a charged track is parametrised.

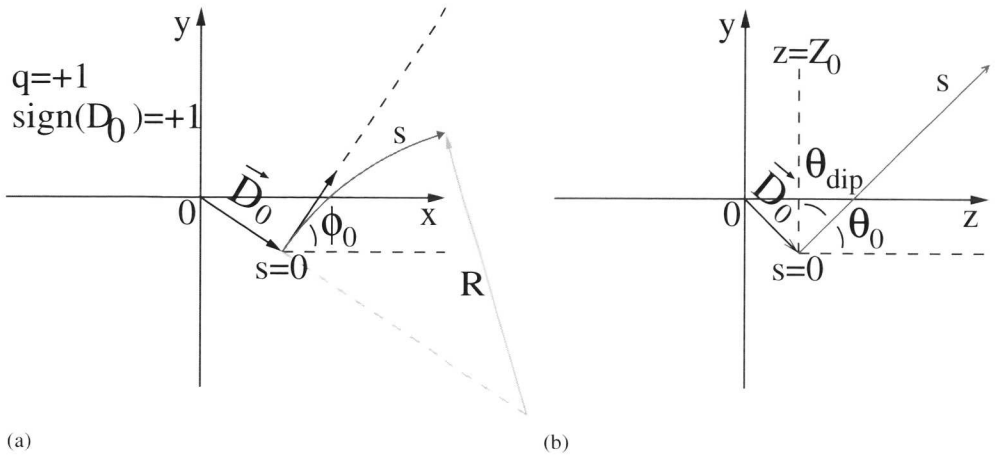

(a) (b)

Figure 4.1: The track of a charged particle in a uniform magnetic field, projected on the xy plane (a) and on the yz plane (b). The 3-vector $\vec{D}_0$ is projected on the xy plane (a) and on the yz plane (b).

4.1.1 Track parameterisation

The motion of a charged particle inside a uniform magnetic field can be described by a helix parameterisation. Inside the MVD the magnetic field is assumed to be homogeneous (see section 2.2.1). Only in the region of the most forward wheel there is a deviation of a few percent. The magnetic field is aligned in the z direction[1] and is constant in magnitude: $\vec{B} = (0, 0, B_z)$, where $B_z \approx 1.43$ Tesla.

The following parameter vector describes the trajectory of the helix in the global Cartesian (x, y, z) frame:

$$\vec{p} = (W,\ T,\ \phi_0,\ D_0,\ Z_0). \tag{4.1}$$

The curvature of the track is the charge over the radius: $W = q/R$. In figure 4.1 the used parameters are explained graphically. The parameter T is defined as $\tan\theta_{\text{dip}}$ and $\theta_{\text{dip}} = 90^\circ - \theta$. An important vector is $\vec{D}_0$, the point of closest approach. The angle ϕ_0 gives the direction of the track at the point of closest approach projected on the xy plane. The parameter D_0 is the distance from the origin to the point of closest approach, projected on the xy plane. Note that D_0 is signed. The sign is given by the product of $\vec{D}_0 \wedge \vec{v}$. The vector $\vec{v}$ is the direction of the track at the point of closest approach. The sign of the z component of the cross product gives the sign of D_0. The parameter Z_0 is the z component of $\vec{D}_0$.

[1]The ZEUS coordinate system is a right-handed Cartesian system, with the z axis pointing in the proton beam direction and the x axis pointing towards the centre of HERA. The coordinate origin is at the nominal interaction point.

When these parameters are used to describe the track, $\vec{D}_0$ is:

$$\vec{D}_0 = \begin{pmatrix} x_0 \\ y_0 \\ z_0 \end{pmatrix} = \begin{pmatrix} D_0 \sin\phi_0 \\ -D_0 \cos\phi_0 \\ Z_0 \end{pmatrix}. \tag{4.2}$$

The trajectory in x, y and z is given by the following parameterisation:

$$\begin{pmatrix} x \\ y \\ z \end{pmatrix} = \vec{D}_0 + \begin{pmatrix} \frac{1}{W}\cos\phi_0 \sin(Ws_\perp) + \frac{1}{W}\sin\phi_0[1-\cos(Ws_\perp)] \\ \frac{1}{W}\sin\phi_0 \sin(Ws_\perp) - \frac{1}{W}\cos\phi_0[1-\cos(Ws_\perp)] \\ Ts_\perp \end{pmatrix}. \tag{4.3}$$

Here the variable $s_\perp = s\sin\theta$, where s is the distance along the trajectory ($s = 0$ at the point of closest of approach).

The task of the track fit is to give the best possible estimate of the five track parameters, based on the measurements and their uncertainties.

4.1.2 Kalman filter track fit

The Kalman filter is named after Rudolf E. Kalman, who in 1960 published his famous article describing a recursive solution to the discrete-data linear filtering problem [38]. The Kalman filter estimates the state of a dynamical system at any time. The dynamics can be distorted by noise sources. The Kalman filter optionally makes optimal use of new measurements and their measurement noise. In the (linear) Kalman filter the measurements are linearly dependent on the state parameters.

The Kalman filter is applied in many fields of science and engineering. The Kalman filter has been introduced in high energy physics by R. Frühwirth for the tracking of particles [39]. In this case the state is the five vector of track parameters and the measurements are the hits.

Doing a track fit with the Kalman filter gives advantages with respect to the more traditional least squares method. The Kalman filter track fit evaluates the measurements (hits) separately. The least squares fit fits all hits simultaneously.

Example of a least squares track fit

How to do a least squares track fit? Assume that three space points: $(\vec{r}_1, \vec{r}_2, \vec{r}_3)$ are measured. These three points can be fitted to a helix, described by the parameterisation from equation 4.3. The example is depicted in figure 4.2. The least squares fit consists of the following steps:

- The measurements are in the vector $\vec{y}$. This is in this case a vector with 9 entries:

$$\vec{y} = (\vec{r}_1, \vec{r}_2, \vec{r}_3). \tag{4.4}$$

  where each position vector $\vec{r}$ has an x, y and z component.

- The uncertainty in the hit positions are stored in the 3×3 covariance matrices: C_1, C_2 and C_3. Then the 9×9 total covariance matrix is:

$$V_y = \begin{pmatrix} C_1 & 0 & 0 \\ 0 & C_2 & 0 \\ 0 & 0 & C_3 \end{pmatrix}. \tag{4.5}$$

  The errors of the hits are assumed to be independent from each other.

- The estimated positions are described by the vector function $\vec{f}(\vec{p}, s)$, which has 9 entries. It is a function of the track parameters $\vec{p}$ and the coordinate along the track s.

- The χ^2 is written as:

$$\chi^2 = \left(\vec{y} - \vec{f}\right)^T V_y^{-1} \left(\vec{y} - \vec{f}\right) \tag{4.6}$$

  The task of the fit is to find the parameters p_j which give the minimal χ^2: $\delta\chi^2/\delta p_j = 0$. This is called χ^2 minimisation.

- From equation 4.3 it is seen that the track model is not linear in its parameters. So the trajectory has to be linearised near the measured points. This is done with a derivative matrix called H. In this case H is a 9×5 matrix. In tensor notation the derivative matrix is represented as:

$$H_{ij} = \frac{\partial y_i}{\partial p_j}, \tag{4.7}$$

  calculated near all three points ($s = s_1$, s_2 and s_3), where y_i represents the hit coordinates. The following equation gives the approximation of the change of the estimated hit positions $\vec{f}$ when the trajectory changes from $\vec{p}_0$ to $\vec{p}$:

$$\vec{f} = \vec{f}(\vec{p}_0, s) + H(\vec{p} - \vec{p}_0). \tag{4.8}$$

- The next step is to find the values of the vector $\vec{p}$ which minimise the χ^2. This is done numerically. The algorithm starts with a rough estimate of the track. In the example a straight line through two of the three points is taken. Starting from the estimate $\vec{p}_0$ the new estimate $\vec{p}_1$ is:

$$\vec{p}_1 = \vec{p}_0 + V_{\vec{p}_1} H^T V_{\vec{y}}^{-1} (\vec{y} - \vec{f}(\vec{p}_0)), \tag{4.9}$$

  with

$$V_{\vec{p}_1} = (H^T V_{\vec{y}}^{-1} H)^{-1}. \tag{4.10}$$

  This is repeated until a minimum in χ^2 is found. The example in figure 4.2 shows how after n steps the trajectory fits the three points.

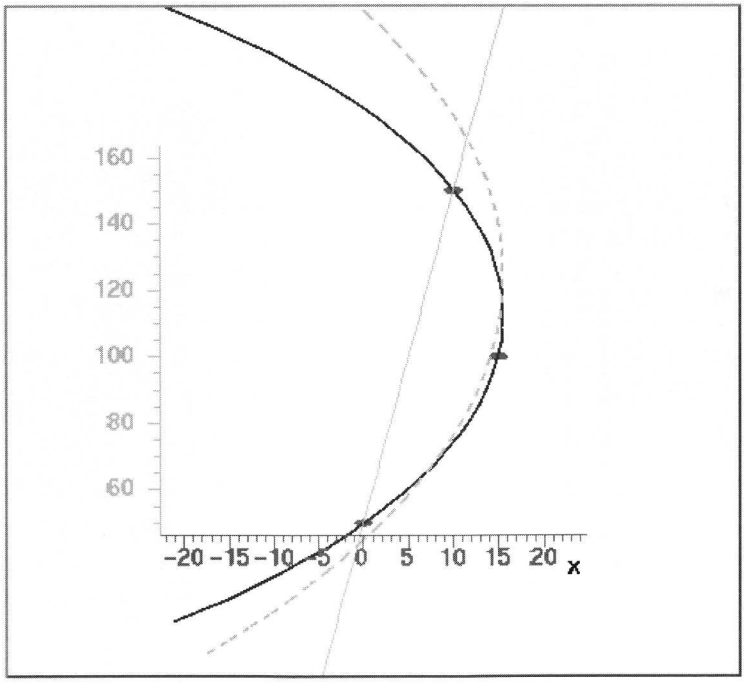

Figure 4.2: Result of the least squares fit for the starting value, after the first iteration and the 51st iteration.

The least squares fit has a number of disadvantages. In this example it is seen that when the helix has to be fitted to a large number of hits, matrices become large and then the computing time increases. The inversion of a matrix of order n needs in general $\mathcal{O}(n^3)$ steps. Also when multiple scattering is included, the hit uncertainties are not independent anymore. This results in off-diagonal entries in the hit error covariance matrix. Furthermore the method is not flexible. If a wrong hit has been used, the complete fit must be repeated from the start.

With the help of the Kalman filter these disadvantages can be overcome. First it is explained what is meant by measuring a hit in a local coordinate frame instead of a global coordinate frame. This is useful when the derivative matrix (or vector) of a Kalman filter step is discussed.

Local and global coordinate frames

In the previous example the hit positions were measured in the global coordinate frame. In the MVD hits are measured locally in the silicon strip sensors. An algorithm is used that calculates the intersection of a track with such a sensor. This intersection algorithm predicts a coordinate $\vec{r}_s$ which is expected to be near the hit. The distance along the track at this point is s. The position and orientation of the sensors in the MVD are well known. With the help of this geometry information $\vec{r}_s$ can be transformed to a locally measured coordinate.

For the track fit it is necessary to know the dependence of the track parameters (explained in section 4.1.1) to a change of the coordinate of the hit. In the following text this dependency is explained in detail.

In the global coordinate frame the axes are labelled x, y and z. The position and the orientation of the silicon strip sensors in the MVD are described by the following three vectors:

- The centre of the sensor inside the MVD frame $\vec{c}$.
- The normal of the sensor inside the MVD frame: the unit vector $\hat{y}'$
- The direction of measurement inside the MVD frame: the unit vector $\hat{x}'$

The direction of $\hat{z}'$ is given by $\hat{z}' = \hat{x}' \wedge \hat{y}'$ and is the direction along the read out strips of the silicon sensors. The direction of $\hat{x}'$ is in the positive measurement direction. In this case this is the direction of the increasing strip number. This is important since two half modules are mirror-images and the $\hat{x}'$ direction reverses.

The used vectors and coordinate systems are explained graphically in figure 4.3. In figure 4.3a an $r\phi$ hit, projected in the xy view, and in figure 4.3b a z hit, projected in the yz view, are shown. The derived track fit equations are also valid for the wheel hits.

The difference between the centre of the sensor and the coordinate of the intersection in the local frame is given by $\vec{D}$ and can be obtained with a rotation and a translation:

$$\vec{D} = D_x\hat{e}_x + D_y\hat{e}_y + D_z\hat{e}_z = R(\vec{r}_s - \vec{c}). \tag{4.11}$$

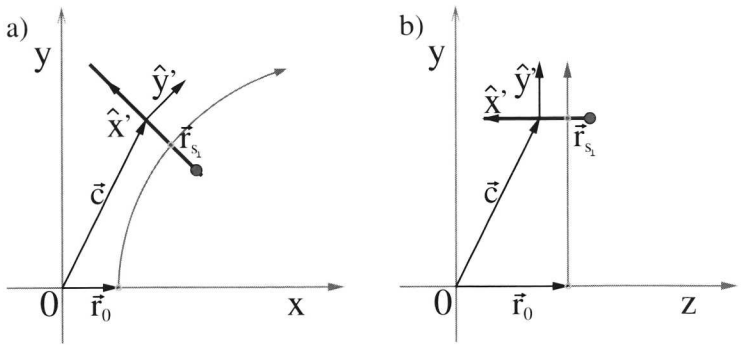

Figure 4.3: The track intersects the sensor at $\vec{r}_s$. The direction of measurement is $\hat{x}'$. Both for an $r\phi$ hit (a) and for a z hit (b) a change in the track parameters changes the position of the intersection. The correlation of the local sensor coordinate and the track parameters is derived in the text.

Here R is the rotation matrix of the sensor and D_y is zero (because the intersection is inside the plane) and D_x is the local coordinate of the intersection in the measurement direction ($\vec{x}'$). Note that $\vec{D}$ is not the same as the track parameter D_0. D_x is assumed to be not too far off from the reconstructed hit position in the silicon strip sensor.

The derivatives of the local coordinate with respect to the track parameters are calculated using the "rotated derivatives" from the global coordinate: $\frac{\partial \vec{D}}{\partial \alpha_i} = R\frac{\partial \vec{r}}{\partial \alpha_i}$. The index i runs from 1 to 5 and α_i is respectively (W, T, ϕ_0, D_0, Z_0). The derivatives $\frac{\partial \vec{r}}{\partial \alpha_i}$ can be written in the following form (where $s_\perp = s \sin\theta$):

$$\frac{\partial \vec{r}}{\partial \alpha_i} = \vec{a}_i + \frac{\partial s_\perp}{\partial \alpha_i}\vec{b}. \tag{4.12}$$

The vectors $\vec{a}_i$ and $\vec{b}$ are short notations for longer terms which are given at the end of this section.

The values for $\frac{\partial s_\perp}{\partial \alpha_i}$ can be calculated using the following constraint:

$$\frac{\partial D_y}{\partial \alpha_i} = \hat{e}_y \cdot \frac{\partial \vec{D}}{\partial \alpha_i} = \hat{e}_y \cdot R\frac{\partial \vec{r}}{\partial \alpha_i} = 0. \tag{4.13}$$

The rotated derivatives have no contribution in the y' direction. Using equation 4.12 in equation 4.13 the values for derivatives of $s_\perp$ are:

$$\frac{\partial s_\perp}{\partial \alpha_i} = \frac{-\hat{e}_y \cdot R\vec{a}_i}{\hat{e}_y \cdot R\vec{b}} \tag{4.14}$$

The derivatives for D_x follow from:

$$\frac{\partial D_x}{\partial \alpha_i} = \hat{e}_x \cdot \frac{\partial \vec{D}}{\partial \alpha_i} = \hat{e}_x \cdot R\frac{\partial \vec{r}}{\partial \alpha_i}. \tag{4.15}$$

With the use of equation 4.12 and 4.14, the final equation, which gives the derivatives of the local "measured" coordinate with respect to the track parameters, is:

$$\frac{\partial D_x}{\partial \alpha_i} = \hat{e}_x \cdot \left(R\vec{a}_i - R\vec{b}\,\frac{\hat{e}_y \cdot R\vec{a}_i}{\hat{e}_y \cdot R\vec{b}} \right) \tag{4.16}$$

The vectors $\vec{b}$ and $\vec{a}_i$ are defined in terms of the track parameters:

$$\vec{b} = \begin{pmatrix} \cos\phi_0 \cos(Ws_-) + \sin\phi_0 \sin(Ws_\perp) \\ \sin\phi_0 \cos(Ws_-) - \cos\phi_0 \sin(Ws_-) \\ T \end{pmatrix}. \tag{4.17}$$

$$\vec{a}_W = \begin{pmatrix} -\frac{1}{W^2}(\cos\phi_0 \sin(Ws_\parallel) + \sin\phi_0[1 - \cos(Ws_-)]) + \frac{s_+}{W} b_x \\ -\frac{1}{W^2}(\sin\phi_0 \sin(Ws_-) - \cos\phi_0[1 - \cos(Ws_-)]) + \frac{s_+}{W} b_y \\ 0 \end{pmatrix}. \tag{4.18}$$

$$\vec{a}_T = \begin{pmatrix} 0 \\ 0 \\ s_\perp \end{pmatrix}. \tag{4.19}$$

$$\vec{a}_{\phi_0} = \begin{pmatrix} D_0 \cos\phi_0 - \frac{1}{W}(\sin\phi_0 \sin(Ws_\parallel) - \cos\phi_0[1 - \cos(Ws_\perp)]) \\ D_0 \sin\phi_0 + \frac{1}{W}(\cos\phi_0 \sin(Ws_-) + \sin\phi_0[1 - \cos(Ws_-)]) \\ 0 \end{pmatrix}. \tag{4.20}$$

$$\vec{a}_{D_0} = \begin{pmatrix} \sin\phi_0 \\ -\cos\phi_0 \\ 0 \end{pmatrix}. \tag{4.21}$$

$$\vec{a}_{Z_0} = \begin{pmatrix} 0 \\ 0 \\ 1 \end{pmatrix}. \tag{4.22}$$

$$\tag{4.23}$$

Kalman track fit algorithm

The Kalman filter does a least squares fit for each hit separately. It is assumed that there is some starting information about the track coming from a rough pattern recognition or another detector component. The idea is to evaluate from outside to the inside all the hits near the start track. Also the amount of material encountered can be calculated and included in the track fit. The Kalman filter track fit algorithm consists of three basic operations:

Predict Predict the next state from the current state.

Filter Estimate the next state using a measurement and the predicted state.

Smooth Update the previous state using the current filtered state.

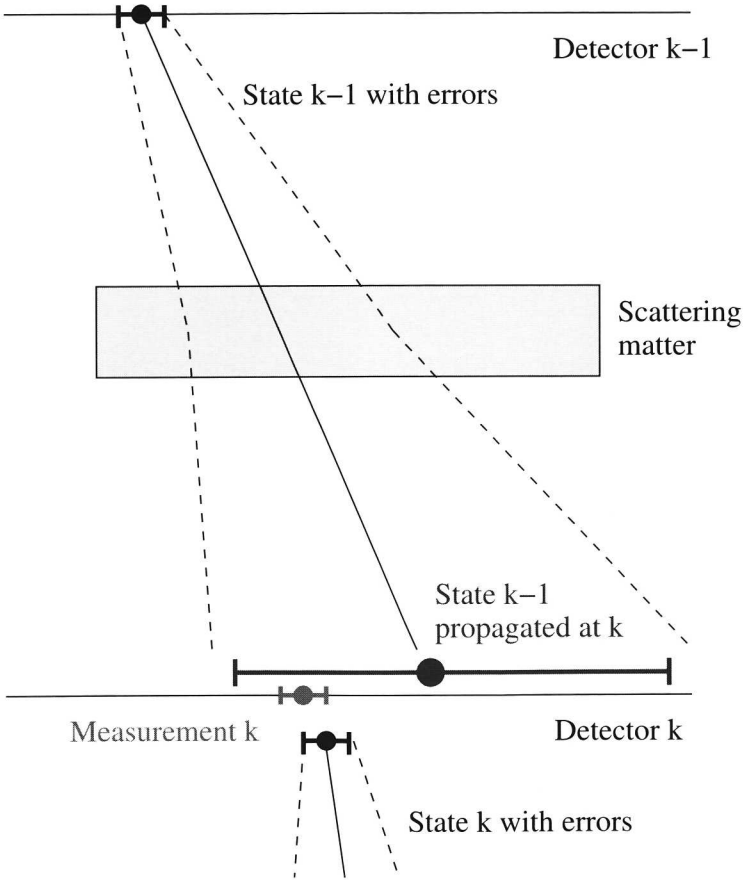

Figure 4.4: Example of a Kalman prediction step from detector $k-1$ to k (including scattering in material) followed by a filter step using a measurement in detector k.

The prediction step

Figure 4.4 shows schematically what happens in the Kalman track fit. The initial state is track $\vec{p}_{k-1}$ with covariance $V_{\vec{p}_{k-1}}$. In the prediction step the track is propagated to the next measurement plane. (That is a silicon sensor.)

Because the layers in the MVD are thin, the energy loss of the track is neglected. Although the state vector stays the same, the covariance of the track changes. The track covariance increases due to multiple scattering.

After propagation the state vector and the covariance are:

$$\vec{p}_k = \vec{p}_{k-1} \tag{4.24}$$

$$V_{\vec{p}_k} = V_{\vec{p}_{k-1}} + M_k, \tag{4.25}$$

where M_k is the contribution of the multiple scattering to the track's covariance between plane $k-1$ and k. To keep the notation simple for the filter step, the state and its covariance after the prediction step are defined as $\vec{p}_{k-1}$ and $V_{\vec{p}_{k-1}}$.

The filter step

In the filter step the trajectory of the particle is fitted to the current hit k which has an uncertainty in the reconstructed position of σ_k. The weight of the hit is proportional to $1/{\sigma_k}^2$. So if the hit has a small error, then the trajectory is pulled more strongly towards this hit. Also the covariance of the track affects the result of the fit. A very precisely measured track is pulled less strongly than a track with large covariance.

An important quantity in the fit is the difference between the measured hit position and the predicted hit on the silicon sensor. This quantity is called Δy, in case of a strip detector this distance is a scalar.

The change in the expected position as a result of a change in the track parameters is linearised as follows:

$$\delta = A_k \left(\vec{p}_k - \vec{p}_{k-1}\right), \tag{4.26}$$

where $\vec{p}_k$ is the parameter vector after the filter step and A_k is the derivative matrix as was derived in equation 4.16. So the quantity δ represents the change in the estimated position after the filter step has been done.

It is instructive to see the $\Delta\chi^2$ of a filter step:

$$\Delta\chi^2 = \left(\Delta y_k - A_k \Delta\vec{p}\,\right)^T \frac{1}{\sigma_k^2} \left(\Delta y_k - A_k \Delta\vec{p}\,\right) + \left(\Delta\vec{p}\,\right)^T V_{\vec{p}_{k-1}}^{-1} \left(\Delta\vec{p}\,\right), \tag{4.27}$$

with

$$\Delta\vec{p} = \left(\vec{p}_k - \vec{p}_{k-1}\right). \tag{4.28}$$

The $\Delta\chi^2$ has two contributions: The deviation of the hit and the track before and after the fit. Both are weighted with their associative errors. What happens when multiple scattering is included? First the predicted covariance $V_{\vec{p}_{k-1}}$ of the track increases. Then from the χ^2 equation it is seen that a track with a large scatter (significantly affected by multiple scattering) decreases in weight. Hence, for the fit the hit becomes more important.

Requiring a minimum for $\Delta\chi^2$ the following solutions are found for $\vec{p}_k$ and $V_{\vec{p}_k}$:

$$\vec{p}_k = \vec{p}_{k-1} + V_{\vec{p}_k} A_k^T \frac{1}{\sigma_k^2} \Delta y_k, \tag{4.29}$$

$$V_{\vec{p}_k} = \left(A_k^T \frac{1}{\sigma_k^2} A_k + V_{\vec{p}_{k-1}}^{-1} \right)^{-1}. \tag{4.30}$$

In the case of a large scatter the (filtered) track covariance $V_{\vec{p}_k}$ increases. Consequently the change in the track parameters is larger. So again, a large scatter allows the fit to change the track more. The equations for $V_{\vec{p}_k}$ and $\Delta\chi^2$ can be written differently [40] to save computing time:

$$V_{\vec{p}_k} = V_{\vec{p}_{k-1}} \left(1 + A_k^T \frac{1}{\sigma_k^2} A_k V_{\vec{p}_{k-1}} \right)^{-1}, \tag{4.31}$$

$$\Delta\chi^2 = (\Delta y_k)^T \frac{1}{\sigma_k^2} \Delta y_k - (\Delta y_k)^T \frac{1}{\sigma_k^2} A_k V_{\vec{p}_k} A_k^T \frac{1}{\sigma_k^2} \Delta y_k. \tag{4.32}$$

Now only one matrix inversion has to be done. These equations are used to check the $\Delta\chi^2$ of a hit and decide whether to use this hit and calculate the filtered estimate or move on to the next hit. The Kalman filter can be used both for the track fit and for the hit finding.

The residual and the covariance of the residual are determined using the following equations:

$$r_k = \Delta y_k - A_k \left(\vec{p}_k - \vec{p}_{k-1} \right), \tag{4.33}$$

$$\sigma_{r_k}^2 = \sigma_k^2 - A_k V_{\vec{p}_k} A_k^T. \tag{4.34}$$

In the case of a large scatter the fit has more freedom to move the track in the direction of the hit. The residual is then smaller than for the case of a small or no scatter.

The smoothing step

After a filter step a filtered estimate $\vec{p}_k$ and a filtered covariance matrix $V_{\vec{p}_k}$ have been calculated. These should be closer to the real track. If for the previous measurements all the parameters, covariances and residuals are stored their estimates can be improved using the latest knowledge of the trajectory. The following equations have been used to pass back the information to a previous measurement.

$$\vec{p}_{k-1}^{\,\text{smoothed}} = \vec{p}_{k-1}^{\,\text{filtered}} - B_{k-1} \left(\vec{p}_{k-1}^{\,\text{filtered}} - \vec{p}_k \right), \tag{4.35}$$

$$V_{\vec{p}_{k-1}}^{\text{smoothed}} = V_{\vec{p}_{k-1}}^{\text{filtered}} - B_{k-1} \left(V_{\vec{p}_{k-1}}^{\text{filtered}} - V_{\vec{p}_k} \right) B_{k-1}^T, \tag{4.36}$$

$$B_{k-1} = V_{\vec{p}_{k-1}}^{\text{filtered}} V_{\vec{p}_{k-1}}^{-1}. \tag{4.37}$$

The updated residual and the covariance of the residual are:

$$r_{k-1}^{\text{smoothed}} = r_{k-1} - A_{k-1} \left(\vec{p}_{k-1}^{\,\text{smoothed}} - \vec{p}_{k-1}^{\,\text{filtered}} \right), \tag{4.38}$$

$$\sigma_{r_{k-1}^{\text{smoothed}}}^2 = \sigma_{k-1}^2 - A_{k-1} V_{\vec{p}_{k-1}}^{\text{smoothed}} A_{k-1}^T. \tag{4.39}$$

The quantity B_{k-1} is "small" when there is a large scatter. In that case the previous estimate of the trajectory has a larger weight than the current estimate. So the current estimate has only a small influence in the smoothing procedure. In contrast, when no multiple scattering took place the smoothed estimate of the previous state becomes equal to the current estimate.

4.1.3 Multiple scattering

The material inside the detector distorts the track. Particles lose energy and scatter in the presence of material. The material in the ZEUS microvertex detector can be described as a number of thin planes and cylinders. The average material that a particle crosses when going through one ladder is estimated to be 3.0% of a radiation length [41]. The effect of energy loss is neglected. In addition only the change in direction is taken into account, it is assumed that the track is not shifted.

The effect of multiple scattering is mainly a change of the trajectory described by an angle θ with respect to the initial track direction. The distribution of this angle (projected on a plane parallel to the track direction) is approximately Gaussian [12] with mean zero and a width of:

$$\theta_0 = \frac{0.0136}{\beta cp} z\sqrt{x/X_0}\left[1 + 0.038\ln(x/X_0)\right], \tag{4.40}$$

with p, βc and z the momentum, velocity and the charge of the incident particle, and x/X_0 the number of radiation lengths of the scattering medium. From equation 4.40 it is seen that for high momentum tracks the effect of multiple scattering becomes smaller.

How does an uncertainty in the multiple scattering change the track covariance? The following approach is used for a scatter in a thin plane.

- The traversed thickness is calculated from a material database and the incoming angle of the track. The material database is described in section 3.2.2.
- The 1σ scattering angle θ_0 follows from equation 4.40.
- The scattering matrix is calculated by calculating the contribution of the angular uncertainty (θ_0) to the uncertainty in the track.
- Finally this scattering matrix is added to the track covariance.

At the point of intersection the track direction is given by the track parameters φ_t and θ_t. The parameters are changed by an amount:

$$\partial\vec{\alpha} = M\begin{pmatrix} \sin\theta_t\partial\varphi_t \\ \partial\theta_t \end{pmatrix}. \tag{4.41}$$

Here the $\sin\theta_t$ comes from the fact that the ϕ angle is defined in the xy plane. The two columns of (5×2) matrix M are: $M_{i1} = \partial\alpha_i/\sin\theta_t\partial\varphi_t$ and $M_{i2} = \partial\alpha_i/\partial\theta_t$. The scattering matrix can be calculated from:

$$V_{MS} = (\theta_0)^2 MM^T. \tag{4.42}$$

The detailed calculation is done elsewhere [42].

4.2 Track finding

Track finding in ZEUS starts within the CTD. The package that performs this is called VCTRAK [43–45]. In VCTRAK each candidate begins as a seed consisting of hits in three separate super layers of the CTD. To extrapolate the track to the beam line, it is assumed that the track originates from the nominal interaction point. Since this is a rough approximation of the vertex location, a large error is assigned to the preliminary fit. Next, the track is followed inwards and new CTD hits are added. Then using all the hits a CTD track fit is performed.

The VCTRAK package has recently been extended with track finding for the MVD. Now also track candidates are searched in the MVD. To do this segments are searched with 6 or 4 hits in the MVD. The segments are compared with CTD tracks. Candidates that are compatible are used as seeds in the track finding. MVD segments without CTD tracks are left over as MVD stand alone tracks. Tracks through the FMVD are often MVD only tracks. If a CTD track does not correspond with an MVD candidate, the CTD track is stored anyway.

The Kalman filter track fit requires a reasonable estimate for the initial track parameter vector and its covariance. For the tracking studies in this thesis three different strategies have been tested. They are defined as follows:

1. **Kalman track finding** Start with the CTD tracks and then evaluate all MVD hits. Pattern recognition and fitting is done simultaneously.

2. **VCTRAK finding** Start with the results from the CTD/MVD track finding. These include tracks and hits assigned to those tracks. The Kalman filter is only used for fitting.

3. **Combined** The same as the previous but then a second iteration is performed which evaluates the remaining hits.

Although the pattern recognition is different, the actual fit is in all three procedures the same. When the Kalman track finding is used, all reconstructed hits in the MVD are Kalman filtered. In the end only the hits close enough to the trajectory are fitted. For strongly inclined tracks, these are tracks which pass less than three super layers of the CTD, the estimate is rather poor. In busy events the Kalman filter has to evaluate many hits.

Using the results from the VCTRAK finding has the advantage that already most of the hits are associated to tracks. Also the estimates for inclined tracks have improved. However not the full force of the Kalman filter is used, namely the hit finding.

In the third way of fitting, it is possible to refit all tracks including CTD tracks with zero associated MVD hits. This means that all left over hits are tried with all tracks. This takes more time but in this way the best results can be obtained.

After the Kalman filter track fit is initialised with the appropriate starting values the hits in the microvertex detector are fitted. The procedure for one initial track is as follows:

1. Sort all hits along the track, from the most outer hit to the closest hit to the interaction point.

2. Start a loop over all hits. This can be the hits given by the VCTRAK finding or simply all hits in the event.

3. The scattering matrix is calculated up to the silicon sensor of the next hit and added to the current track covariance matrix.

4. The angle between the track and the sensor is calculated and used to calculate the position resolution of the next hit. Figure 3.13b shows the dependence of the position resolution as a function of the angle of incidence. The points are calculated using simulated events and a centre-of-gravity cluster algorithm. There is one exception. For the track fit in the MVD system test described in section 5.2 the angular dependence parameterisation was not available and a fixed uncertainty is used.

5. A check is done on the contribution of the hit to the χ^2 of the track: $\Delta\chi^2 < 10$. If this is not the case then the next hit is evaluated.

6. If there are more hits in the same sensor or the "ghost" of the hit has also a valid $\Delta\chi^2$ then a new track candidate is created for each of those hits. A hit and a ghost cannot be fitted within the same track.

7. Update the trajectory and covariance (filter step). Update the trajectory for the previous measurements (smoothing step). Continue with the next hit.

8. If all hits are fitted and all material is passed then the next track candidate is evaluated further.

9. If all track candidates are evaluated the candidates are sorted on number of hits and χ^2.

10. The track with the most hits and the best χ^2 is considered as the best track and used as the fitted track.

4.3 Vertex reconstruction

By combining the information of multiple tracks, in a vertexing algorithm, a common vertex can be found. To arrive at a reliable secondary vertex reconstruction for heavy flavour tagging, first the interaction or primary vertex needs to be examined. The primary vertex is the estimated position of the ep collision. Subsequently, a secondary vertex can be found from tracks that are not compatible with the primary vertex.

Figure 4.5 shows schematically the parameters in the vertex fit. For each track i the track parameters $\vec{p}_i$ and their covariance $V_{\vec{p}_i}$ are measured. The task of the vertex fit is to estimate the position of the vertex $\vec{x}$ and to estimate the direction and momentum of the tracks at the vertex, expressed as: $\vec{q} = (W, T = \tan\theta_{\text{dip}}, \phi)$. The vector $\vec{q}$ is called the vertex momentum or the vertex re-fitted track.

In the following text, two methods are discussed to determine the vertex. First a general least squares fit is used. Then the vertex fit is done using a Kalman filter algorithm.

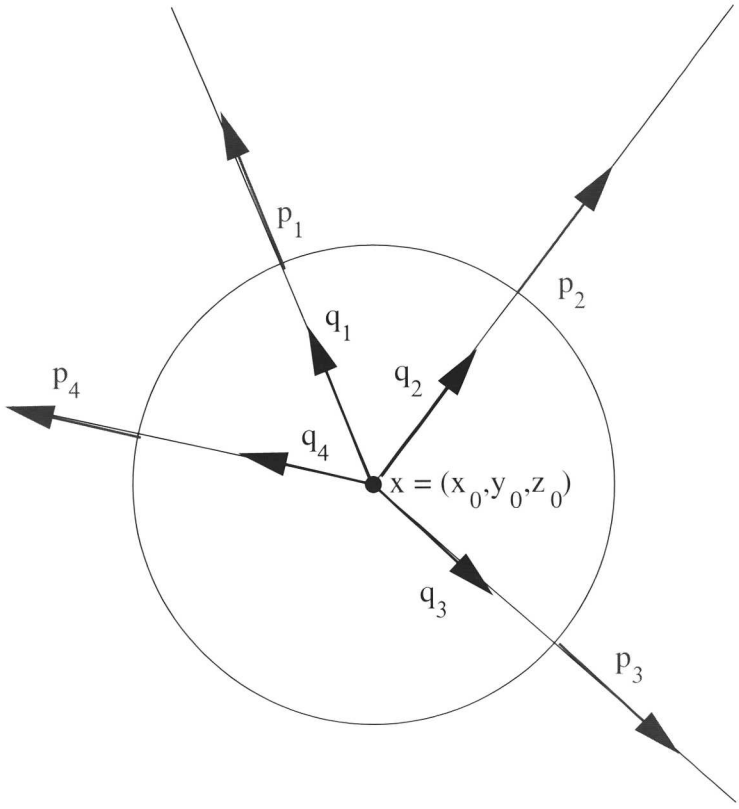

Figure 4.5: Schematic drawing of the vertex problem. The trajectory of a number of tracks ($\vec{p}_i$) are reconstructed with the detector. The vertex fit estimates the vertex position ($\vec{x}$). Also the momentum vector ($\vec{q}_i$) of the tracks at the vertex is fitted.

4.3.1 The full vertex fit

In the full vertex fit all the tracks are fitted to a common vertex simultaneously using the least squares method.

In the track fit the predicted hit positions were described as a vector function of the track parameters and the distance along the track: $\vec{f}(\vec{p}, s)$. For the vertex fit the expected tracks are derived from a vector function $\vec{h}$ which depends on the vertex tracks and the vertex position: $\vec{h}(\vec{x}, \vec{q})$.

- The initial estimate for the vertex parameters is described by the vectors $\vec{x}_0$ and $\vec{q}_0$. In general the track has to be linearised near these initial values:

$$\vec{h}(\vec{x}, \vec{q}) = \vec{h}_0(\vec{x}_0, \vec{q}_0) + A(\vec{x} - \vec{x}_0) + B(\vec{q} - \vec{q}_0), \tag{4.43}$$

  where A and B are derivative matrices:

$$A = \partial\vec{h}/\partial\vec{x}, B = \partial\vec{h}/\partial\vec{q} \text{ with } \vec{x} = \vec{x}_0, \vec{q} = \vec{q}_0. \tag{4.44}$$

  The difference $\vec{h} - \vec{h}_0$ is a vector which describes how the (measured) track parameters change with a change in the vertex parameters.

- A first estimate for $\vec{x}_0$ and $\vec{q}_0$ can be determined by for example the knowledge of a beam spot position and by extrapolating the tracks close to the interaction region. Then by using $\vec{x}_0$ and $\vec{q}_0$ the vector $\vec{h}_0$ can be calculated for all tracks.

- In matrix notation the linearisation for n tracks is described as follows:

$$\vec{h}(\vec{x}, \vec{q}) = \vec{h}_0(\vec{x}_0, \vec{q}_0) + \begin{pmatrix} A_1 & B_1 & 0 & \dots & 0 \\ A_2 & 0 & B_2 & \dots & 0 \\ \vdots & \vdots & \vdots & \ddots & \vdots \\ A_n & 0 & 0 & \dots & B_n \end{pmatrix} \begin{pmatrix} \vec{x}_i - \vec{x}_0 \\ \vec{q}_1 - \vec{q}_0 \\ \vdots \\ \vec{q}_n - \vec{q}_0 \end{pmatrix}, \tag{4.45}$$

  or shorter:

$$\vec{h}(\vec{x}, \vec{q}_i) = \vec{h}_0(\vec{x}_0, \vec{q}_0) + H\Delta\vec{p}_{\text{vertex}}. \tag{4.46}$$

  So H is the full derivative matrix and has a clear block structure. The dimension of H is $5n \times (3n + 3)$.

- The χ^2 is calculated with the following equation:

$$\chi^2 = [\vec{y} - \vec{h}(\vec{x}, \vec{q}_i)]^T V_{\vec{y}}^{-1} [\vec{y} - \vec{h}(\vec{x}, \vec{q}_i)], \tag{4.47}$$

  with

$$\vec{y} = \begin{pmatrix} \vec{p}_1 \\ \vec{p}_2 \\ \vdots \\ \vec{p}_n \end{pmatrix} \quad \text{and} \quad V_{\vec{y}} = \begin{pmatrix} V_{\vec{p}_1} & 0 & \dots & 0 \\ 0 & V_{\vec{p}_2} & \dots & 0 \\ \vdots & \vdots & \ddots & \vdots \\ 0 & 0 & \dots & V_{\vec{p}_n} \end{pmatrix} \tag{4.48}$$

- The new vertex parameters ($\vec{p}_{\text{vertex}}$) and its covariance matrix can be calculated:

$$V_{\text{vertex}} = (H^T V_y^{-1} H)^{-1}, \tag{4.49}$$

$$\vec{p}_{\text{vertex}} = \vec{p}_{0,\text{vertex}} + V_{\text{vertex}} H^T V_y^{-1} (\vec{y} - \vec{h}_0). \tag{4.50}$$

  V_{vertex} is a matrix with dimension $(3n+3) \times (3n+3)$ and $\vec{p}_{\text{vertex}}$ is a vector with $3n+3$ entries.

- With the new parameters the χ^2 is calculated. The procedure is repeated until the χ^2 converges to a minimal value.

In events with high track multiplicity, the least squares algorithm has to work with large matrices which makes it slow. Another disadvantage is that the method is not very flexible for finding outlying/secondary tracks.

When the collision point is well known, for example the beam spot has position $\vec{b} = (b_x, b_y, b_z)$ with covariance $V_{\vec{b}}$, the algorithm stays the same, besides that:

$$\vec{y} = \begin{pmatrix} \vec{b} \\ \vec{p}_1 \\ \vec{p}_2 \\ \vdots \\ \vec{p}_n \end{pmatrix} \quad , \quad V_{\vec{y}} = \begin{pmatrix} V_{\vec{b}} & 0 & \dots & 0 \\ V_{\vec{p}_1} & 0 & \dots & 0 \\ 0 & V_{\vec{p}_2} & \dots & 0 \\ \vdots & \vdots & \ddots & \vdots \\ 0 & 0 & \dots & V_{\vec{p}_n} \end{pmatrix} \tag{4.51}$$

and

$$H = \begin{pmatrix} I & 0 & 0 & \dots & 0 \\ A_1 & B_1 & 0 & \dots & 0 \\ A_2 & 0 & B_2 & \dots & 0 \\ \vdots & \vdots & \vdots & \ddots & \vdots \\ A_n & 0 & 0 & \dots & B_n \end{pmatrix} \tag{4.52}$$

In the unconstrained vertex fit one starts with $5n$ measurements. With the fit $3n+3$ parameters need to be determined. So in total $2n-3$ degrees of freedom are available. In other words at least two tracks are needed to fit a vertex. In the case of a beam constraint, the number of measurements is effectively larger: $5n+3$. The degrees of freedom are: $2n$. (So a vertex fit with zero tracks is possible but gives back the original beam constraint.)

4.3.2 The Kalman filter vertex fit

The full vertex fit as explained in the previous section can become rather complicated if the number of tracks is large. Thanks to the block structure of the derivative matrix (see equation 4.51) the vertex problem can be solved quicker and more flexibly with the help of a Kalman filter.

Basically the Kalman filter vertex fit consists of two steps. First, the current estimate of the vertex position and a track are evaluated. The result depends on the distance between the track and the vertex and the covariance of both. The vertex momentum is

fitted simultaneously, by requiring it originates from the vertex position. Secondly, after n tracks are evaluated and the final position of the vertex is known, all the vertex momenta have to be re-fitted to the new vertex position. In the following text it is shown how this is done mathematically.

Again it is assumed that the vertex problem has n tracks. In contrast to the least squares vertex fit, the vertex is now fitted with one track at a time. The state vector is therefore: $(\vec{x}, \vec{q})$ and has 6 entries. Also a covariance matrix $C_{\vec{x},\vec{q}}$ is defined, representing the uncertainty in the vertex parameters:

$$C_{\vec{x},\vec{q}} = \begin{pmatrix} C & E \\ E & D \end{pmatrix}. \tag{4.53}$$

where C describes the uncertainty in vertex position $\vec{x}$, D described the uncertainty in the vertex momentum $\vec{q}$ and E the cross covariance between the two.

Initially the state vector only consists of the prior information of the vertex position $\vec{x}_0$ and its covariance matrix C_0. The Kalman filter vertex fit describes how to add a new track k with parameters $\vec{p}_k$ to a vertex already fitted with $k-1$ tracks. The weight matrix for track k is $G_k = V_{\vec{p}_k}^{-1}$. The measurement equation, which compares a new state with an old state is nonlinear and the linearisation is given in equation 4.43.

In the prediction step of the Kalman filter the state vector is propagated as follows:

$$\vec{x}_k = \vec{x}_{k-1}, \tag{4.54}$$
$$\vec{q}_k = \vec{q}_{k-1}, \tag{4.55}$$

where $\vec{q}_0$ is the track $\vec{q}$ vector at a "point" close to expected vertex. The vector $\vec{h}_k$ is calculated from $\vec{x}_k$ and $\vec{q}_k$.

The following equations are used in the filter step to get an improved estimate of the state vector and its error matrices.

$$\vec{x}_k = C_k \left[C_{k-1}^{-1} \vec{x}_{k-1} + A_k^T G_k^B (\vec{p}_k - \vec{h}_{k-1}) \right], \tag{4.56}$$
$$\vec{q}_k = S_k B_k^T G_k \left(\vec{p}_k - \vec{h}_{k-1} - A_k \vec{x}_k \right). \tag{4.57}$$

The covariances after the filter step are:

$$C_k = \left(C_{k-1}^{-1} + A_k^T G_k^B A_k \right)^{-1}, \tag{4.58}$$
$$D_k = S_k + E_k^T C_k^{-1} E_k, \tag{4.59}$$
$$E_k = -C_k A_k^T G_k B_k S_k \tag{4.60}$$

with

$$S_k = \left(B_k^T G_k B_k \right)^{-1}. \tag{4.61}$$
$$G_k^B = G_k - G_k B_k S_k B_k^T Gk, \tag{4.62}$$

to keep the notations short. Here it is seen that $\vec{x}_k$ has two contributions: the current vertex position and the contribution of the shifted track parameters. For $\vec{q}_k$ also the contribution of the new vertex position is taken in account.

The increase in χ^2 when adding a track k is expressed as follows:

$$\begin{aligned}\Delta\chi^2_k &= (\vec{x}_k - \vec{x}_{k-1})^T \tilde{C}^{-1}_{k-1}(\vec{x}_k - \vec{x}_{k-1}) + \\ &\quad (\vec{p}_k - \vec{h}(\vec{x}_k, \vec{q}_k))^T G_k(\vec{p}_k - \vec{h}(\vec{x}_k, \vec{q}_k)).\end{aligned} \tag{4.63}$$

Both the vertex and the track contribute to the χ^2. The $\Delta\chi^2_k$ can be used for the decision to use the track in the vertexing algorithm or not. The filter steps can be repeated until a minimum $\Delta\chi^2$ is found. After the minimum is found and the filter step is performed, the algorithm evaluates the next track. In one single filter step the number of degrees of freedom is 2 ($5+3$ "measurements" - 6 parameters to fit).

After all tracks are evaluated the next step is to smooth the momentum vector of all vertex tracks to the estimated vertex position. For the smoothed momenta the following equation is used.

$$\vec{q}_k = S_k B^T_k G_k(\vec{p}_k - \vec{h}_{k-1} - A_k \vec{x}_n) \tag{4.64}$$

The smoothed covariances for D_k and E_k can be found elsewhere [46].

The vertexing algorithm is implemented in the reconstruction program in two different modes:

Constrained The nominal interaction point or beam spot is used as the initial estimate for the vertex. All tracks are evaluated and are fitted to this vertex in consequetive Kalman filter steps.

Unconstrained An algorithm is used that first finds the vertex of all track pairs. The vertex with the best χ^2 is re-evaluated with all the other tracks. Tracks which have a χ^2 below 25 are added to this current vertex. For the remaining tracks the procedure is repeated.

4.4 Summary

In this chapter a detailed explanation was given on the track reconstruction in the microvertex detector. Also the reconstruction of the primary and secondary vertices was discussed. In chapter 5 the track reconstruction is used to check the performance of the microvertex detector. Furthermore the physics studies in chapter 6 rely on the vertex reconstruction from this chapter.

Chapter 5

Cosmic rays in the MVD

In this chapter the tracking performance of the ZEUS microvertex detector is discussed. Cosmic ray data are used to study the performance (sections 5.2 and 5.3). From these data, results are derived about the data quality, alignment and efficiency of the detector. A study of the improvement on the track reconstruction when MVD alignment corrections are applied is found in section 5.4. Furthermore in section 5.5 the results of a single track MC study are discussed and compared to the data. Also in that section the impact parameter and momentum resolution are investigated.

5.1 Introduction

During the construction of the microvertex detector (MVD) four testing periods can be identified:

1. The test program for the silicon sensors and read out electronics in a test beam experiment at DESY [47].
2. The quality control of all components after each assembly step.
3. Cosmic ray tests outside ZEUS. This is the pre-installation system test.
4. The (ongoing) cosmic ray tests inside the experiment.

Here the focus is on the cosmic ray tests done with the MVD. The cosmic muons are easy to trigger on and give (most of the time) clear and isolated hits in the detector.

In this chapter two cosmic ray tests are discussed. The first one is called the MVD system test and is discussed in section 5.2. The second one is the regular ZEUS cosmic data test. The analysis of these data is discussed in section 5.3.

5.2 Cosmic ray test before installation

In March 2001 the final assembly of the MVD took place in the Jade Hall at DESY. This included the insertion of the beam pipe and the mounting of the lower and upper MVD

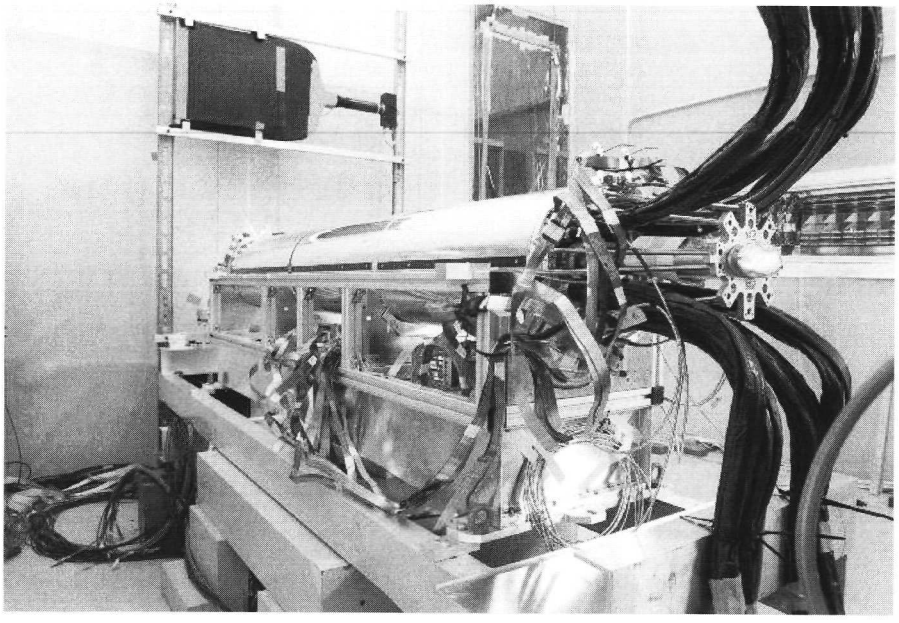

Figure 5.1: Photograph of (a part of) the setup for the MVD system test in the Jade Hall at DESY. The MVD is still supported by its transport frame. The picture shows the rear side of the MVD with the cables that lead to the patch box several meters away.

half on each other. Besides this all the final read out and supply cables and electronics were installed. A photograph is shown in figure 5.1.

5.2.1 Trigger

The experimental setup was completed with a scintillator trigger, consisting of various scintillator blocks connected to photomultiplier tubes. Figure 5.2 shows schematically the location of the scintillator blocks.

In a four week running period 2.5 million cosmic events were stored on tape. After the detector performance was studied and optimised a sample of 355k remained, requiring the same stable conditions. The number of events was sufficient to test the Kalman filter track fit with enough tracks. Approximately one third of the events has a valid track with 6 or more hits. In some events more than one track was found.

Coincidences between different layers of scintillator were used as an external trigger to start a read out cycle of the MVD [48]. The read out of the MVD is designed for the fixed HERA bunch crossing rate of 10.4 MHz. In the case of the system test the events arrive randomly distributed in time. Effectively this means that the signal is sampled around its maximum value.

The time difference between the coincidence signal and the next MVD clock pulse was measured with a TDC. Figure 5.3 shows the result of a cosmic run with a large time window. The TDC time range is divided in bins of 5 ns.

The sum of the pulse heights of the strips in a cluster (cluster sum in ADC counts) is plotted versus the TDC time in figure 5.3. Then in figure 5.4 it is shown that the cluster sum distribution (for three different time bins) can be fitted with a Landau curve. In figure 5.5 the most probable value for each bin is plotted. This shows the time dependence of the gain. The final trigger window was set at a width of 30 ns to have sufficient event rate.

5.2.2 Track fit

During the tests outside the ZEUS experiment no external magnetic field was available. To describe a track generated by a traversing muon the model introduced in section 4.1.1 is used without the need to fit a curvature. So only the following four parameters are fitted: $T = \tan\theta_{\mathrm{dip}}$, ϕ_0, D_0, Z_0. Because there is no momentum estimation of the trajectory no scattering matrix could be derived. The Kalman filter track fit for the MVD system test is similar to that explained in section 4.1.2 but without the addition of the scattering matrix.

To start the fit procedure a track seed is required. Combinations of hits in an inner and outer half of one module are made, forming so called "crosses". Each straight line from one cross to another cross is used as a seed for the Kalman filter.

For a good cosmic event at least three of these crossed hits are required. Since every pair gives a seed for a track fit, several candidates emerge. For every candidate all the measured hits in the MVD are evaluated with the fit algorithm. After all candidates are

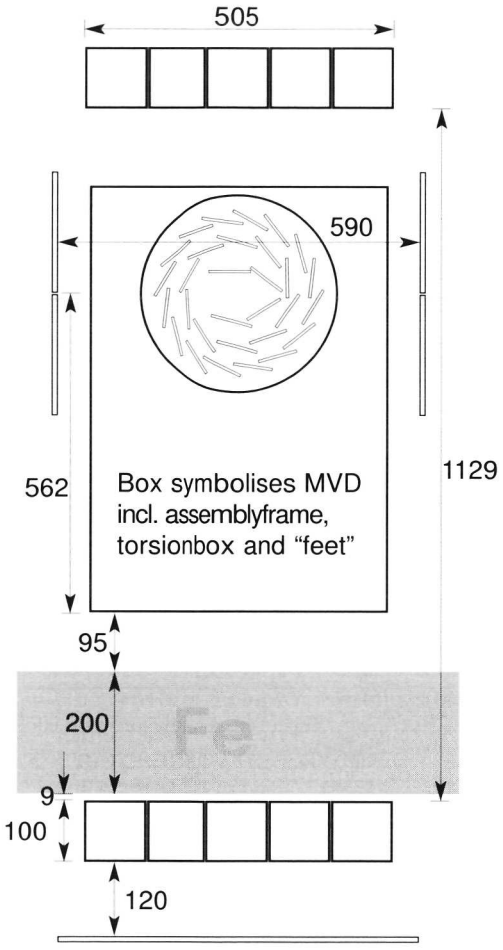

Figure 5.2: Schematic view of the geometry of the scintillator blocks used to trigger cosmic rays for the MVD system test. The displayed lengths are in mm. An iron block filters out very low momentum cosmic muons.

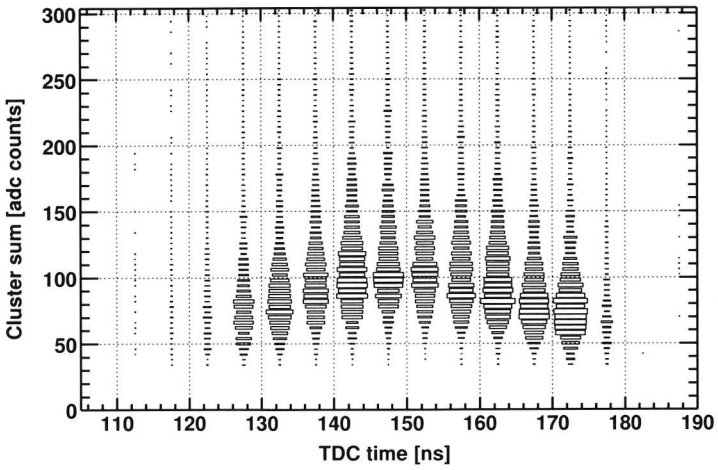

Figure 5.3: Results of the data that are obtained without constraining the time difference between the MVD readout clock and the arrival time of the cosmic (TDC time). The plot shows the total sum of the measured cluster in bins of 5 ns. The size of the rectangles is proportional to the number of events in a bin.

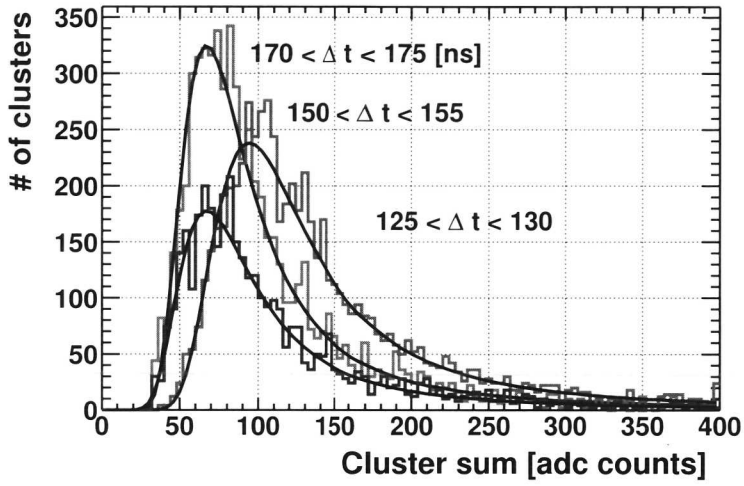

Figure 5.4: For three different time bins a Landau fit of the data is done. The position of the maximum of the Landau distribution gives the most probable value for the energy loss (MPV).

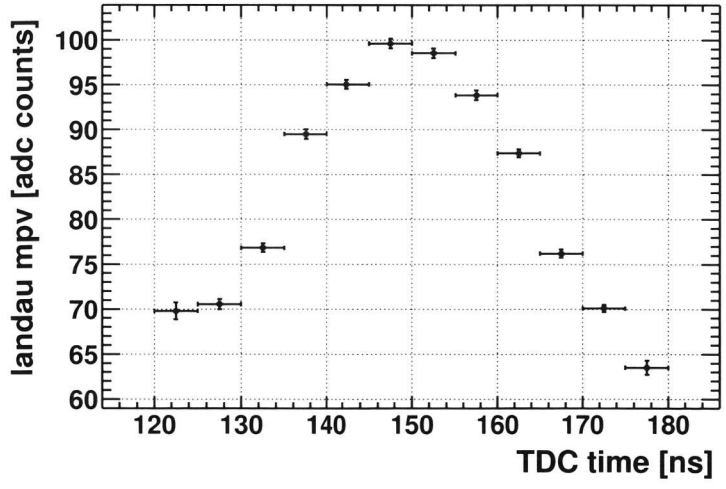

Figure 5.5: Plot of the most probable value versus the TDC time.

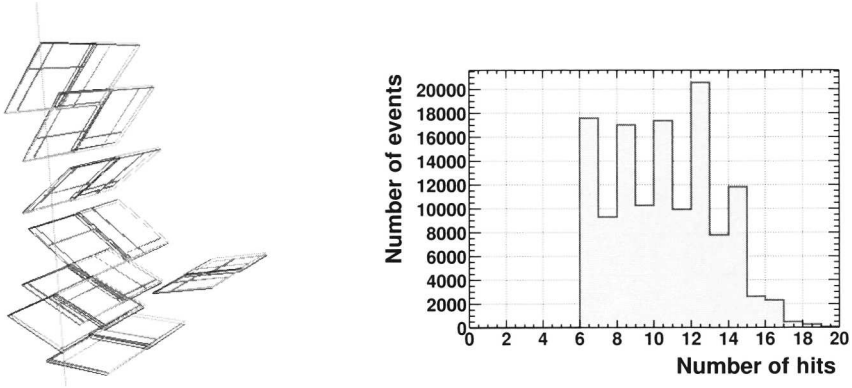

(a) (b)

Figure 5.6: (a) A beautifully measured cosmic track with 7 crossed hits (= 14 hits) in the microvertex detector. This display was specially developed to debug the MVD tracking. In (b) the distribution of the number of assigned hits per track is shown. At least six hits were required to fit a track.

fitted, the final fitted track is the track with the most hits or the best total χ^2. The track fit for the MVD system test is explained in detail elsewhere [31].

In figure 5.6a an event is shown in a 3-dimensional display. Not less than 7 crosses are fitted to this straight track. Also the position of the ghost hits are shown. A histogram of the number of hits per track is shown in figure 5.6b. The distribution peaks at even numbers of hits due to the double layer structure. Because at least three crosses are required, there are no tracks with less than six hits.

The fitted track parameters are shown in figure 5.7. Most tracks have $|T| < 1$ (or $|\theta_{\text{dip}}| < 45°$ because $T = \tan\theta_{\text{dip}}$) and $60° < |\phi_0| < 120°$.

5.2.3 Residuals, alignment and efficiency

For the best track candidate the residuals are already calculated during the fitting procedure. The residuals are the difference between the measured hit position and the estimated track position in the sensor as follows from equation 4.34.

The expected position uncertainty has the following contributions:

- The intrinsic resolution of the sensor which is of the order of 10 µm for tracks perpendicular to the sensor. The centre of gravity clustering algorithm was used (see section 3.1.4). The increasing error for tracks with a large angle of incidence was not taken into account.

- Uncertainties in the position of the sensors inside the MVD which deviate from their design positions. The average shifts are of the order of 50 µm. This number is estimated from the detailed and precise survey after assembly (see section 3.2.1).

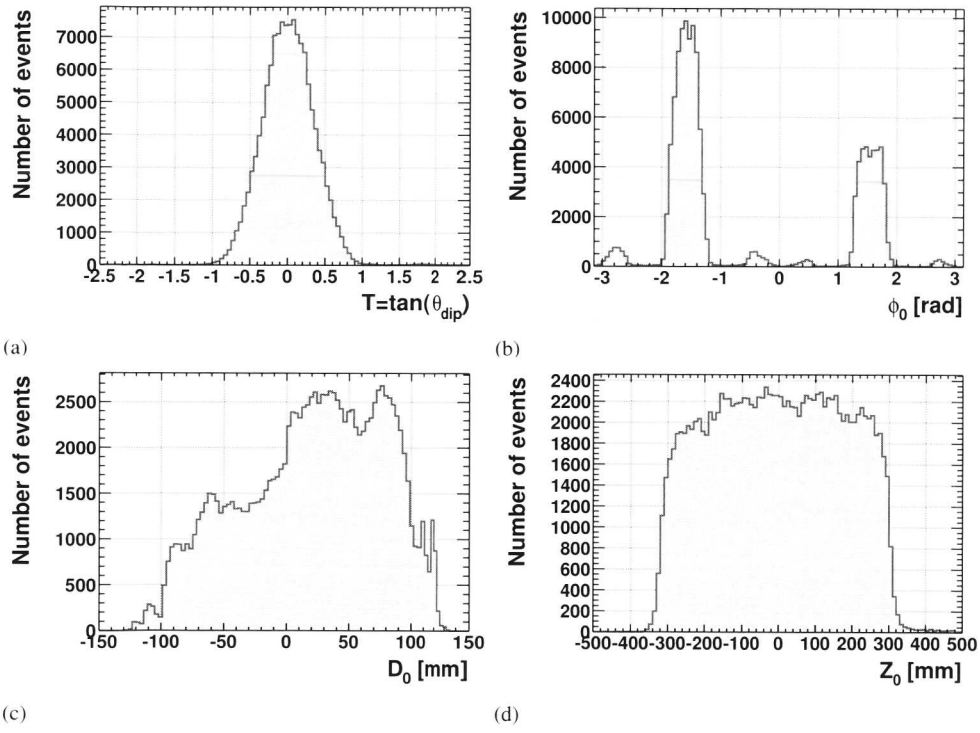

Figure 5.7: Distribution of the fitted cosmic tracks. Each track has at least 6 hits in the microvertex detector. The following parameters are plotted: $T = \tan\theta_{\mathrm{dip}}$ (a), ϕ_0 (b), D_0 (c) and Z_0 (d).

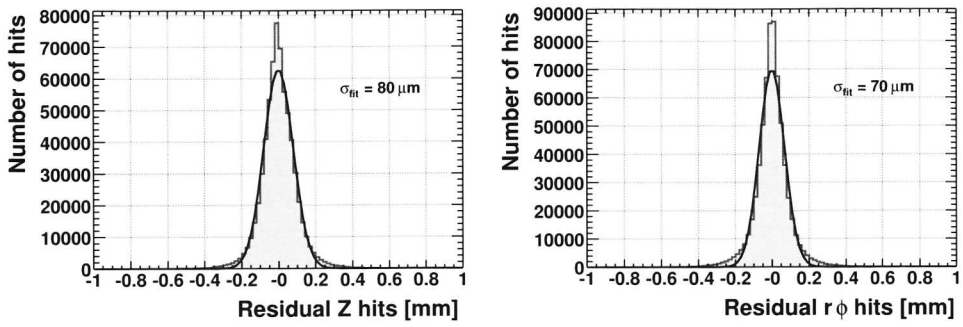

(a) (b)

Figure 5.8: Residuals of the track fit for the z hits (a) and the $r\phi$ hits (b) in the MVD barrel. For the position reconstruction of the cluster a centre of gravity algorithm is used and no alignment corrections are done.

	sensor positions from	
	design geometry	survey geometry
$\sigma(z$ hits [μm])	80	56
$\sigma(r\phi$ hits [μm])	70	70
σ(wheel 0 hits [μm])	750	510
σ(wheel 1–3 hits [μm])	580	550
mean wheel 0 hits [μm]	-270	-50
mean wheel 1–3 hits [μm]	-100	-34

Table 5.1: The σ and the mean of the residuals of the trajectory for z hits, $r\phi$ hits and wheel hits. Both the design geometry and the survey geometry of the sensor positions are used for the track fit. For the survey geometry only shifts in the z direction are applied.

- Scattering of the muons in the material of the MVD. A 1 GeV muon, travelling through material with a radiation length of 1%, gets an average deflection of about 1 mrad. Over a distance of 50 mm this leads to an average error in the position estimation of 50 μm.

The estimated position error which is used in the track fit is 50 μm, which slightly underestimates the real error. The maximum $\Delta\chi^2$ of one hit is set to high values (40) so the effect on the hit finding is small.

Figure 5.8 gives the residuals of all z and $r\phi$ hits in the barrel for single track events. The Gaussian fit of the data has a mean smaller than 1 μm and a standard deviation of 80 μm for the z hits and 70 μm for the $r\phi$ hits. These measurements are done without using any detector alignment correction. The position of a cluster is determined by calculating the centre of gravity of the cluster.

In the forward MVD most of the collected cosmics passed both the wheels and the ladders. Both in the wheels and the ladder the sensors are crossed with rather large

angles. So the position reconstruction is worse. Also small uncertainties in the alignment (in z) of the MVD wheels have a large effect on the difference between the measurement and the track. By setting the error on the cluster position of the wheels to 1 mm the wheel hits were included in the fit. The residuals for the wheels are given in table 5.1. Due to low statistics, the results are shown for the wheel closest to the BMVD (wheel 0) and the three most forward wheels (wheel 1-3).

During the construction of the MVD the positions of the various mechanical components were measured. From this survey a shift in the z direction is calculated for every ladder and wheel. With these offsets the design positions of the sensors are changed. A single run of 41k events shows then already a large improvement for the residuals of the barrel and wheel hits. In table 5.1 the residuals are given again for the z hits, $r\phi$ hits and wheel hits. There is no improvement in the $r\phi$ hits because the corrections are done in the z direction. The residuals for the z hits were 80 µm and are now 56 µm. For the wheel hits the position resolution also improved.

Efficiency

A simple algorithm was used to estimate the efficiency of all the sensors of the barrel MVD. For each track all sensors are evaluated, that are expected to be crossed by the track. If in a sensor no hit (looking only to the hits used to fit the track) is found it counts as inefficient. By dividing the number of hits by the total number of expected intersections for a sensor a measure of efficiency is determined. The results are shown in figure 5.9. The expected intersection is calculated with the total area of the sensor and this is larger than the estimated active area of the sensor. The result is a maximum geometric efficiency of 92.7%. Without this geometric effect the average efficiency of fitting a hit in a sensor is 97.7%. In this calculation sensors with problems in the readout are not used. From 600 sensors in the barrel 14 sensors were excluded from the read out due to electronic problems. Six sensors had different electronic problems and could only measure charged particles in a part of the active area.

5.3 Cosmic rays inside ZEUS

In the previous section cosmics ray data are studied which are recorded during the MVD system test. After installation of the vertex detector inside the existing ZEUS experiment, another type of cosmics muons is triggered. A recorded event is shown in figure 5.10. Hits in the CAL, CTD and MVD can be seen. In ZEUS the magnetic field curves the muon trajectory, so also the momentum of the muon can be estimated.

In this section the ZEUS cosmic trigger is discussed. The cosmic ray events are very clean and are thus useful for MVD alignment and impact parameter studies.

5.3.1 Trigger and timing

The cosmics that are useful for MVD studies are isolated muons travelling close to the interaction region of the ZEUS detector. These muons are triggered with the BCAL and

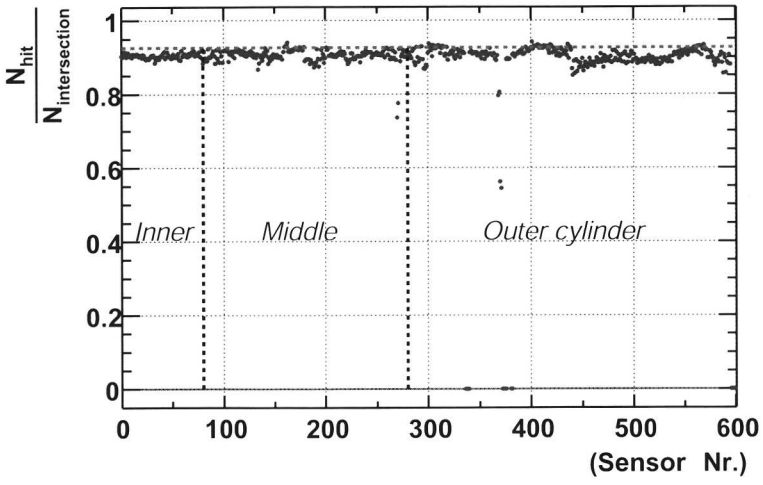

Figure 5.9: The efficiency for all barrel sensors. In the calculation the track can intersect with the total area of a sensor, while the outer edges of the sensor do not belong to the active area. This results in a maximum (geometric) efficiency of 92.7%. From 600 sensors 14 are switched off from the read out chain.

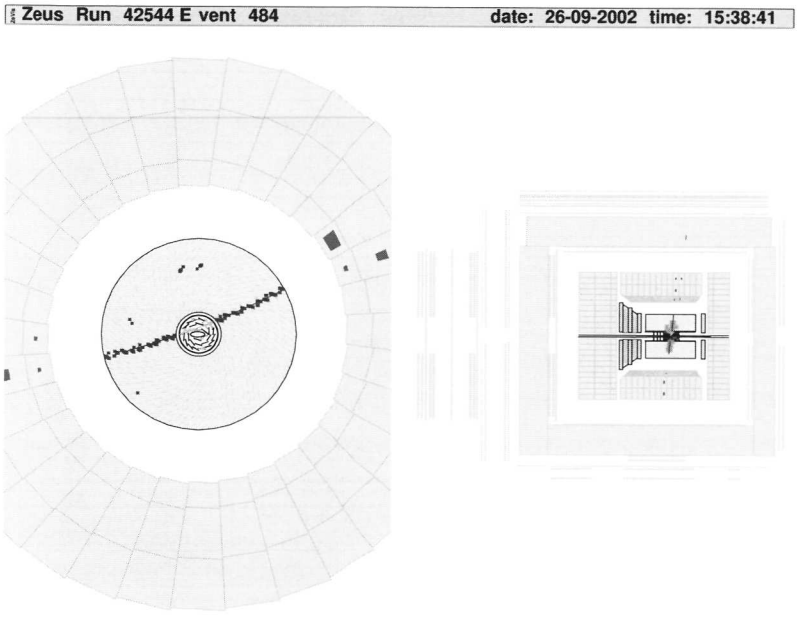

Figure 5.10: A cosmic muon detected in the ZEUS detector. The muon gives hits in the CAL, CTD and MVD. The trajectory is curved, due to the magnetic field.

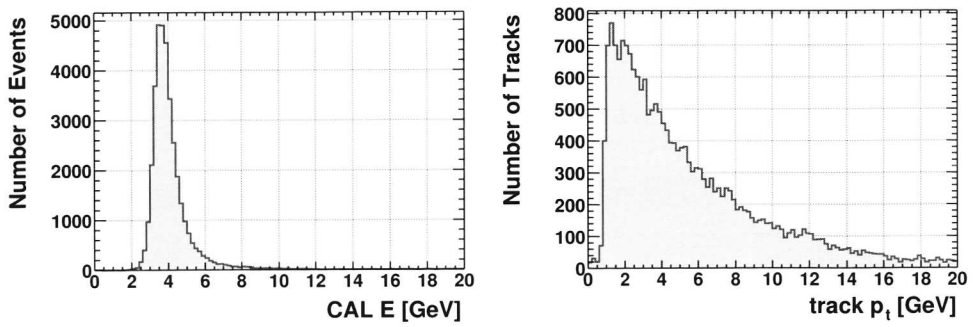

(a) (b)

Figure 5.11: (a) Energy measured in the calorimeter for isolated cosmic muons. (b) Transverse momentum (p_t) distribution of the isolated cosmic tracks.

CTD. This trigger configuration is called the "BCAL cosmic and good track trigger". In this text such an event is called an "isolated cosmic". The following requirements are used in the first level trigger to select isolated cosmics:

- Coincidence between upper and lower barrel calorimeter sides.
- Total energy more than 700 MeV in the barrel calorimeter.
- A CTD good track coming from the interaction region.

In figure 5.11a the CAL energy spectrum is plotted for the isolated cosmic trigger. The distribution peaks at 3.5 GeV. A minimum ionising muon travelling straight through the calorimeter loses on average 2.6 GeV. The measured value is larger, mainly because the response of the calorimeter is calibrated for particle shower measurements and not for minimum ionising particles [49].

Figure 5.11b shows the transverse momentum distribution of the muon tracks. The CTD reconstruction software (VCTRAK) reconstructs the cosmic event as a di-track physics event. The tracks are selected by requiring two tracks in the CTD with opposite charge. An additional requirement was that both tracks have similar track parameters. This distribution shows that most of the triggered muons have a p_t of approximately 2 GeV. For higher p_t the distribution decreases exponentially.

The arrival time of the cosmic can be measured with the calorimeter timing. This time is the global calorimeter time which is the average time of all the calorimeter cells above threshold. Since there is no beam the timing is with respect to a 10.4 MHz clock.

Using the CAL global time an MVD time scan can be done in a similar manner as described in section 5.2.1. The results are plotted for a 2002 cosmic run in figure 5.12a. Within the shaded region the CTD track finding performs well. The optimum of the MVD signal is just outside this window, still most performance studies are done with this (2002) sample. From 2003 onward the MVD and CTD are synchronised as can be seen in figure 5.12b.

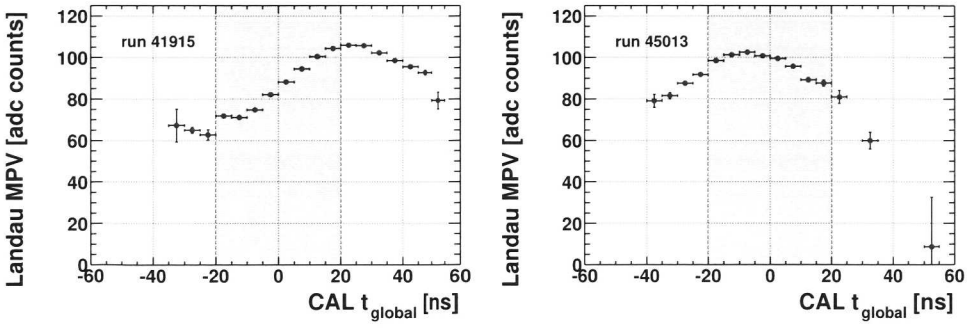

(a) (b)

Figure 5.12: In (a) the most probable value (MPV) of the cluster sum is plotted in bins of 5 ns. The peak in the signal does not correspond with the region for efficient CTD track finding (from -20 to 20 ns). This is for ZEUS run 41915. In December 2002 the MVD timing was adjusted. Plot (b) shows that the peak in the MVD signal does correspond with the region of the good CTD tracks.

5.3.2 Track fit

The track fit is again based on the procedure described in section 4.1.2. But this time the CTD tracks and their covariance matrices serve as the starting estimate of the filter. The strategy is to update the track stepwise with hits close to the extrapolation of the trajectory. Furthermore two additional changes are made: First, a better description of the angular dependence of the position resolution is included. The parameterisation from section 3.1.4 is used to describe the angular dependence. An uncertainty of 40 μm is added in quadrature because the design geometry is assumed. (For the system test data 50 μm was used for all contributions.) Secondly, the multiple scattering effects in the material of the detector are now included in the fit procedure.

Starting from the cosmic trigger data the following track selection was applied:

- Two tracks in the CTD with opposite charge (one cosmic muon travelling through the CTD is reconstructed in ZEUS as two independent tracks).
- The D_0 and Z_0 of the tracks are within 10 cm of each other.
- The Kalman track finding finds at least two hits in the MVD for both tracks.

The number of events is around 100k after these selection criteria are applied to the cosmic data of 2002.

Figure 5.13a shows the number of hits per track. The distribution peaks at even numbers of hits. The peak structure is less clear than was observed during the MVD system test. This is caused by the bad timing of the detector and also some half modules were masked by the data acquisition.

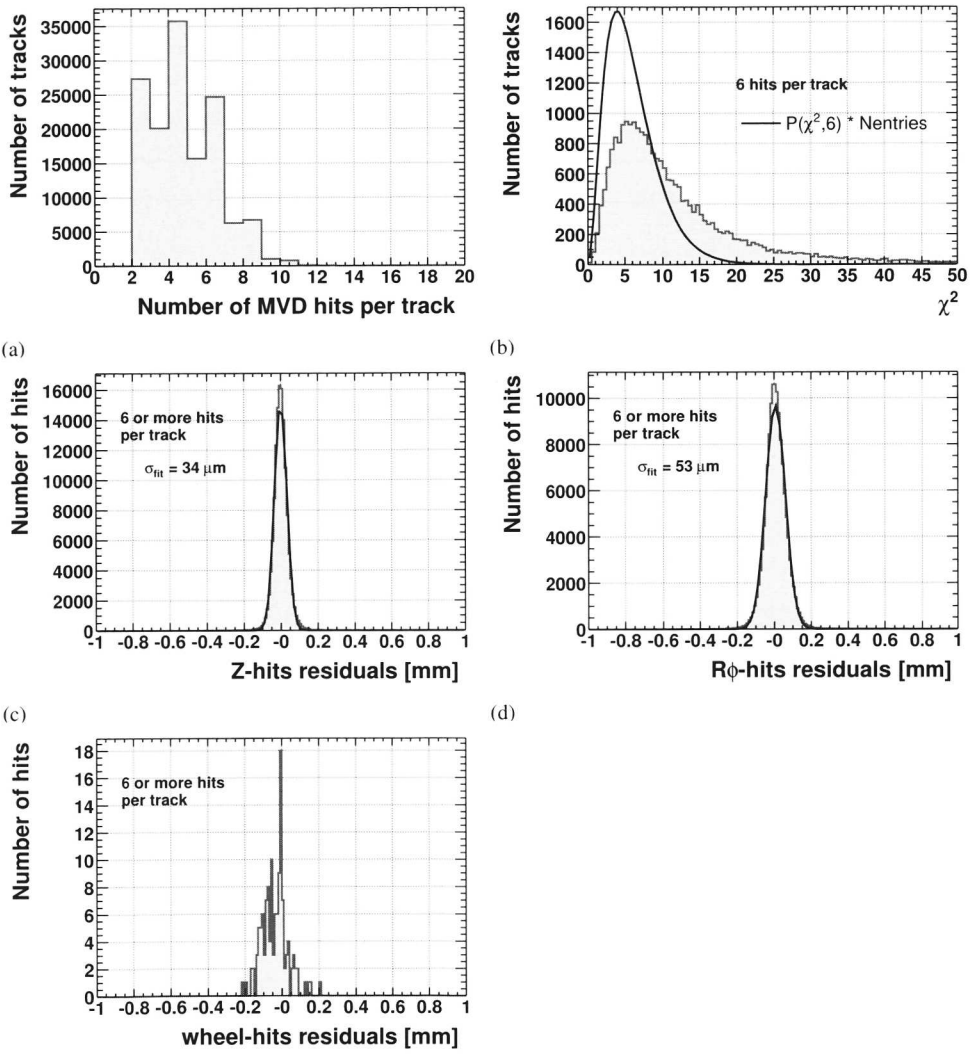

Figure 5.13: Number of hits per track (a), the χ^2 for tracks with 6 hits (b), the residuals of the z hits and the $r\phi$ hits for cosmics with at least 6 hits per track (c and d). In (e) the residuals are plotted for the (less frequent) wheel hits. Note that one cosmic is regarded as two separate tracks.

	mean [μm]	σ [μm]
z hits	1	34
$r\phi$ hits	7	53
wheel hits	-40	63

Table 5.2: Results obtained from the MVD hit residual distribution for cosmic ray muons.

In figure 5.13b the χ^2 for the tracks is plotted. The plot shows that there is a large tail present. This suggests that for these data (and the design geometry) the estimated position error is too small.

The residuals plotted in figures 5.13c and d for tracks with at least 6 hits are narrower than the system test data. Since the ZEUS magnetic field and the used trigger filter out the lower momentum cosmics, the muons are scattering less than in the system test. For the wheel hits the residuals seem to be worse, however the statistics is low. The results are summarised in table 5.2.

In figure 5.14 the distribution of the track parameters (θ, ϕ_0, D_0 and Z_0) are plotted. Most tracks with 6 hits pass the MVD in a cone of 30° with respect to the ZEUS y axis and are within a distance of 10 cm of the nominal z axis. The peak structure in Z_0 is caused by the 1 mm gaps between two MVD modules on a ladder. Also track efficiency is lost when the extrapolation of the CTD track is far off and crosses the wrong sensor.

5.4 Alignment

In the previous section a sample of approximately 100k good cosmic events was discussed. These cosmics go through the CTD and the MVD. This same sample is now used to study the alignment of the microvertex detector. Furthermore the improved geometry knowledge from a track alignment study is used. Finally an estimate is made for the impact parameter resolution as function of the track transverse momentum.

The MVD and CTD z position can be compared by looking at the difference in the Z_0 parameter between tracks fitted with the CTD only and the same tracks fitted with the MVD. After a few Kalman filter steps the track parameters are dominated by the MVD measurements. If a misalignment between MVD and CTD exists, the tracks are shifted towards the MVD frame since its precision is much better. This effect is seen in the left column of figure 5.15. A clear shift between MVD and CTD of 0.8 mm is seen.

To study the impact parameter precision of the MVD it is useful to consider the cosmic track as two independently reconstructed tracks and see how well they match. In the right column of figure 5.15 the mismatch between the two track segments is plotted. Only tracks fitted with at least 6 MVD hits are used. A Gaussian fit of the distribution has a width of 180 μm. An estimate for the impact parameter resolution of these cosmic tracks is then $180/\sqrt{2} = 127$ μm. This depends also on the momentum of the tracks. The momentum of most of the cosmics is between 1 GeV and 2 GeV. Comparing figure 5.15a with figure 5.15b shows that the MVD gives an impact parameter that is more than ten times better than the CTD only.

The aim of the alignment is to estimate the real positions and orientation of all the

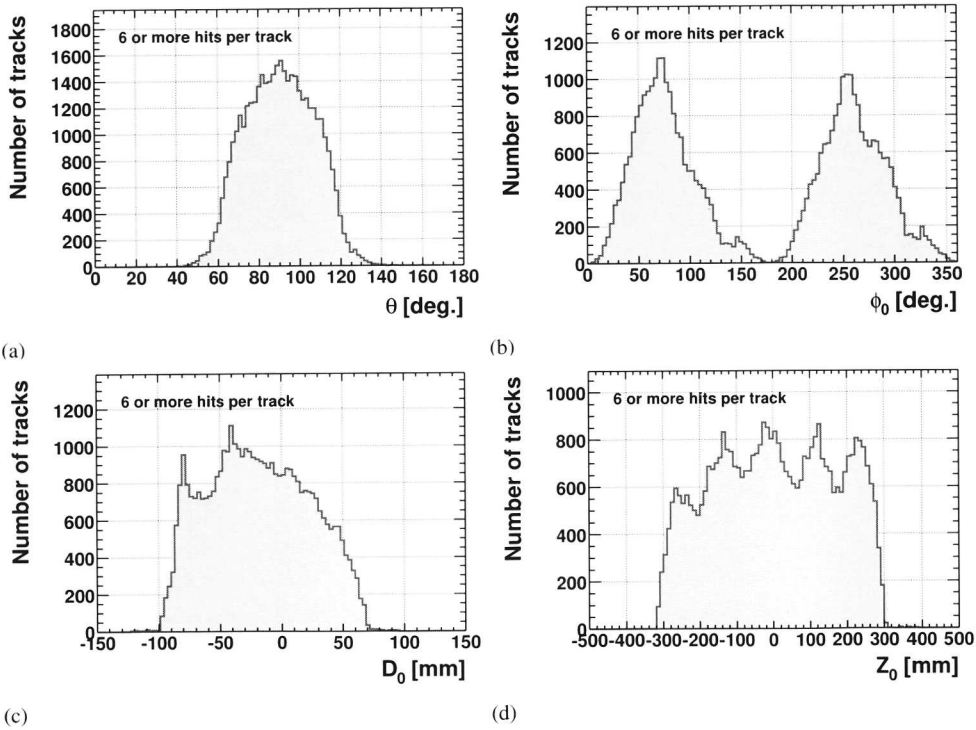

Figure 5.14: The parameters of the selected cosmic ray tracks. Shown are θ (a), ϕ_0 (b), D_0 (c) and Z_0 (d).

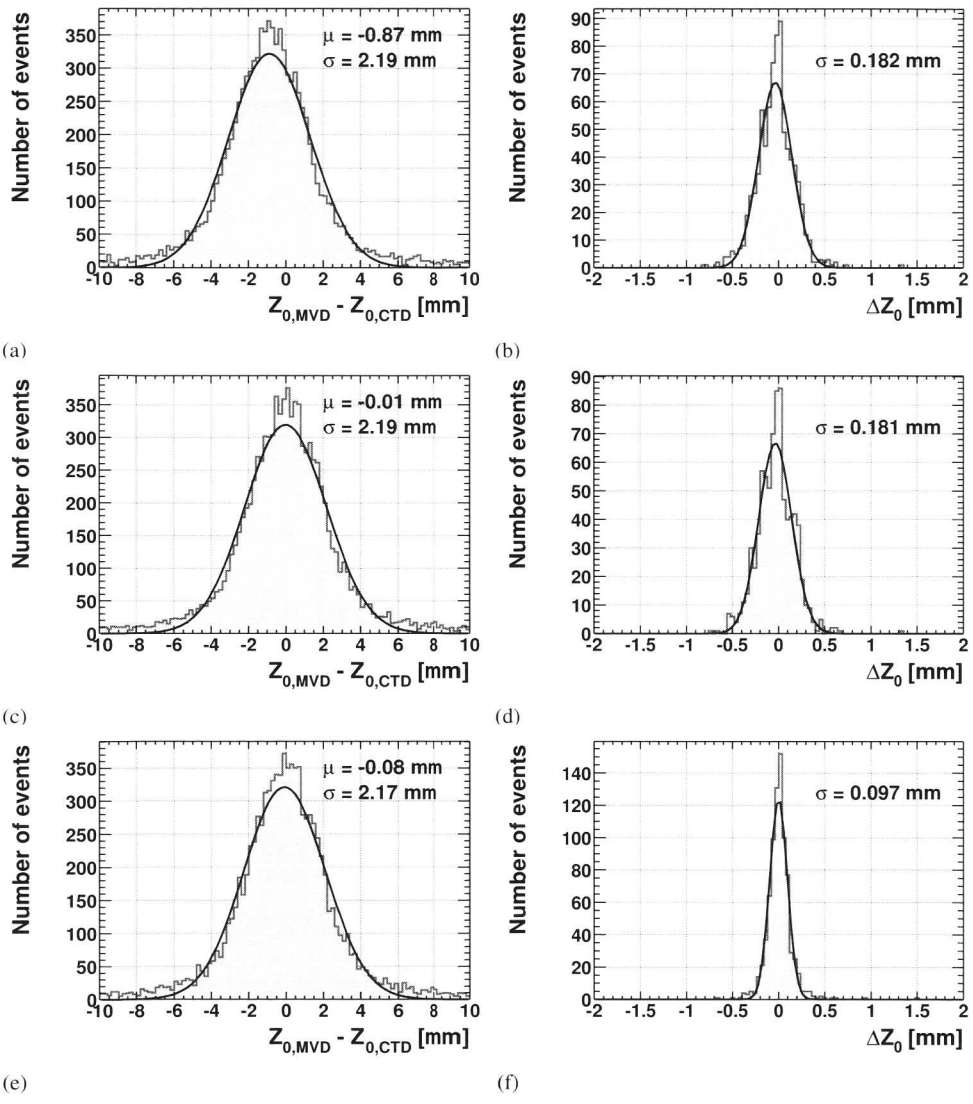

Figure 5.15: In the left column the Z_0 parameter of the track fit with CTD only and MVD is compared. In this case the CTD resolution limits the width of the distribution. The right column compares the "two independent" tracks of a cosmic both fitted with the MVD. In (a) and (b) the design geometry is used. In (c) and (d) the MVD is aligned with respect to the CTD. In (e) and (f) also the MVD ladders are aligned.

MVD sensors. When these estimated positions are applied, the track fit is expected to improve.

Input for the alignment are the differences between the expected track position and the measured hit positions. Then a least squares minimisation is done to determine the geometry offsets.

With the 2002 cosmic data a preliminary tracking alignment is calculated for the MVD [50]. First a global alignment was performed: The position and orientation of the MVD with respect to the CTD was calculated. Subsequently, the MVD internal alignment was done. The data sample was only large enough to do the internal alignment per ladder. However it is known from section 3.2 that already a big effort was made to construct the MVD as precisely as possible.

Using these alignment offsets the reconstruction of the cosmic events can be redone. To study the improvement, the cosmic sample is reconstructed with three different geometries:

1. design geometry (from the technical drawings)

2. MVD with respect to the CTD

3. MVD with respect to the CTD and the MVD barrel ladders.

The results from this study are shown in figure 5.15, where the mismatch in Z_0 is plotted between the CTD fitted track and CTD and MVD fitted track. A clear improvement is seen when comparing the design and aligned geometries.

When the MVD ladders are aligned it is seen in the figure that the width of the mismatch between the upper and lower track becomes much smaller. The Gaussian fit gives for all tracks in the sample a width of 97 µm.

The transverse momentum dependence of the mismatch in Z_0 is shown in figure 5.16. The mismatch becomes smaller at high p_t. In this region the fit is dominated by the position reconstruction. For lower momentum, multiple scattering becomes more and more important so the mismatch increases. To get from this an estimate of the impact parameter resolution the data are divided by $\sqrt{2}$. The result for the impact parameter fit is: $83/p_t + 47\,\mu m$. This satisfies the design criterium, requiring an impact parameter resolution of 100 µm.

The alignment program did not use the incident angle to optimise the cluster reconstruction. It used the centre of gravity algorithm and assigned to each hit an uncertainty of 50 µm. The residual of a hit i with respect to the expected position was calculated by re-fitting the track without hit i. The optimised residuals were 47 µm for the z hits and 64 µm for the $r\phi$ hits. The precision reaches a level where the cluster reconstruction method and error estimation becomes more important. By implementing these improved algorithms the detector alignment improves and indirectly the impact parameter resolution.

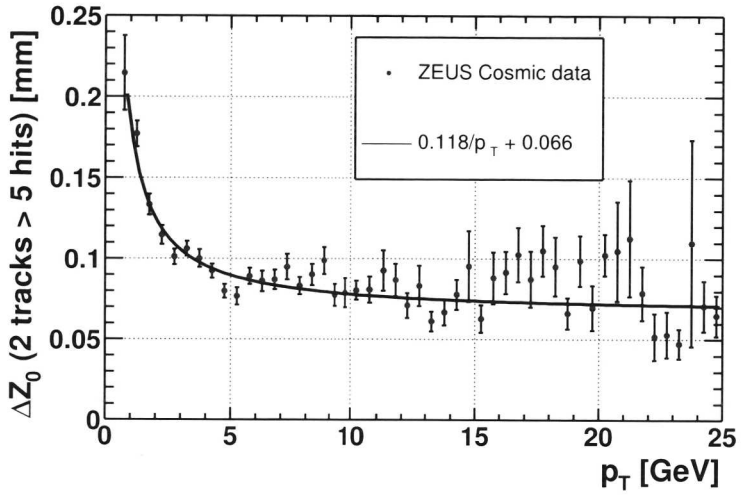

Figure 5.16: The mismatch between the upper and lower MVD track in bins of transverse momentum. Used tracks have at least 6 hits in the MVD. In the used geometry the MVD ladders are aligned.

5.5 Monte Carlo comparison

In this section the performance of the track fit is studied using tracks and hits from a Monte Carlo simulation. The advantage is that the information of the generator is available. So the reconstructed tracks and hits can be compared with the generated tracks and hits.

5.5.1 Single track Monte Carlo events

The ZEUS Monte Carlo is based on a full GEANT[24] simulation of the detector including the microvertex detector.

A single track MC is used to investigate the hit and track finding efficiency of the track reconstruction. A sample of 10k muons was generated in the following kinematic range: $0.2 < p < 10.0\,\text{GeV}$, $0^\circ < \phi_{\text{track}} < 360^\circ$ and $5^\circ < \theta_{\text{track}} < 175^\circ$. The vertex position was set to the expected nominal e^+p interaction point: $(x, y, z) = (17.5, 0, 0)\,\text{mm}$. Both negatively and positively charged muons were generated.

5.5.2 Hit assignment

For a good track fit the hits have to be assigned to the correct track. Ghost hits, noise hits and hits belonging to other tracks (wrong hits) have to be disentangled reliably. In the Monte Carlo every hit can be traced back to a certain track or to noise.

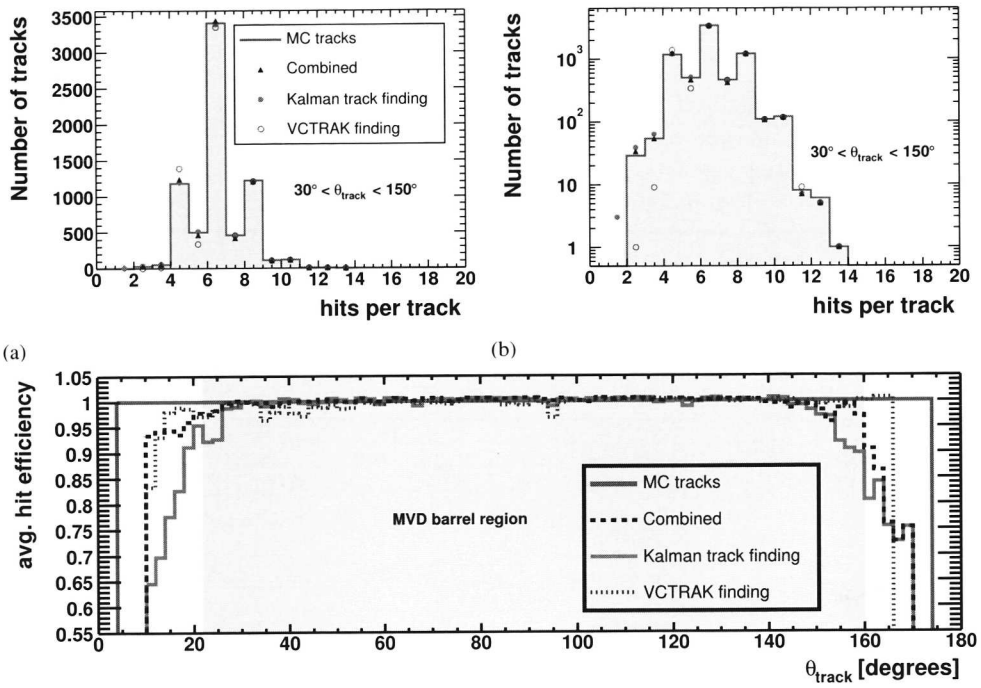

Figure 5.17: Hit finding in the MVD with different tracking strategies using MC tracks. The strategies are explained in section 4.2. In (a) and (b) the number of assigned hits per track is shown. In (c) the average hit finding efficiency per track in bins of θ_{track} is presented.

After the simulation has generated the charge on the MVD strips, noise is simulated. This is done by adding to every read out strip a random pulse height according to a Gaussian distribution with mean zero and average noise (σ). The same clustering algorithm is applied as for data.

The probability to pick up noise hits is very small (the signal-to-noise ratio was larger than 20 in the simulation). Furthermore because a single track Monte Carlo is used it is impossible to pick up a hit from a wrong track. The current Monte Carlo sample is primarily used to check if the true hits are assigned to the track.

Figure 5.17 gives an overview of the hit finding for the different strategies. The three strategies were Kalman track finding, VCTRAK finding, combined track finding (see section 4.2).

In figures 5.17a and 5.17b for all tracks the number assigned hits per track is plotted. The distribution peaks at four, six and eight hits which is also expected from the detector geometry. The distribution closely follows the number of hits per Monte Carlo track. For

tracks with a small number of hits the VCTRAK finding finds less tracks.

The number of ghost hits and missing hits per track are also studied for tracks in the region $30^\circ < \theta < 150^\circ$. Most tracks do not fit to ghost hits or do not miss hits. The Kalman track finding picks up a ghost hit for 0.1% of the tracks. For the VCTRAK finding and combined method this is about 0.05%. For about 0.1% of the tracks the Kalman track finding has more than 1 missing hits. About 3% (2%) of the VCTRAK finding tracks (combined or Kalman finding tracks) are missing 1 or 2 hits.

Ghost hits can be picked up if the prediction of the CTD track is substantially offset with respect to the first MVD hit. The Kalman track finding is more sensitive to this. In some cases when the track crosses the module overlap the ghost hit fits better to the trajectory than the "true" hit.

Hits are missed if the track does not cross a sensor, or the contribution to the χ^2 of the track is too large. Also when the first hit is not a true hit, then the track can deviate too far to find other true hits, resulting in a large number of missing hits. This happens in some cases for the Kalman track finding.

Figure 5.17c shows the hit finding efficiency in bins of θ_{track}. The hit finding efficiency is defined as the number of hits assigned to the track divided by the number of "true" hits of the track. For tracks in the range $30^\circ < \theta_{\text{track}} < 150^\circ$ the efficiency is better than 99%. For tracks with lower or higher θ_{track} not only less tracks are found (see next section), also less hits per track are found.

5.5.3 Track finding

In figure 5.18 the track finding efficiency is plotted in bins of angle θ and ϕ_0 and momentum p of the generated track. The results of the three tracking strategies are compared with MC tracks having at least one hit in the MVD. The efficiency is defined as the number of reconstructed tracks divided by the number of true (MC) tracks per bin. An additional constraint is that only reconstructed tracks are counted with at least two "true" hits.

In the central region ($30^\circ < \theta < 150^\circ$) almost all tracks are found, except when the VCTRAK finding is used. The performance is worse because the minimum number of MVD hits required is four hits. (For example an $r\phi$ and a z hit in two MVD modules.) Tracks with less than four hits do occur in the MVD, especially in the range of ($150^\circ < \phi < 210^\circ$). The decrease in the track finding efficiency is best seen in the ϕ_0 plot. Tracks with only a small number of hits are found with the Kalman track finding and with the combined method.

In the forward ($\theta < 30^\circ$) and in the rear ($\theta > 150^\circ$) region the track finding efficiency worsens. The reduced efficiency can be explained as follows. First, when a track crosses fewer super layers in the CTD the measurement of the CTD track is fitted with fewer hits. In particular the Z_0 and T track parameters are less accurate. In this case the measured CTD track can be far off from the corresponding MVD hits. This decreases the track finding in the MVD for all three methods. Secondly, tracks which only pass one or two cylinders of the MVD, have only few hits available (looking only to the MVD barrel). This also makes the track finding in the MVD with the VCTRAK package more difficult.

For tracks which pass the MVD forward wheels additional hits can be measured. The

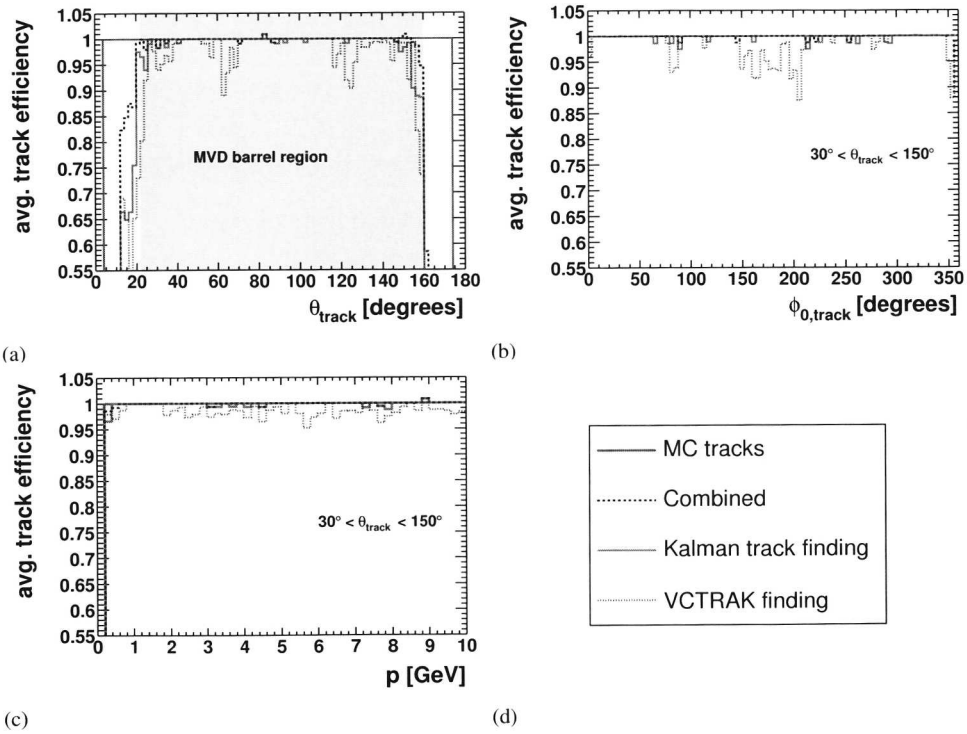

Figure 5.18: Track finding efficiencies for tracks which are fitted with at least two MVD hits. The results are presented in bins of the angles θ (a), ϕ_0 (b) and momentum p (c). The three different fitting strategies are explained section 4.2. For comparison the "true" tracks with at least one MVD hit are also shown.

method	found tracks	efficiency
All MC tracks	7102	100.00%
VCTRAK finding	6992	98.45%
Kalman track finding	7088	99.80%
Combined	7096	99.92%

Table 5.3: Comparison of the number of found tracks for different fitting strategies for tracks with $30^\circ < \theta < 150^\circ$. The results are obtained from a generated sample of 10k single muons.

VCTRAK finding finds track candidates in the forward direction. For this study only forward tracks were stored which are compatible with a CTD track. Future studies will include stand alone forward MVD tracks. However separating real tracks from background tracks in this region is difficult.

When no track is found in the MVD by the VCTRAK finding, the combined method re-fits the track with the CTD track as a seed. Some additional MVD hits are then found in the forward region.

The efficiency of track finding in the central region is summarised in table 5.3. For single track events the efficiency is larger than 99%. The VCTRAK finding has less efficiency because it needs at least four MVD hits in a track.

5.5.4 Quality of the track fit

For the study of the quality of the tracks a closer look at the actual fit is taken. Important parameters are the hit residuals Δ_i and the χ^2 of the track. In addition the pull-distributions are used, defined as follows:

$$p_i = \frac{\Delta_i}{\sigma_i}, \tag{5.1}$$

where σ_i is the hit resolution. If all sources of uncertainty are described correctly, these distributions should be Gaussian with mean zero and a width of 1.

If all errors are Gaussian then the expectation value of the χ^2 of a least squares fit is:

$$\langle \chi^2 \rangle = \left\langle \sum_{i=1}^{N_{\text{hits}}} \left(\frac{\Delta_i}{\sigma_i} \right)^2 \right\rangle = N_{\text{df}}, \tag{5.2}$$

where N_{df} is the number of degrees of freedom and N_{hits} is the number of hits ($N_{\text{df}} = N_{\text{hits}} - N_{\text{par}}$ and N_{par} is the number of parameters).

The χ^2 from the Kalman track fit is the sum of the $\Delta\chi^2$ of the filter steps (see section 4.1.2). For every assigned hit one degree of freedom is obtained. In the discussion of some of the results a simplified interpretation is used that considers a regular least squares fit with N_{hits} and N_{par}.

The residuals are also calculated from the Kalman filter. The expected hit errors follow from a parameterisation using the angle of incidence (see section 3.1.4).

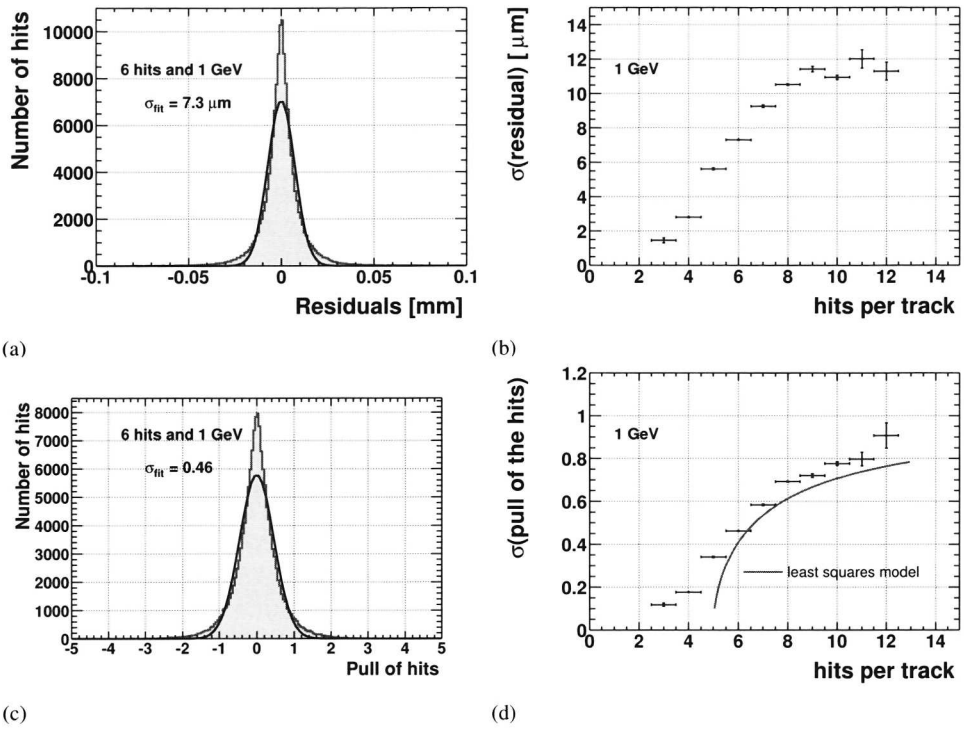

Figure 5.19: In (a) is shown the distribution of the hit residuals for 1 GeV tracks. A Gaussian fit is used to determine the width of the distribution. In (b) the width of the residual distributions are shown versus the number of hits per track. In (c) is shown the distribution of the hit pulls. In (d) is plotted the width of the pull distributions versus the number of hits in the track. The line is the least squares expectation and is explained in the text.

The hit residuals are not identical to the hit resolution. Because the hit is included in the fit, the residual tends to be smaller than the hit position resolution. Assuming that all errors are Gaussian then by rewriting equation 5.2 the following approximation for the hit residual is derived:

$$\sigma_{\text{res}} \approx \sqrt{\frac{N_{\text{df}}}{N_{\text{hits}}}}\sigma_{\text{hit}} \qquad N_{\text{df}} \geq 0, \tag{5.3}$$

so only for large number of hits is $\sigma_{\text{res}} \approx \sigma_{\text{hit}}$.

In figure 5.19 the distribution of the residuals and pulls are shown for 1 GeV tracks. For this study the z and $r\phi$ hits are not distinguished.

Substituting 5.3 in 5.1 then the pull equals $\sqrt{N_{\text{df}}/N_{\text{hits}}}$. The least squares model to describe the pulls is only valid starting from 5 hits. In figure 5.19d this simple model is seen to closely follow the data points. For tracks with 6 hits the pull is then 0.41. The value measured in figure 5.19c is 0.46.

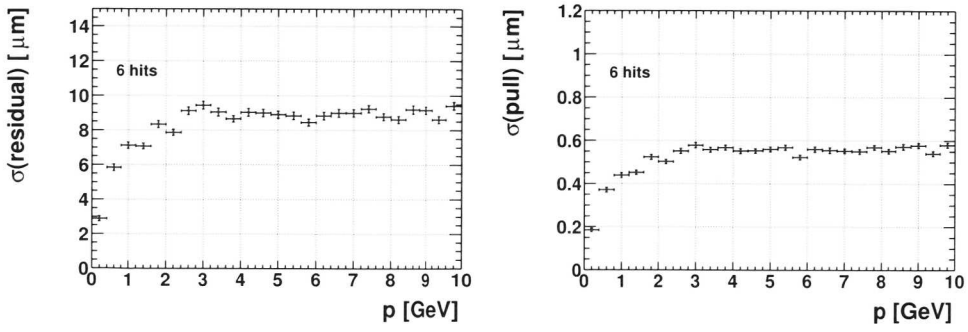

(a) (b)

Figure 5.20: Residuals (a) and pulls (b) of the hits as function of the momentum of the track. The decrease in the residuals and pulls for tracks with low momentum is due to multiple scattering.

For tracks with 6 hits σ_{res} is 7.3 μm. With the use of equation 5.3 an average hit position resolution of 17.9 μm is obtained. Considering that the resolution decreases due to the angular dependence and multiple scattering this is a consistent result.

In figure 5.20a and b the width of the residual and the width of the pull distribution is plotted for different track momenta. The residuals for low momenta become smaller. This is because multiple scattering has an increasing effect at low momentum. In the track fit procedure the covariance of the track is made larger when multiple scattering is expected. Consequently the fit pulls the track closer to the hit.

The pull for high momentum tracks is 0.55. Now effectively 4 parameters are fitted instead of 5. (The curvature becomes more or less zero). A track with 6 hits and 4 parameters corresponds to a pull of: $\sqrt{2/6} \approx 0.57$.

Applying equation 5.3 again for the high momentum tracks in figure 5.20a an average hit resolution is obtained of 15.6 μm. This is again consistent with the expected errors.

Figure 5.21 shows histograms of the χ^2 and χ^2-probability for tracks with 6 hits and 1 GeV and tracks with 6 hits and 6 GeV. In figures 5.21a and c the line is the χ^2-distribution for 6 degrees of freedom. The average χ^2 is not too far off from 6, but the distributions are not described by the line.

The 1 GeV tracks have a larger tail than the 6 GeV tracks. This happens if the scattering is underestimated or if the expected hit errors are too small. For the 6 GeV tracks some tracks are fitted too well. It is possible that the initial track covariance is too large. A further step in tuning the hit errors, track covariances and multiple scattering effects is recommendable.

Another quantity to investigate are the track pulls after the fit. For example for the Z_0 parameter one can calculate $(Z_{0,\text{rec}} - Z_{0,\text{true}})/\sigma(Z_0)$, where $\sigma(Z_0)$ comes from the appropriate diagonal entry of the covariance matrix.

In table 5.4 the track pulls of all five track parameters are given for tracks of 1 GeV and 6 GeV. The widths of the pull distributions for 6 GeV tracks are smaller than for 1 GeV

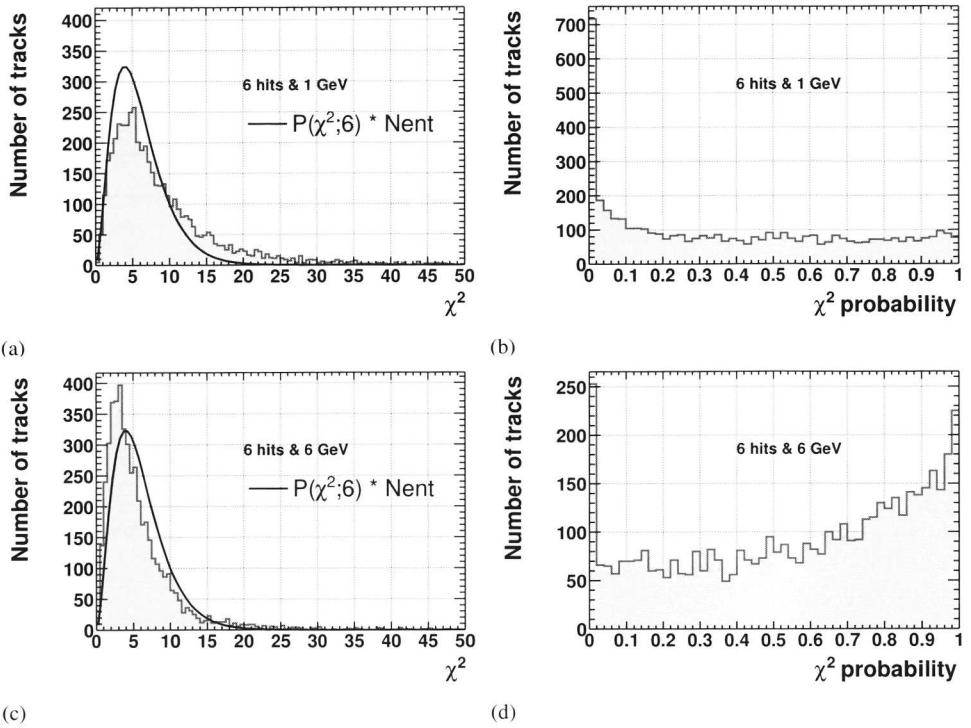

Figure 5.21: The χ^2 distribution and probability for 1 GeV tracks (a and b) and for 6 GeV tracks (c and d). All tracks have 6 hits.

	1 GeV		6 GeV	
	pull mean	pull sigma	pull mean	pull sigma
$W\,[\mathrm{mm}^{-1}]$	0.011	1.25	0.005	1.12
T	-0.014	2.19	-0.043	1.58
$\phi_0\,[\mathrm{mrad}]$	0.019	2.12	-0.040	1.59
$D_0\,[\mathrm{mm}]$	0.023	1.74	-0.030	1.30
$Z_0\,[\mathrm{mm}]$	0.009	1.77	0.033	1.31

Table 5.4: Mean and width of the track pull distributions for 1 GeV and 6 GeV tracks.

tracks. One effect still to be corrected for is that in the reconstruction no correction was applied for the scatters in the most inner sensors and the beam pipe.

5.5.5 The track impact parameters

The impact parameter is determined by calculating the point of closest approach of the reconstructed track to the coordinate where the track is generated. The radial and z component of this vector are studied as function of p_t, θ and ϕ_0.

The vector from the origin to the point of closest approach is perpendicular to the track. Hence, the determination of the impact point is most sensitive in the directions perpendicular to the track.

In figure 5.22a the impact parameter resolution is shown in bins of transverse momentum. The selected tracks are in the following range: $30^\circ < \theta_{\text{track}} < 150^\circ$, passing through the MVD barrel. For tracks with momenta larger than 1 GeV an impact parameter resolution of 50 µm is approached. The effect that multiple scattering increases the error on the impact parameter for lower track momenta is also clearly seen.

Also in figure 5.22a the z impact parameter resolution is fitted. The fit gives the parameterisation: $0.056/p_t + 0.018$ mm. This is a better resolution than was experimentally derived with cosmic ray data in section 5.4 ($0.083/p_t + 0.047$ mm). However, it should be noted that the detector geometry in the Monte Carlo is perfect.

To see the effect of extrapolation on the uncertainty of the impact parameter, tracks are studied with momenta between 3 and 10 GeV. In figure 5.22b the radial impact parameter is plotted in bins of θ_{track}. For inclined tracks the radial impact parameter becomes worse. In the figure it is seen that the resolution in z stays constant. To obtain the z impact parameter the (three dimensional) impact parameter vector is projected on the z axis. For inclined tracks the extrapolation is larger, but the projection of the impact parameter vector on z becomes smaller and compensates.

In figure 5.23 the impact parameter is plotted in bins of $\phi_{0,\text{track}}$. Tracks with $140^\circ < \phi_{0,\text{track}} < 210^\circ$ are measured with only the two outer cylinders of the MVD. In this region the impact parameter resolution gets significantly worse.

5.5.6 Tracks through the MVD wheels

The performance of the fit in the forward region is studied with a special track sample. The tracks were generated between 1 and 5 GeV and $5^\circ < \theta_{\text{track}} < 30^\circ$. In figure 5.24 the residuals of the track fit are shown for the barrel sensors and the wheel sensors for tracks with at least 6 hits. The tracks traversing the barrel sensors and the wheel 0 sensors produce wide clusters, because of the angular dependence on the cluster shape. This leads to worse resolution. There is also an asymmetry in the distributions. Probably as consequence of a different geometry definition for the wheels between the reconstruction and the simulation. A more detailed analysis is needed.

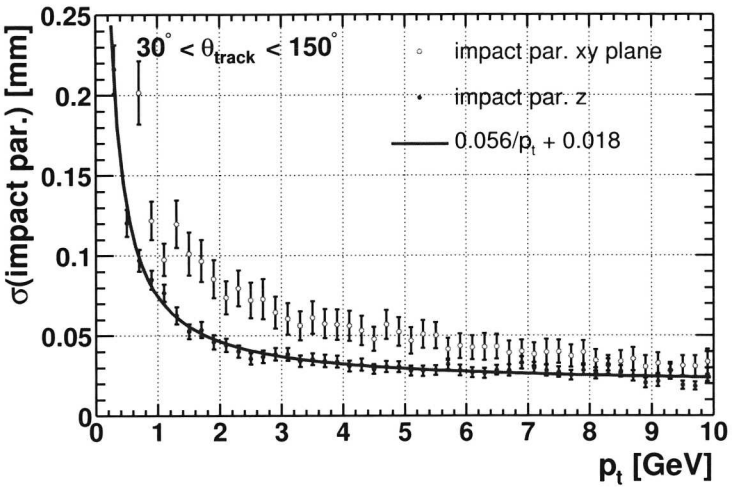

(a)

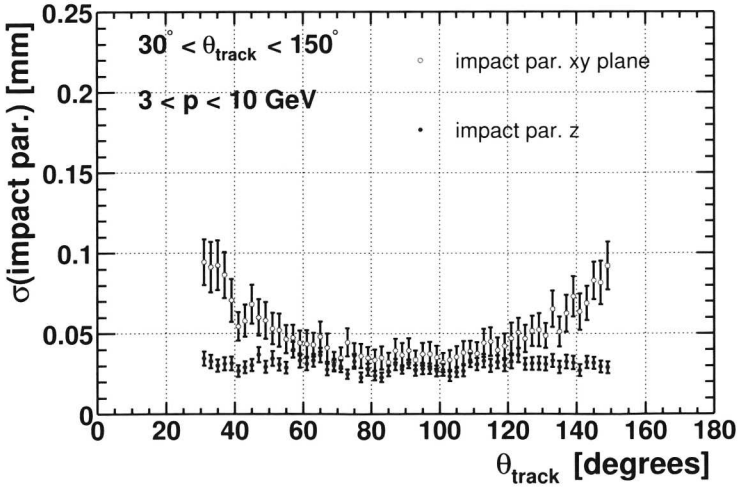

(b)

Figure 5.22: Impact parameters projected on the xy plane and on the z axis in bins of transverse momentum (a) and θ_{track} (b).

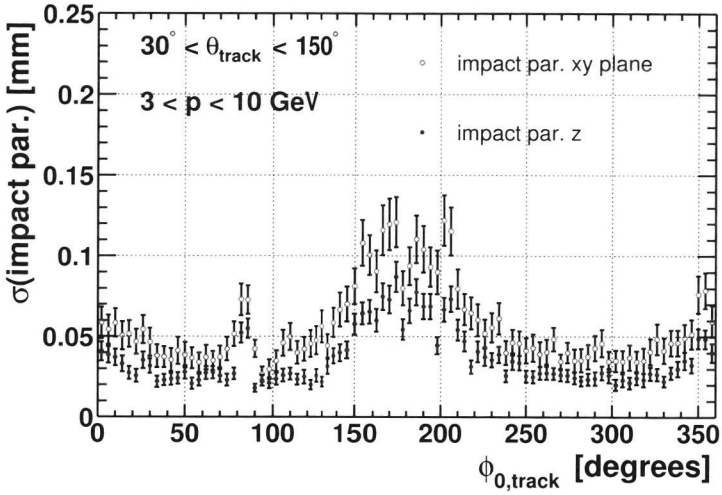

(a)

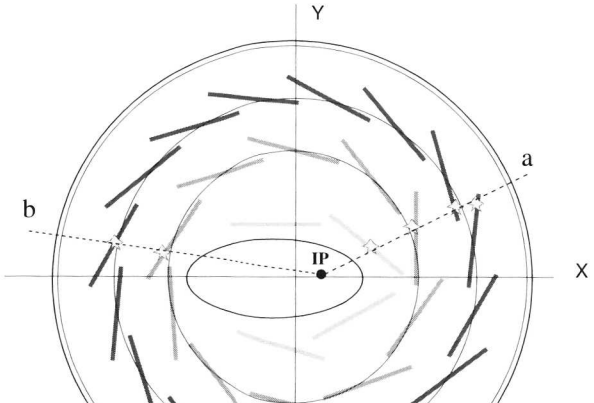

(b)

Figure 5.23: Impact parameters projected on the xy plane and on the z axis in bins of ϕ_0 (a). In (b) the hits of track a are closer to the origin of the track. The shorter extrapolation gives a better resolution in the xy plane and in z.

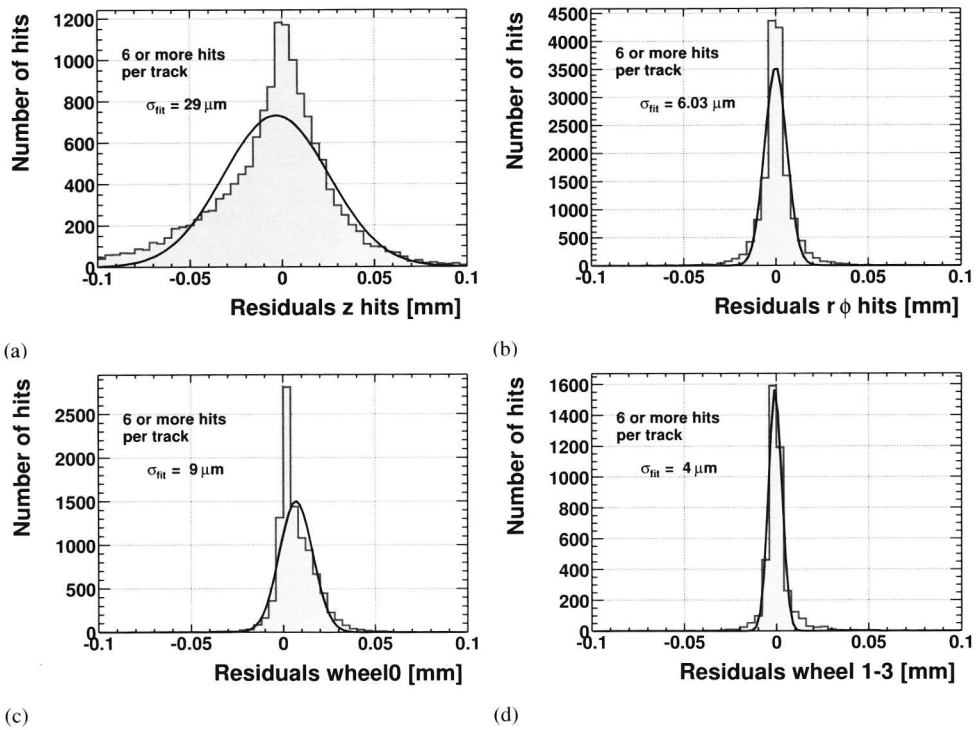

Figure 5.24: Residuals of hits from tracks with at least 6 hits going through the wheels.

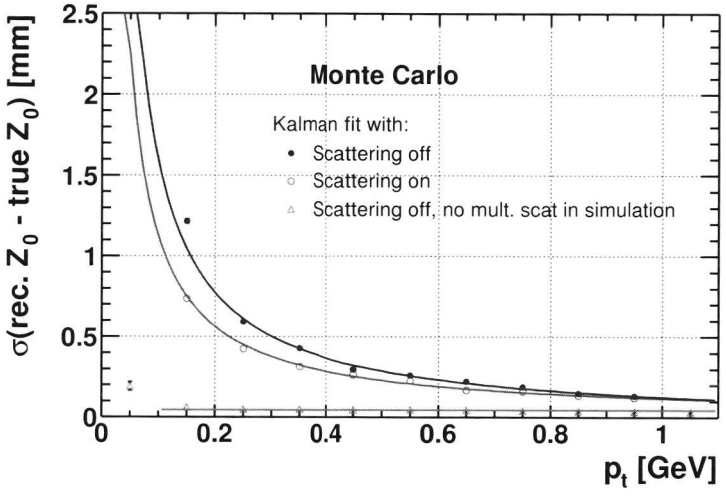

Figure 5.25: For low momentum tracks the difference in Z_0 $\sigma(Z_0(\text{rec}) - Z_0(\text{true}))$ is plotted as function of the transverse momentum.

5.5.7 Effect of the multiple scattering corrections

For low momentum tracks charged particles scatter in the material of the detector. This distorts the trajectory of the particle. The effect of multiple scattering is that the precision of the track reconstruction decreases. The Kalman fit includes the additional uncertainty due to multiple scattering to the track covariance matrix.

To see the effect of this method the "mismatch" of Z_0 between the true (generated) track and the reconstructed track is investigated. The studied sample consisted of 10000 muon tracks with momentum $0.125 < p < 1.25\,\text{GeV}$, $30° < \theta < 150°$ and $0° < \phi < 360°$.

The results are shown in figure 5.25. The quantity $\sigma(Z_0(\text{rec}) - Z_0(\text{true}))$ is defined as the width of a Gaussian fit of the tracks in transverse momentum bins of 0.1 GeV. Two different track fit modes are used. One takes the effects of multiple scattering taken into account and the other does not. It is seen that for lower momentum the mismatch is smaller when the scattering is included. This is the effect of the Kalman filter giving less weight to the tracks if multiple scattering is included.

A different look at the effects of multiple scattering is obtained by switching the multiple scattering off in the simulation, as if there is no material. The mismatch between the reconstructed and the generated track is very small (45 µm) and does not depend so strongly on the transverse momentum. For tracks below 0.1 GeV the starting track of the CTD can become unreliable, because there are only hits in a few CTD layers.

Overall it can be concluded that the Kalman filter and the correct treatment of uncertainties coming from multiple scattering has improved the tracking precision significantly for these low momentum tracks.

5.5.8 Transverse momentum resolution

In this section a study of the transverse momentum resolution of the CTD and the MVD is presented. The track fit is done with CTD only tracking and compared to the tracking including the microvertex detector hits.

The transverse momenta (p_t) of the reconstructed tracks are compared with the "true" values from the generator. The relative difference is studied: $(p_{t,\mathrm{rec}} - p_{t,\mathrm{true}})/p_t$. The resulting distribution is fitted in bins of p_t. The fit gives a mean and a σ. The results are shown in figure 5.26.

For lower momenta the reconstructed momentum becomes smaller than the true value. This is due to the fact that the energy loss is not taken into account in the reconstruction. The energy loss of a 500 MeV muon is 1% (see figure 5.26a), corresponding to 5 MeV. If all the traversed material was silicon then this would correspond to a thickness of 0.5 cm (5% of a radiation length).

Since the MVD material distribution is known, the track fit algorithm could be extended by estimating the average energy loss per traversed layer and subsequently by correcting the track momentum.

For high momenta the MVD gives a better resolution. For low momenta the resolution is similar. Also shown is the "official" parameterisation of the CTD transverse momentum resolution [51]:

$$\sigma(p_t)/p_t = 0.0058 p_t \oplus 0.0065 \oplus 0.0014/p_t. \tag{5.4}$$

The new parameterisation using the MVD is:

$$\sigma(p_t)/p_t = 0.0026 p_t \oplus 0.0104 \oplus 0.0019/p_t. \tag{5.5}$$

5.6 Conclusion

After the final assembly and with the help of a cosmic trigger the first tracks were measured with the microvertex detector in the system test. A large sample of cosmic rays was collected. These data were analysed and showed a hit residual of approximately 70 µm. In total 98% of the MVD modules were working properly. Furthermore a first estimate of the hit finding efficiency resulted in an average efficiency of 97.7%.

After the MVD was installed inside ZEUS the whole data taking was integrated into the global data acquisition. More cosmic ray data were recorded. These data were used to align the MVD with the CTD and the MVD ladders internally. An estimate of the impact parameter resolution as function of the track momentum could be made. The result is: $\sigma_{\mathrm{imp}} = 0.83/p_t + 0.047$ mm. which satisfies the design criterium requiring that the impact parameter is better than 100 µm. Future studies will improve the geometry constants and the cluster position reconstruction in the MVD. Then even better resolution is achievable. An estimate of the ultimate precision has been obtained with a Monte Carlo simulation.

The performance of the track fit was studied with the ZEUS Monte Carlo simulation including the new MVD simulation. The fit procedure can find hits and tracks with high efficiency in the MVD barrel region. Furthermore the size of the residuals of the track fit were studied. They depend on the number of hits and the track momentum. The detector

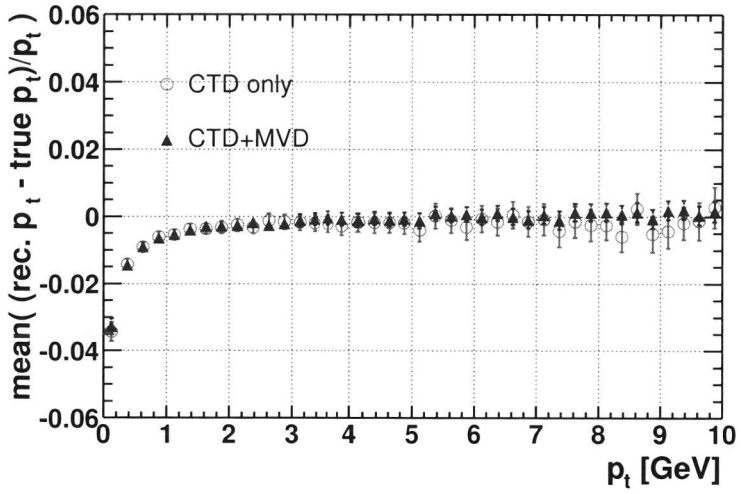

(a)

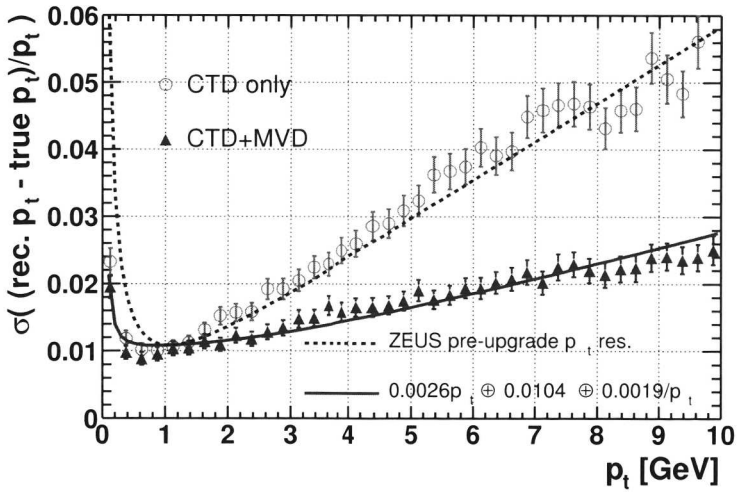

(b)

Figure 5.26: Study of the transverse momentum resolution (p_t) of the CTD and MVD fitted tracks.

misalignment was not simulated in the Monte Carlo. The impact parameter resolution can be described by the parameterisation: $\sigma_{\text{imp}} = 0.056/p_t + 0.018\,\text{mm}$. Hence if the MVD is well aligned this excellent resolution is achievable. The centre of gravity clustering algorithm was used. More precise clustering methods exist. Future improvements can improve the hit resolution which will also lead to an improved impact parameter resolution. The method to include the effect of multiple scattering in the track fit improves the impact parameter for tracks below 1 GeV significantly.

Finally the momentum resolution was studied. The resolution can be parameterised by: $\sigma(p_t)/p_t = 0.0026p_t \oplus 0.0104 \oplus 0.0019/p_t$. Comparing this to the CTD data it is seen that for low momentum tracks the resolution is similar but for high momentum tracks an improvement of a factor two is achieved.

In the following chapter the tracks in real ep collisions are reconstructed and they are combined to study the production of D mesons which are due to heavy quark production. The high precision available with the MVD should allow to observe charm events with displaced tracks and vertices.

Chapter 6

Charm in the HERA-II data

The HERA-II data, recorded from October 2002 until April 2004, are analysed in this chapter. The detector and fits as described in the previous chapters are used, to search for charm production in the data sample.

The selection criteria to obtain a sample of neutral current deep inelastic scattering events are described.

The decay of the K^0_S meson to two charged pions: $K^0_S \to \pi^+\pi^-$ is used to investigate the secondary vertexing.

The integrated luminosity is small. However a small number of charm events is found in the data including the microvertex detector (MVD). To study the charm events first the track selection is described. The studied charm decays are $D^{*+} \to D^0\pi^+$ (and c.c.) with the subsequent decay $D^0 \to K^-\pi^+$, and $D^+ \to K^-\pi^+\pi^+$ (and c.c.).

6.1 Event selection

During and after data taking the quality of the data is checked. Data runs that are useful for analysis are selected if a minimal number of detector components are functioning properly. Normally a run is declared good if the data of the calorimeter (CAL), the central tracking detector (CTD) and the luminosity measurement (LUMI) have good quality. Also a list of runs with "good" MVD is available.

An overview of the amount of integrated luminosity available for physics analysis is given in table 6.1. The total amount is $10.4\,\mathrm{pb}^{-1}$. Because some runs were not yet available off-line the integrated luminosity of the used data is $9.8\,\mathrm{pb}^{-1}$.

One of the events recorded in 2002 is shown in figure 6.1. This is an event with high Q^2 ($Q^2 \approx 4100\,\mathrm{GeV}^2$). The energy deposits in the CAL correspond to the scattered

	Oct 02 - Mar 03	Oct 03 - Dec 03	Jan 04 - Mar 04
physics [nb^{-1}]	971	2125	8066
with MVD [nb^{-1}]	801	1986	7681

Table 6.1: Different run periods with the amount of integrated luminosity for good physics runs and physics runs with reliable MVD data.

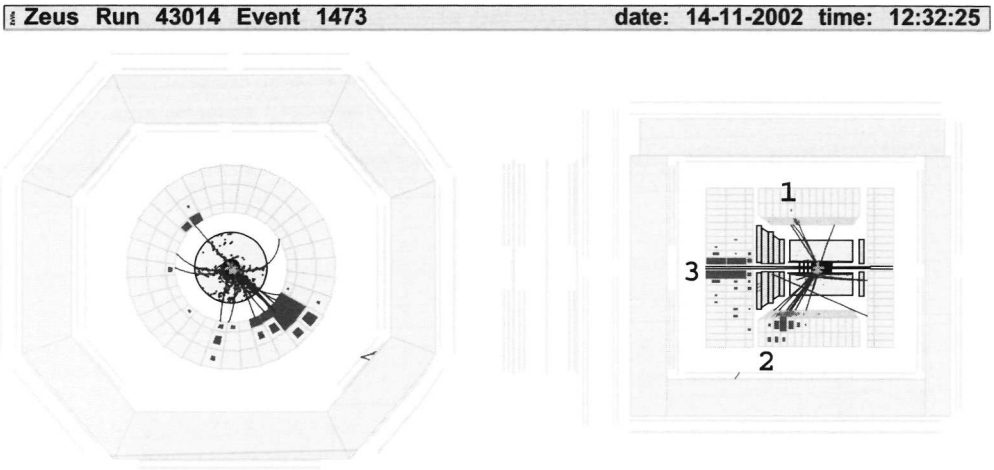

Figure 6.1: A high Q^2 DIS event is shown. The event was recorded in 2002. At the lefthand side the event is shown in the xy view, at the righthand side in the zr view. In the zr view are indicated: 1) the scattered positron, 2) the quark jet and 3) the proton remnant.

positron, the current jet and the proton remnant. Also the tracks in the CTD are clearly seen.

6.1.1 DIS sample

In this section the DIS sample is described. The event selection is similar as was done for the ZEUS inclusive F_2 measurement [52] for HERA I data. The following selection was applied.

Selection 1

- z-position of event vertex: $-50 < z < 50\,\text{cm}$
- Energy distribution in the calorimeter: $30 < E - p_z < 70\,\text{GeV}$
- Scattered positron: At least one candidate with probability larger than 0.7 and energy measured with the CAL larger than 8 GeV.
- Tracking: At least 2 CTD tracks in the event.

To get an inclusive sample no trigger information was used. After the criteria were applied 1903874 events remained. This is a rough selection, and photoproduction and off-momentum positron background are still present.

In figure 6.2 some important event variables are plotted. The method to determine Q^2 and x was the double angle method [53]. This method uses both the angle of the scattered positron and the hadronic system (quark jet).

A more pure DIS sample is selected by extending selection 1 with the following requirements:

Selection 2

- Calorimeter: $38 < E - p_z < 65\,\text{GeV}$
- Calorimeter: $p_t/E_t < 0.7$
- Calorimeter: $p_t/\sqrt{E_t} < 3\,\text{GeV}^{1/2}$
- "Box cut" for the scattered positron at the RCAL face: $-10 < x < 10\,\text{cm}$ and $-13 < y < 13\,\text{cm}$.

These criteria reduce the number of events to 1383930 and the effect on the distribution of the event variables is seen by the shaded area in figure 6.2. In particular the energy spectrum of the scattered positron improves.

For the search for charm production in the DIS sample is started with selection 1. For future cross sections measurements the selection of a pure DIS sample will be important.

6.1.2 Beam spot studies

The beam spot is defined as the region of positions where ep interactions took place over a certain time. The primary vertex is the point where the ep collision took place for one single event. During data taking the beam was not always in the same position. In this section the beam spot position is studied for all data runs, and also during the run.

To find the beam spot the Kalman vertex algorithm is used in the unconstrained mode (see section 4.3). In this mode no beam spot information is used. All x, y and z coordinates of the resulting vertices are stored after the vertex fit. The vertices are analysed further. First ep events are selected. The DIS sample contained too low statistics to study the beam spot on a run by run basis. Secondly, vertices that are originating from secondary interactions in the material of the detector are removed.

The following rough selection is done to remove most of the background events:

- RCAL time−FCAL time $> -8\,\text{ns}$. This reduces proton beam-gas events and proton beam halo muons.
- CAL $E_t > 5\,\text{GeV}$ and CAL $p_t < 5\,\text{GeV}$. This reduces proton beam-gas events. Here E_t is the transverse energy in the calorimeter. The p_t is here the sum of the "momentum" vectors of all CAL deposits projected on the xy plane.
- At least one "good track": The track has hits in CTD super layer 1, 2 and 3. This filters out off-momentum positron events.

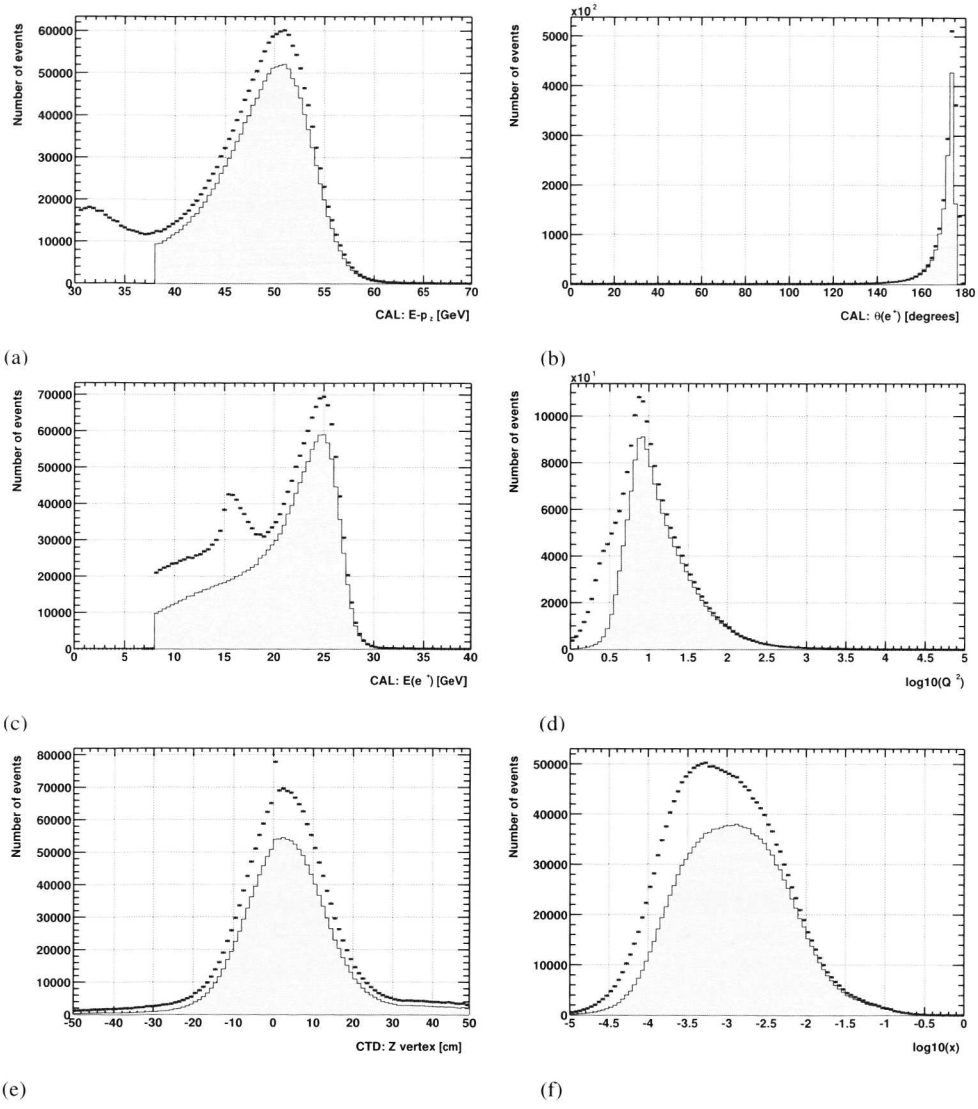

Figure 6.2: Distributions of $E - p_z$ (a), the angle of the scattered positron θ_e (b), the energy of the positron E_e (c), $\log_{10} Q^2$ (d), z vertex position (e) and $\log_{10} x$ (f). The dots are the distributions after event selection 1. The shaded area is after stronger selection criteria were applied (selection 1 and selection 2).

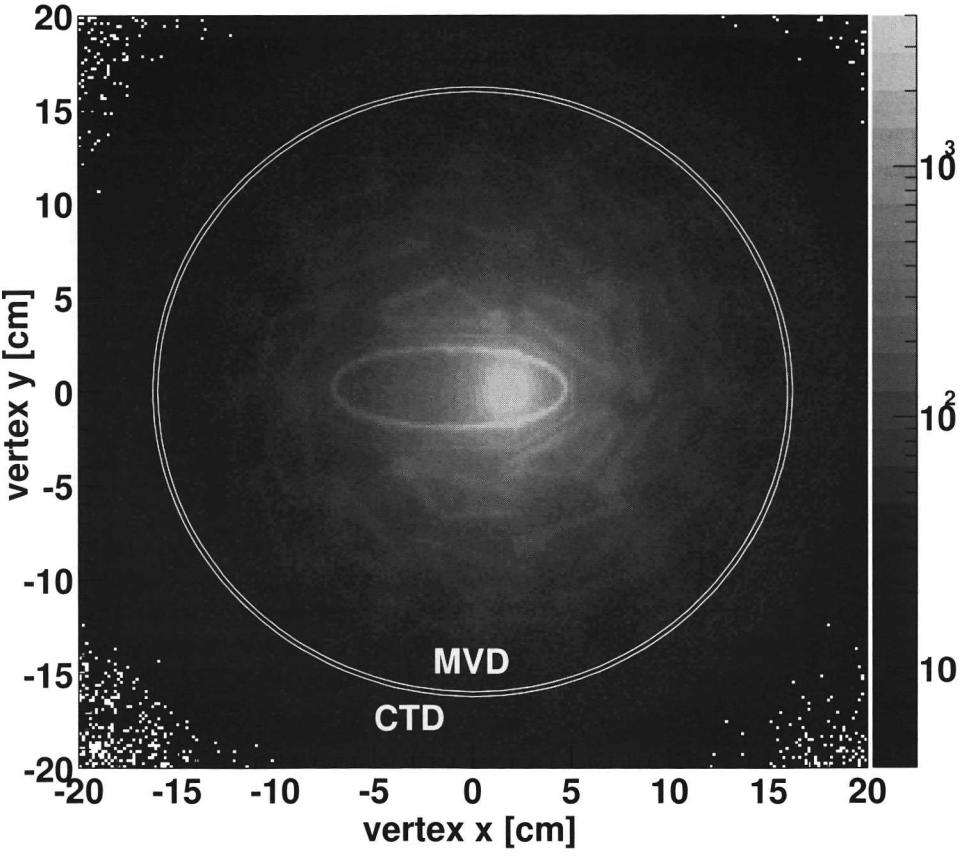

Figure 6.3: All vertices are shown that are found in the beam spot study in the MVD barrel region. The maximum number of entries per bin is set to 4000. The structure of the material in the MVD is clearly seen.

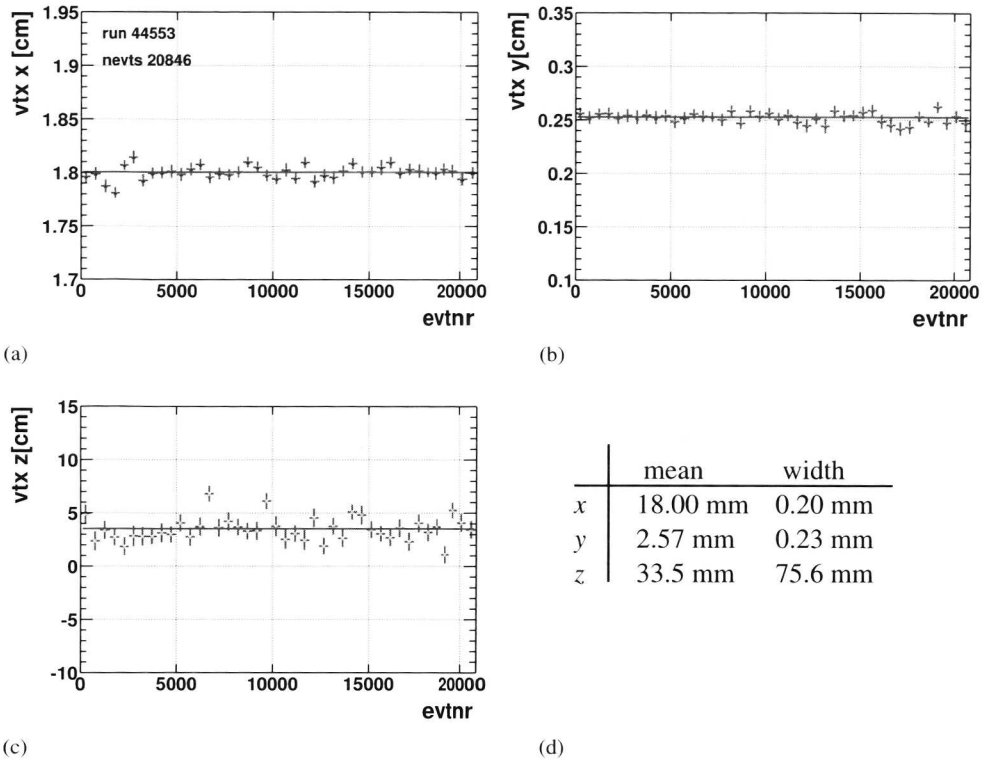

	mean	width
x	18.00 mm	0.20 mm
y	2.57 mm	0.23 mm
z	33.5 mm	75.6 mm

Figure 6.4: Distribution of the vertex position in x (a), y (b) and z (c) in bins of approximately 500 events for one single run with 20k events. In (d) are shown the fitted beam spot parameters for the whole run.

Figure 6.3 shows all reconstructed vertices, for the selected events, in the xy plane with $-25 < z < 25\,\text{cm}$. The interactions in the material of the beam pipe and the MVD ladders are clearly seen. Also the triangular structure of the ladders is seen. Around the beam pipe, the electrical shielding tube which has a thickness of 0.5 mm is also observed.

For the estimation of the beam spot position only the vertices inside the beam pipe are interesting. Vertices are selected if they are inside a cylinder with $-50 < z < 50\,\text{cm}$ and $0 < r < 1.75\,\text{cm}$. The centre of the cylinder is: $(x_0, y_0) = (1.8, 0)\,\text{cm}$. The mean position and width are determined with a Gaussian fit.

In figure 6.4d the fitted beam spot parameters for one single run are shown. The large width of the z distribution is dominated by the proton beam profile.

The stability of the beam spot position is studied for each single run. The method is to divide the data in bins of approximately 500 events. The result for one run is shown in figure 6.4. Overall the vertex position is constant during the run. Deviations of the order of 100 µm sometimes occur in the x and y direction. In precise vertexing studies it is therefore important to calculate the primary vertex for each event separately.

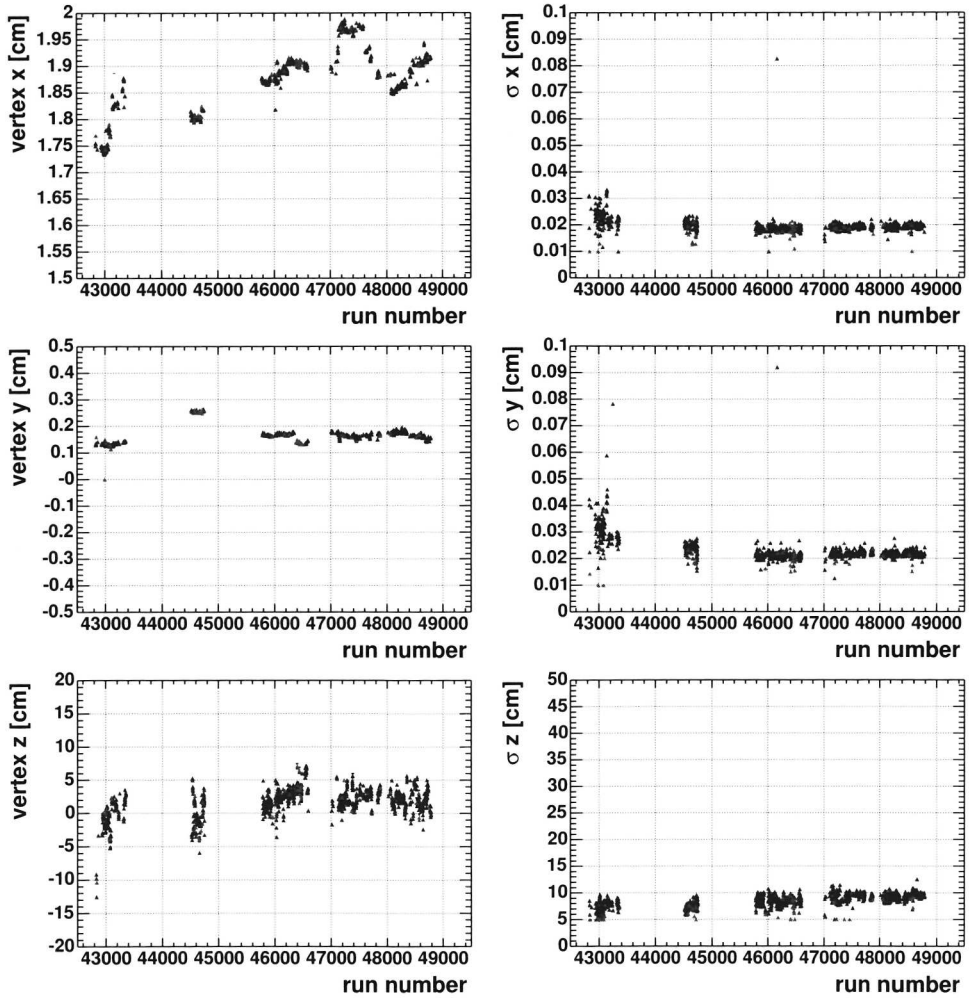

Figure 6.5: The position and the size of the beams pot in x, y and z for all 2002, 2003 up to 2004.

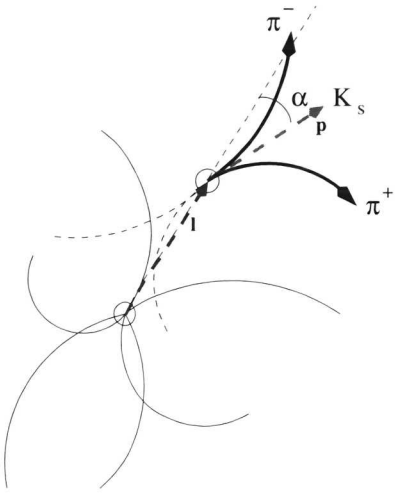

Figure 6.6: Schematic representation of a secondary decay of a K_S^0 meson into a $\pi^-\pi^+$ pair.

For this thesis the beam spot position and width is determined for all good ep physics runs with the MVD for 2002, 2003 and up to April 1st 2004. The results are shown in figure 6.5.

6.1.3 Secondary vertexing

After the primary vertex is fitted the remaining tracks are used to find secondary vertices. In figure 6.3 the secondary vertices are also shown. These vertices can be real particle decays: for example $K_S^0 \rightarrow \pi^-\pi^+$ and $\Lambda \rightarrow p\pi^-$ or interactions in the beam pipe or in the material of the detector: for example photon conversions ($\gamma \rightarrow e^+e^-$). Also random combinations of tracks can be fitted to a secondary vertex.

To study the secondary vertexing K_S^0 decays are examined. The average decay length of the K_S^0 is $\gamma c\tau = \gamma 2.68\,\text{cm}$ [12], where γ is the Lorentz boost of the particle. The K_S^0 mass is 0.498 GeV.

In figure 6.6 a picture of a decay of a K_S^0 meson into a charged pion pair is shown. The method is to select track pairs from secondary vertices. Only secondary vertices which fit to two tracks, with opposite charge, are selected. It is assumed that the two tracks are pions so the pion mass is assigned to them. Then the momentum four-vector of the candidate is calculated. If the candidate was a real K_S^0 then the invariant mass is expected to be close to 0.498 GeV.

Also random combinations and backgrounds can occur in this mass region. To reduce the background, candidates are selected with larger momentum. The background is reduced further by requiring that the flight direction of the K_S^0 is consistent with originating from the primary vertex ("pointing back").

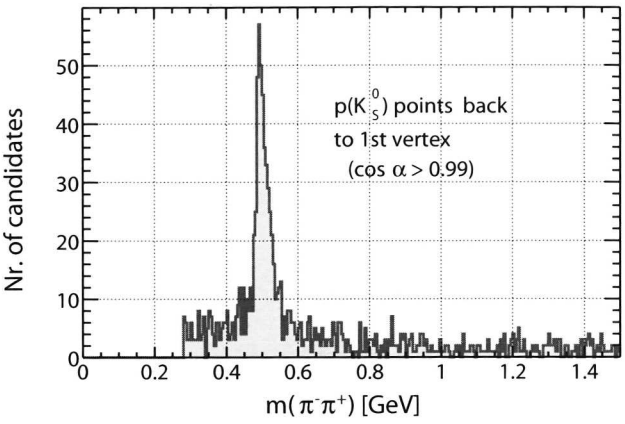

Figure 6.7: Invariant mass spectrum of the K^0_S candidates. The tracks are fitted with the CTD and the MVD. For each candidate was required $p_t(K^0_S) > 0.2\,\text{GeV}$. Also each candidate was required to "point back" to the primary vertex: $\cos\alpha > 0.99$.

In figure 6.7 a clear peak is seen at the K^0_S mass. The figure shows the result from tracks fitted with the MVD and the CTD from DIS data recorded in 2002.

The number of detected K^0_S decays can be estimated with the post-upgrade tracking (MVD and CTD) and with CTD-only tracking. With the post-upgrade tracking four times more K^0_S mesons are found. From figure 6.8 it is seen that the gain is coming from the "short living" decays (small $c\tau$). Down to $c\tau = 3\,\text{cm}$ an equal number of K^0_S decays are found with the CTD-only and with the MVD . The gain comes from vertices with $c\tau < 3\,\text{cm}$.

6.2 Track selection

For the charm quark measurements (presented in the next section) the effect of using different types of tracks is investigated. For this purpose three different samples are formed for each event. These are:

type 1: CTD-only tracks that fit to the CTD primary vertex.

This selection is based on the VCTRAK reconstruction program which is used by the ZEUS collaboration to fit and vertex CTD tracks.

type 2: MVD fitted tracks that fit to the MVD primary vertex.

This selection is based on the Kalman tracking and vertex package as described in chapter 4

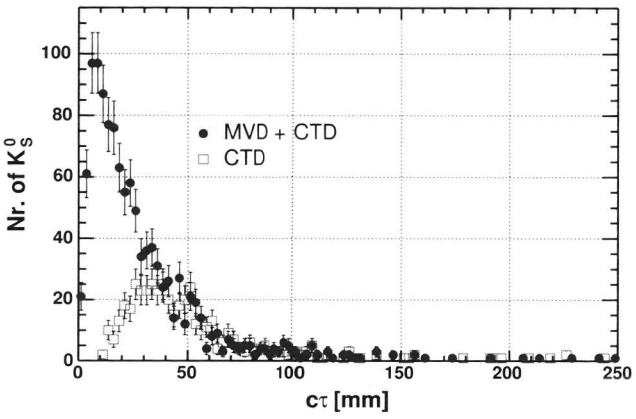

Figure 6.8: The $c\tau$ of the K^0_S candidates. The MVD finds more K^0_S mesons and they are found in particular in the region close to the primary vertex.

type 3: MVD fitted tracks that fit to the MVD primary vertex and tracks that originate from nearby the primary vertex.

This selection is made because a reasonable fraction of the produced charmed hadrons is expected to decay outside the primary vertex position envelope.

In the remaining part of this section the track selection is described in more detail. In the analysis the selected tracks are considered event by event.

First the type 1 tracks are discussed. These are tracks fitted with only the information from the CTD. The track fit and vertexing is done with VCTRAK. The following selection is done before the primary vertex fit is performed:

- at least 1 hit in super layer 1
- at least 2 CTD z hits and 2 CTD "axial" hits.
- point of closest approach compatible with beam spot
- "Loopers" are rejected. These are low p_t tracks.

Before tracks are stored for analysis the following selection is performed:

- track $p_t > 20\,\mathrm{MeV}$
- at least 2 CTD z hits
- track $|\eta| < 1.9$

- track $\chi^2/\mathrm{ndf} < 10$

The pseudorapidity η is defined as: $\eta = -\ln(\tan(\theta/2))$.

The type 2 tracks are based on MVD fitted tracks. The vertexing is done with the Kalman filter vertexing algorithm described in section 4.3.2. The offline reconstruction was corrected for the MVD off-set with respect to the CTD. The MVD ladder corrections were not yet implemented. This would improve the impact parameter resolution with a factor two.

Input for the vertexing are the calculated beam spot positions. For all tracks at least one MVD hit or CTD hits in super layer 1, 2 and 3 in the CTD were required. The selection is much looser than for the VCTRAK vertexing. Optimisation studies have to be done in the future. After the primary vertex fit is done, tracks that fit to this vertex are called primary vertex tracks. Remember that the momentum vector of each track is then fitted to the primary vertex position (vertex re-fitted tracks).

The impact parameter resolution of a well measured MVD track is about 100 µm. After a few iterations the error on the vertex position becomes of the same order. It is then possible that tracks coming from short living hadrons do not fit to the primary vertex. To study this, the "nearby" track sample is formed:

- For secondary vertices within $|z| < 50\,\mathrm{mm}$ from the primary vertex and transverse distance $r < 12.5\,\mathrm{mm}$ from the primary vertex, all tracks are marked as "nearby".
- For tracks not fitting to any vertex the point of closest approach to the primary vertex is calculated. These tracks are marked as "nearby" if the point of closest approach is within $|z| < 50\,\mathrm{mm}$ and $r < 12.5\,\mathrm{mm}$ from the primary vertex.

Together with the type 2 tracks the "nearby tracks" form the type 3 tracks.

To compare between the MVD fitted tracks and the CTD-only primary vertex tracks the following selection is done for all three types:

- CTD hits in super layer 1, 2 and 3.
- $|\eta| < 1.5$

In the following sections the selected tracks are input to the reconstruction of $D^{*\pm}$ and $D^{\pm}$ mesons. The three different types of tracks are then called: CTD only, MVD and CTD primary tracks and MVD and CTD primary and nearby tracks.

6.3 $D^{*\pm}$ reconstruction

The reconstruction of the decay: $D^{*+} \rightarrow D^0\pi^+$ (and c.c.), with the subsequent decay of $D^0 \rightarrow K^-\pi^+$, is a well known method to tag charm quarks. This method is used to tag charm quarks in deep inelastic scattering data from HERA-I (see section 1.3.4). In this section this decay is reconstructed in the HERA-II DIS data (see section 6.1.1) and compared to the results from the HERA-I data.

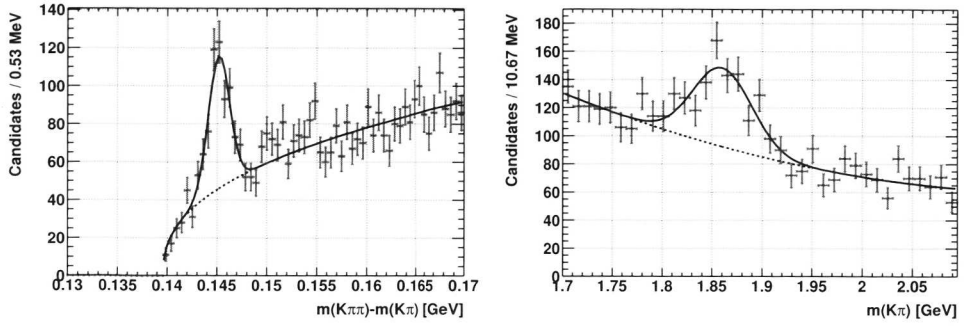

(a) (b)

Figure 6.9: In (a) the mass difference, $\Delta m = m(K\pi\pi) - m(K\pi)$, for $D^{*\pm}$ candidates (dots). The solid line shows the result of the fit described in the text. In (b) the $m(K\pi)$ distribution for the D^0 candidates in the range $0.143 < \Delta m < 0.148\,\text{GeV}$. The D_0 signal is fitted with a Gaussian signal function on top of a second order polynomial background function.

6.3.1 Reconstruction method

The D^{*+} mesons are identified using the decay channel $D^{*+} \to D^0\pi_s^+$ with the subsequent decay $D^0 \to K^-\pi^+$. The π_s^+ refers to a low momentum ("slow") pion accompanying the D^0. The reconstruction for the D^{*-} is similar except that all charges are opposite.

Charged tracks fitted by the central tracking detector (CTD) and microvertex detector (MVD) are selected. Only tracks fitting to the primary vertex are selected.

Tracks with opposite charges and transverse momenta $p_t > 0.4\,\text{GeV}$ are combined in pairs to form D^0 candidates. The tracks are alternately assigned the masses of a kaon and a pion and the invariant mass of the pair $m(K\pi)$ is calculated. It is not known if the D^0 candidate has the configuration $K\pi$ or πK. The ambiguity is resolved by the charge of the third track (with $p_t > 0.12\,\text{GeV}$). Each additional track with charge opposite to that of the kaon track, is assigned the pion mass and combined with the "correct" D^0 candidate to form a $D^{*\pm}$ candidate.

In figure 6.9 the mass difference $\Delta m = m(K\pi\pi) - m(K\pi)$ and the D^0 mass $m(K\pi)$ are plotted. For the $D^{*\pm}$ candidates $p_t(D^{*\pm}) > 1.5\,\text{GeV}$ and pseudorapidity $|\eta(D^{*\pm})| < 1.5$ is required. The signal to background is enhanced by requiring respectively $1.80 < m(K\pi) < 1.92\,\text{GeV}$ and $0.143 < \Delta m < 0.148\,\text{GeV}$.

To obtain the number of $D^{*\pm}$ the Δm distribution is fitted using the following equation:

$$f(\Delta m) = p_1 \exp(-0.5[(\Delta m - p_2)/p_3]^2) + p_4(\Delta m - m_\pi)^{p_5}, \tag{6.1}$$

where p_1 to p_5 are free parameters and m_π is the pion mass. The equation is the sum of a Gaussian signal function and a background function. In figure 6.9a the Gaussian has its peak value at $p_2 = 145.183 \pm 0.103\,\text{MeV}$. (The PDG value is $145.436 \pm 0.016\,\text{MeV}$ [12]). The fitted width (p_3) is $1.07 \pm 0.11\,\text{MeV}$.

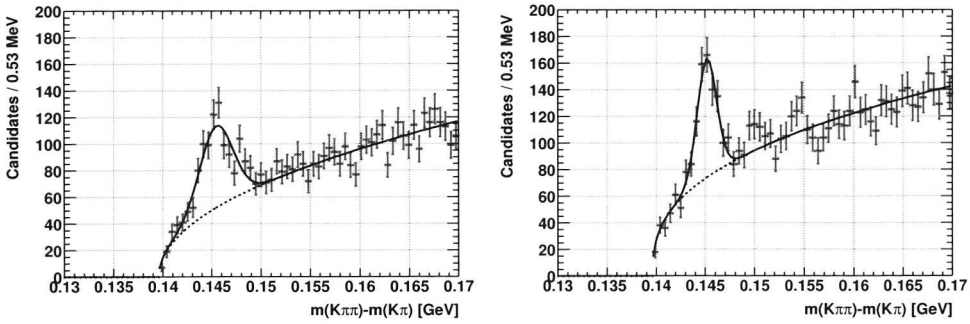

(a) (b)

Figure 6.10: In (a):The mass difference Δm is plotted for $D^{*\pm}$ candidates measured with tracks fitted only with the CTD. In (b): The mass difference is plotted for tracks fitted with both the CTD and the MVD. The track selection includes secondary tracks (see text).

The number of signal and background events are calculated by integrating the signal and the background function in a three sigma interval around the peak.

The number of signal events is N and the number of background events is B. The statistical error is defined as $\sqrt{N+B}$. The significance is defined as $N/\sqrt{B}$. The number of candidates in figure 6.9a is then $348 \pm 19 \pm 23 = 348 \pm 27$. The significance is $348/23 = 15.1$.

In the remaining part of this section $D^{*\pm}$ production is studied for different p_t and Q^2. Also comparisons are made with the CTD tracking and the MC simulation.

6.3.2 CTD and MVD comparison

The $D^{*\pm}$ signal for CTD-only tracks and tracks fitted with MVD and CTD is compared. For the MVD two samples are used: one with only the primary vertex tracks and one with primary and secondary tracks close to the primary vertex ("nearby tracks").

In figure 6.10a the mass difference with the CTD only tracks is plotted. The distribution is wider than the distribution in figure 6.9a (1.70 ± 0.20 MeV). The fitted number of candidates is larger ($488 \pm 22 \pm 31 = 488 \pm 38$). In figure 6.10b the mass difference is shown for the sample of primary and nearby tracks. The fitted width is 0.97 ± 0.10 and the number of candidates is $407 \pm 20 \pm 28 = 407 \pm 35$. These results are tabulated in table 6.2.

The comparison is done for different values of the minimal $p_t(D^{*\pm})$ and $|\eta(D^{*\pm})| < 1.5$). For larger p_t it is seen that the number of candidates for CTD tracks and the MVD primary and nearby tracks agrees within the errors. For $p_t > 1.5$ a 2σ difference is observed, while no large difference is expected. The width of the fitted Gaussian is smaller for both the MVD track samples.

The number of candidates stays less with the MVD primary tracks. Some tracks

ZEUS 02 - April 04. $\mathcal{L} = 9.8\,\text{pb}^{-1}$

	$p_t > 1.5\,\text{GeV}$		$p_t > 2.0\,\text{GeV}$	
	N_{cand}	σ [MeV]	N_{cand}	σ [MeV]
CTD	488±22±31	1.70±0.20	403±20±25	1.81±0.21
MVD+CTD p	348±19±23	1.07±0.11	326±18±17	1.01±0.09
MVD+CTD p+s	407±20±28	0.98±0.10	385±20±21	0.94±0.08

	$p_t > 3.0\,\text{GeV}$	
	N_{cand}	σ [MeV]
CTD	205±14±14	1.50±0.17
MVD+CTD p	184±14±10	0.99±0.11
MVD+CTD p+s	238±15±13	1.04±0.12

Table 6.2: $D^{*\pm}$ in the data. Different track selections are compared: CTD-only fitted and MVD+CTD fitted tracks. Selection "MVD p" consists of tracks fitting to the primary tracks. Selection "MVD p+s" consists of both primary tracks and secondary tracks as defined in the previous section. The width and the signal of the mass difference Δm are fitted for different cuts on $p_t(D^{*\pm})$. The statistical error for the number of candidates is written down as $N \pm \sqrt{N} \pm \sqrt{B}$.

coming from the $D^{*\pm}$ do not fit to the primary vertex because the D^0 decay length is of the same order as the vertexing precision.

From these results it can be concluded that a fraction of more than 10% of the $D^{*\pm}$ decays do not fall in the primary vertex envelope. The "missing" $D^{*\pm}$ can be found back by including secondary tracks.

The studied $D^{*\pm}$ is tagged efficiently because the mass difference gives a clear signature. The only way the MVD can increase the number of $D^{*\pm}$ measured is by increasing the phase space of the measurement. This is possible when data from the forward tracking is included.

The MVD can be used to improve the track selection and to decrease the width of the Δm signal. This will decrease the error on the number of measured $D^{*\pm}$ decays and improve the measurement of charm.

An additional use of the $D^{*\pm}$ decay is that a large number of D^0 candidates can be tagged. This tagged D^0 can be used to calibrate displaced vertex finding algorithms for other decays, for example the $D^{\pm}$.

6.3.3 Comparison with Monte Carlo simulation and HERA-I data

In this section the number of $D^{*\pm}$ decays is compared with the HERA-I data and a charm Monte Carlo sample, equivalent to $56\,\text{pb}^{-1}$.

To compare with HERA-I the number of $D^{*\pm}$ candidates has been estimated for different Q^2 regions (with $p_t(D^{*\pm}) > 1.5\,\text{GeV}$ and $|\eta(D^{*\pm})| < 1.5$). The results are presented in table 6.3. High Q^2 DIS events are triggered very efficiently in ZEUS. For $Q^2 > 40\,\text{GeV}^2$,

ZEUS 02- April 04. $\mathcal{L} = 9.8\,\mathrm{pb}^{-1}$

	$Q^2 > 1.5\,\mathrm{GeV}^2$		$Q^2 > 10\,\mathrm{GeV}^2$	
	N_{cand}	σ [MeV]	N_{cand}	σ [MeV]
CTD	468±22±30	1.65±0.22	239±15±21	1.31±0.19
MVD+CTD p	338±18±23	1.06±0.11	167±13±17	0.92±0.13
MVD+CTD p+s	396±20±28	0.97±0.10	234±15±21	0.91±0.12

	$Q^2 > 40\,\mathrm{GeV}^2$	
	N_{cand}	σ [MeV]
CTD	91±10±15	1.61±0.42
MVD+CTD p	56±7±10	0.86±0.19
MVD+CTD p+s	81±9±14	0.95±0.24

Table 6.3: $D^{*\pm}$ in the data. Different track selections are compared: CTD-only fitted and MVD+CTD fitted tracks. Selection "MVD p" consists of tracks fitting to the primary tracks. Selection "MVD p+s" consists of both primary tracks and secondary tracks as defined in the previous section. The width and the signal of the mass difference Δm are fitted for different Q^2 regions. The statistical error for the number of candidates is written down as $N \pm \sqrt{N} \pm \sqrt{B}$. ($p_t(D^{*\pm}) > 1.5\,\mathrm{GeV}$ and $|\eta(D^{*\pm})| < 1.5$).

8.26 ± 1.69 $D^{*\pm}$ decays are observed per pb^{-1} of data. For HERA-I data, 8.20 ± 0.22 decays per pb^{-1} are measured in the same measurement range [15] (only statistical error included). The HERA-II trigger strategy accepts less events at low Q^2. The comparison for low Q^2 is difficult because the trigger acceptance has not yet been calculated.

For the Monte Carlo sample the same is done. The results are presented in table 6.4. The equivalent luminosity is 5.7 times that of the data. In the simulation the tracking resolution is better than in data. The width of the mass differences is smaller than in table 6.3. In the MC, the width of the Δm peak is for the MVD fitted tracks about 0.20 MeV smaller than for the CTD fitted tracks

Overall it can be said that the $D^{*\pm}$ mesons can be well measured with the MVD. The CTD measured this already very well in the HERA-I data, resulting in a measurement of charm production in DIS. To measure the $D^{*\pm}$ meson the observation of the "slow" pion is very important. Since the MVD is installed, this particle will undergo some extra scattering in the material of the MVD (10% of a radiation length). The additional number of measured hits with the MVD compensate for this. (In the Monte Carlo study (see chapter 5) it was seen that the momentum resolution for low momentum tracks has not changed much.)

In HERA-I data, only the primary vertex tracks are used to find the $D^{*\pm}$. It was shown that for the HERA-II data, a large fraction of the D^0 mesons decay outside the primary vertex envelope. In the next section we will take advantage of this to tag $D^{\pm}$ decays.

Monte Carlo (RAPGAP). $\mathcal{L} = 56\,\mathrm{pb}^{-1}$

	$Q^2 > 1.5\,\mathrm{GeV}^2$		$Q^2 > 10\,\mathrm{GeV}^2$	
	N_{cand}	σ [MeV]	N_{cand}	σ [MeV]
CTD	2677±52±28	1.14±0.03	1651±41±23	1.13±0.04
MVD+CTD p	2317±48±22	0.88±0.02	1395±37±18	0.86±0.03
MVD+CTD p+s	2751±52±28	0.92±0.02	1700±41±23	0.90±0.03

	$Q^2 > 40\,\mathrm{GeV}^2$	
	N_{cand}	σ [MeV]
CTD	498±22±16	1.02±0.06
MVD+CTD p	405±20±11	0.77±0.05
MVD+CTD p+s	530±23±15	0.79±0.04

Table 6.4: Number of $D^{*\pm}$ and width of the Δm signal in the Monte Carlo simulation. Different track selections are compared: CTD-only fitted and MVD+CTD fitted tracks. Selection "MVD p" consists of tracks fitting to the primary tracks. Selection "MVD p+s" consists of both primary tracks and secondary tracks as defined in the previous section. The width and the signal of the mass difference Δm are fitted for different Q^2 regions. The statistical error for the number of candidates is written down as $N \pm \sqrt{N} \pm \sqrt{B}$. (with $p_t(D^{*\pm}) > 1.5\,\mathrm{GeV}$ and $|\eta(D^{*\pm})| < 1.5$)

6.4 $D^{\pm}$ reconstruction

The $D^{\pm}$ mesons are reconstructed from the decay channel $D^+ \to K^- \pi^+ \pi^+$ (and c.c.). The $D^{\pm}$ has a mass of 1.869 GeV and the average $c\tau$ is 315 µm [12]. Relativistic particles are "boosted" with a factor γ. With the microvertex detector it should be possible to tag these decays by looking for decays separated from the primary vertex.

In each event all track pairs with equal charge and a third track with opposite charge are combined to form the $D^{\pm}$ candidates. The pion mass is assigned to the two tracks with equal charges and the kaon mass is assigned to the third track. Subsequently, the $D^{\pm}$ candidate invariant mass, $m(K\pi\pi)$ is calculated. Tracks are selected from the sample of primary and "nearby" secondary tracks. The transverse momentum p_t of a track is required to be larger than 0.4 GeV.

Candidates with $p_t(D^{\pm}) > 1.5\,\mathrm{GeV}$ and an invariant mass between 1.6 GeV to 2.2 GeV are re-vertexed. The $D^{\pm}$ vertex position is recalculated using the three decay tracks. The vertex re-fitted tracks are used to determine the $D^{\pm}$ invariant mass.

The remaining tracks are input to the primary vertex algorithm with the beam spot as initial estimate. The result is a new re-fitted vertex position. The distance between the new primary vertex and the $D^{\pm}$ vertex is used to tag $D^{\pm}$ decays.

First the invariant mass spectrum for a selection without cuts on the secondary vertex and track impact parameters is plotted. To suppress the combinatorial background, the following is required:

- $\cos\theta^*(K) > -0.75$

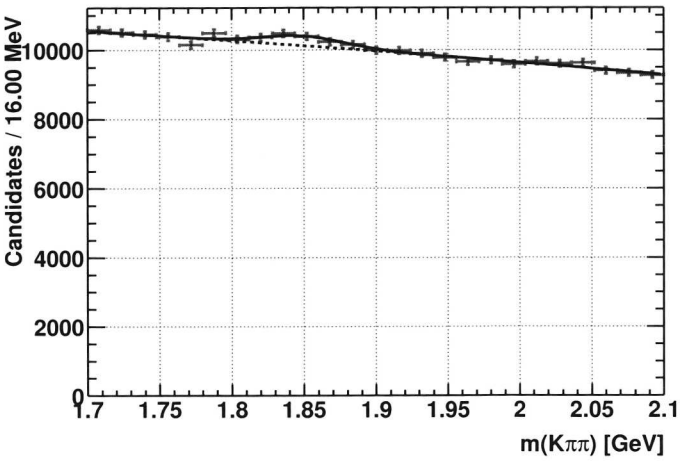

Figure 6.11: The invariant mass, $m(K\pi\pi)$, for $D^{\pm}$ candidates (dots). The solid line shows the result of the fit and estimates the signal and the background from random combinations.

where $\theta^*(K)$ is the angle between the kaon in the $K\pi\pi$ rest frame and the $K\pi\pi$ line of flight in the laboratory. Furthermore for the $D^{\pm}$ is required:

- $p_t(D^{\pm}) > 2.0\,\mathrm{GeV}$,
- $|\eta| < 1.5$.

The $K\pi\pi$ mass spectrum is shown in figure 6.11. The combinatorial background is huge but a $D^{\pm}$ bump is present. The fit is performed in the same way as for the D^0 invariant mass spectrum. The signal is described by a Gaussian and the background by a second order polynomial. From the fit the number of signal events is 1243 ± 331 on top of 108038 background events. Next an attempt is done to improve the signal over background by requiring the $D^{\pm}$ candidate to originate from a secondary vertex.

After the re-fitting of the $D^{\pm}$ candidate vertex and the primary vertex, the "signed" decay length l is defined as:

$$l = |\vec{L}|\mathrm{sign}(\vec{L} \cdot \vec{p}_{D^{\pm}}), \tag{6.2}$$

with $\vec{L} = \vec{S} - \vec{P}$. The primary vertex has position $\vec{P}$ and the secondary vertex has position $\vec{S}$. The re-fitted momentum vector of the $D^{\pm}$ is $\vec{p}_{D^{\pm}}$. In the case l is positive (negative) the decay is in front (behind the vertex). Secondly the uncertainty in the primary vertex and $D^{\pm}$ candidate position are both described by a covariance matrix. The errors (σ_{vtx} and $\sigma_{D^{\pm}}$) are calculated by projecting both covariance matrices on the decay vector. The decay length significance is defined as:

$$s_l = l/\sigma_l, \tag{6.3}$$

N signal	197±14
N background	978±31
mass peak [GeV]	1.870±0.004
width [MeV]	22.1±4.2

Table 6.5: Parameters of the $m(K\pi\pi)$ invariant mass fit in figure 6.12.

where $\sigma_l^2 = \sigma_{\text{vtx}}^2 + \sigma_{D^\pm}^2$.

Furthermore the impact parameter d of the helix track to the primary vertex can be calculated. The vector pointing from the primary vertex to the point of closest approach is $\vec{d}$. The signed impact parameter is:

$$d = |\vec{d}|\text{sign}(\vec{d} \cdot \vec{p}_{D^\pm}). \tag{6.4}$$

To determine the error σ_d the vertex covariance and track covariance are projected on the impact parameter vector. This results in the impact parameter significance: $s_d = d/\sigma_d$. For each of the three decay tracks the s_d is calculated with respect to the re-fitted primary vertex.

Candidates are selected if:

- at least 2 of the 3 tracks have an impact parameter significance s_d larger than 3 ($2 \times s_d > 3$).

This removes candidates that fit well to the primary vertex.

To select good quality $D^\pm$ candidates the candidates the following is required:

- The $D^\pm$ decay length error $\sigma_{D^\pm} < 0.5\,\text{mm}$.
- The χ^2 probability $P(\chi^2) > 0.05$.

This reduces the number of "bad" random vertices. The radial decay length is defined as $l_{xy} = l\sin(\theta)$, where θ is the polar angle of the $D^\pm$ candidate. Candidates are selected if:

- $|l_{xy}| > 1\,\text{mm}$.
- $|l_{xy}| < 5\,\text{mm}$.

These selections remove more background candidates.

A decay length significance is required:

- $s_l > 4$.

The resulting invariant mass spectrum is shown in figure 6.12. A clear mass peak is seen. The results of the fit are summarised in table 6.5. From the table it is seen that the background is reduced by factor 100 while the signal is reduced by factor 6 with respect to the previous selection. The result is a $D^\pm$ invariant mass signal with a significance of 6.4.

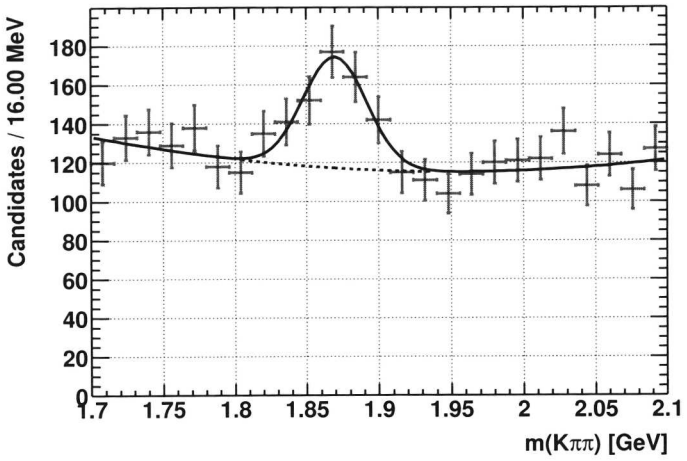

Figure 6.12: The $D^{\pm}$ invariant mass is shown, after secondary vertices are selected.

One of the candidate events is displayed in figure 6.13. It is a D^{+} candidate with a p_t of 5.1 GeV and decay length of 4.1 cm ($\gamma = 3.0$). All three decay tracks fit to a secondary vertex. An additional fourth track also fits to this secondary vertex. This track is seen in figure 6.13a as the low momentum track with negative charge, with corresponding energy loss in the electromagnetic calorimeter (electron candidate). Hence, the event seen here is a candidate for a semi-leptonic $\bar{B}^0$ decay: $\bar{B}^0 \rightarrow D^{+} e^{-} \nu_e$.

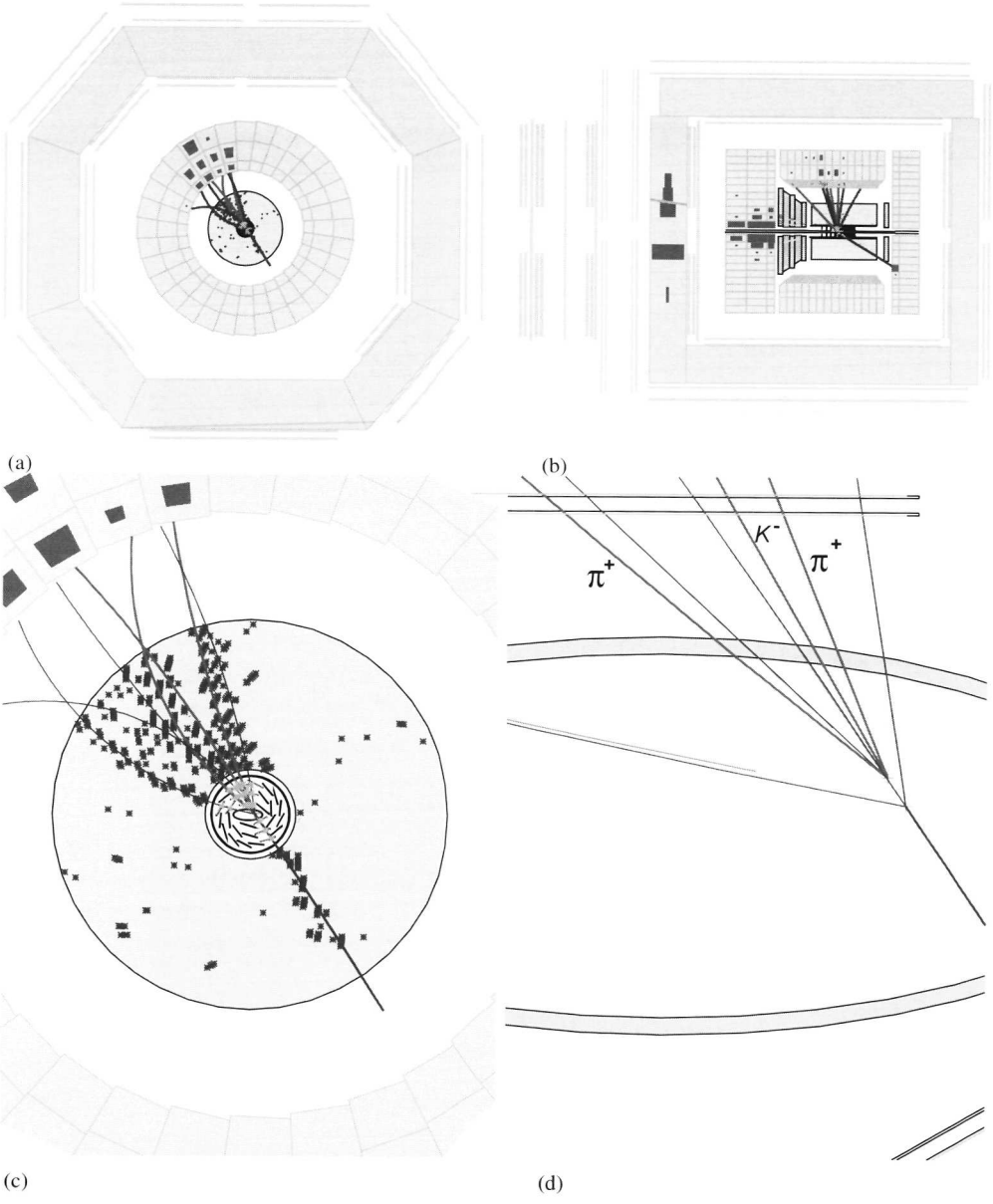

Figure 6.13: A D^+ candidate (ZEUS run 48121, event 53748) with a displaced secondary vertex is shown. In (a) the global xy-view, in (b) the rz-view, in (c) and (d) the event is zoomed in. The decay length of the $D^{\pm}$ candidate is 4.1 mm. Its p_t is 5.1 GeV and its mass is 1.863 GeV.

Chapter 7

Conclusions

The physics subject of this thesis is the measurement of the production of charm and bottom quarks in deep inelastic scattering. In this thesis data are included until April 2004, corresponding to an integrated luminosity of $9.8\,\mathrm{pb}^{-1}$. Due to the delay of the HERA program, the amount of available data is small. Hence, additional measurements will have to be done with future data. The HERA program is expected to continue until 2007.

The microvertex detector (MVD) has become a reliable ZEUS component and its data are available for analysis. The microvertex detector improves the ZEUS tracking significantly. An impact parameter resolution of $83/p_t + 47\,\mu\mathrm{m}$ is achieved in the analysis of cosmic ray tracks. The secondary decays of long living charm and bottom hadrons can be separated from the primary collision point. This was impossible before 2001, when the central tracking detector (CTD) was the most inner tracking chamber.

Although the performance is already better than what the goal of the proposal was, some recommendations for further improvements can be made.

First, the centre of gravity algorithm is used to reconstruct the position of a hit on the silicon sensor. Alternative position reconstruction can be done depending on the angle of incidence between the track and the sensor. These alternative methods will improve the hit resolution.

The detector geometry has been calibrated partially. The MVD position is calibrated with respect to the CTD, and the MVD ladders are aligned. This improves the impact parameter resolution of the MVD with a factor two (mentioned above). According to the Monte Carlo simulation, the impact parameter resolution is an additional factor two better. However, the design geometry is used in the simulation and the signal to noise ratio is assumed to be very high.

The impact parameter resolution depends on the φ angle of the track. This is due to the geometrical layout of the MVD. For tracks in the region $140^\circ < \varphi < 210^\circ$ the impact parameter resolution is a factor two worse. The efficiency of measuring a secondary decay depends strongly on φ.

Multiple scattering at lower track momentum contributes more and more to the track uncertainty. These uncertainties are taken into account. For low momentum tracks this improves significantly the result for the track impact parameter resolution.

From beam spot studies it is seen that the average width is approximately 200 µm in x and y. The beam spot is calculated for each run, and serves as an initial estimate for the primary event vertex fit.

Charm quarks are studied by identifying the decay $D^{*+} \to D^0\pi^+$ (and c.c), with the subsequent decay $D^0 \to K^-\pi^+$ and the decay $D^+ \to K^-\pi^+\pi^+$ (and c.c).

In the $D^{*\pm}$ channel 407 ± 35 candidates with $p_t(D^{*\pm}) > 1.5\,\text{GeV}$ and $|\eta| < 1.5$ are found in the data sample. This number is 2σ lower than what is found with the CTD. For larger $p_t(D^{*\pm})$ and in the MC simulation the number of $D^{*\pm}$ candidates is in agreement. The width of the signal peak is $0.97 \pm 0.10\,\text{MeV}$, however the ladder to ladder alignment is not applied. The measured width with the CTD is about 0.2 MeV larger.

For $Q^2 > 40\,\text{GeV}^2$ 81 ± 17 candidates are found. Assuming the detector acceptance in unchanged this result is in agreement with HERA-I data. To compare for lower Q^2 the trigger acceptance should be taken into account.

In the $D^\pm$ channel 1243 ± 331 candidates with $p_t(D^\pm) > 2\,\text{GeV}$ and $|\eta| < 1.5$ are found in the data sample. The candidates are re-fitted. After the re-fit the separation of the $D^\pm$ decay from the primary vertex is calculated. Selecting candidates with a large impact parameter significance, reduces the background strongly. In the HERA-II sample up to April 2004, 197 ± 34 candidates are found.

In this thesis it is shown that charm hadrons can be tagged by separating their decays from the primary vertex. The average decay length of a charm hadron is only a few 100 microns. The average decay length for bottom hadrons is even larger. The microvertex detector promises to be a powerful tool for the study of heavy quarks at HERA-II.

References

[1] Veltman, M. J. G., *Facts and mysteries in elementary particle physics.* River Edge, USA: World Scientific, 2003. 340 p.

[2] Particle Data Group, K. Hagiwara et al., *Review of particle physics.* Phys. Rev. **D 66**, 10001 (2002).

[3] Zhao, Qiang and Close, Frank E., *On the experimental status of theta+ and sigma(5)+ pentaquarks* (2004), hep-ph/0404075;
Chekanov, S. and others, *Evidence for a narrow baryonic state decaying to k0(s) p and k0(s) anti-p in deep inelastic scattering at hera.* Phys. Lett. **B591**, 7 (2004), hep-ex/0403051.

[4] M. Breidenbach et al., *Observed behaviour of highly inelastic electron-proton scattering.* Phys. Rev. Lett. **23**, 935 (1969):
E.D. Bloom et al., *High-energy inelastic ep scattering at* 6° *and* 10°. Phys. Rev. Lett. **23**, 930 (1969).

[5] R.K. Ellis, W.J. Stirling and B.R. Webber, *QCD and Collider Physics*, Cambridge Monographs on Particle Physics. Nuclear Physics and Cosmology, Vol. 8. Cambridge University Press, 1996.

[6] A.D. Martin et al., *MRST2001: partons and* α_S *from precise deep inelastic scattering and tevatron jet data.* Eur. Phys. J. **C**, 73 (2002), hep-ph/0110215.

[7] V.N. Gribov and L.N. Lipatov, *Deep inelastic ep scattering in perturbation theory.* Sov. J. Nucl. Phys. **15**, 438 (1972);
Yu.L. Dokshitzer, *Calculation of the structure functions for deep inelastic scattering and* e^+e^- *annihilation by perturbation theory in Quantum Chromodynamics [in Russian].* Sov. Phys. JETP **46**, 641 (1977):
G. Altarelli and G. Parisi, *Asymptotic freedom in parton language.* Nucl. Phys. **B 126**, 298 (1977).

[8] ZEUS Coll., S. Chekanov et al., *Zeus next-to-leading-order qcd analysis of data on deep inelastic scattering.* Phys. Rev. **D 67**, 012007 (2003), hep-ex/0208023.

[9] J. Pumplin et al., *New generation of parton distributions with uncertainties from global QCD analysis.* Preprint hep-ph/0201195, 2002.

[10] E. Laenen et al., *Complete $\mathcal{O}(\alpha_s)$ corrections to heavy flavor structure functions in electroproduction.* Nucl. Phys. **B 392**, 162 (1993).

[11] L. Gladilin, *Charm hadron production fractions.* Preprint hep-ex/9912064, 1999.

[12] Particle Data Group, D.E. Groom et al., *Review of particle physics.* Eur. Phys. J. **C 15**, 1 (2000).

[13] S.E.S. Schagen, *Charm in the proton, an analysis of charm production in deep inelastic scattering.* Ph.D. Thesis, University of Amsterdam, 2004.

[14] C. Peterson et al., *Scaling violations in inclusive e^+e^- annihilation spectra.* Phys. Rev. **D 27**, 105 (1983).

[15] Chekanov, S. and others, *Measurement of d*+- production in deep inelastic e+- p scattering at hera.* Phys. Rev. **D69**, 012004 (2004), hep-ex/0308068.

[16] ZEUS Coll., J. Breitweg et al., *Measurement of open beauty production in photoproduction at HERA.* Eur. Phys. J. **C 18**, 625 (2001), hep-ex/0011081.

[17] Chekanov, S. and others, *Measurement of beauty production in deep inelastic scattering at hera* (2004), hep-ex/0405069.

[18] Tiecke, H., *Status of HERA and the experiments H1 and ZEUS.* 1992. Prepared for 12th International Conference on Physics in Collision, Boulder CO, 10-12 Jun 1992.

[19] ZEUS Coll., U. Holm (ed.), *The ZEUS Detector.* Status Report (unpublished), DESY, 1993, available on `http://www-zeus.desy.de/bluebook/bluebook.html`.

[20] M. Derrick et al., *Design and construction of the ZEUS barrel calorimeter.* Nucl. Inst. Meth. **A 309**, 77 (1991);
A. Andresen et al., *Construction and beam test of the ZEUS forward and rear calorimeter.* Nucl. Inst. Meth. **A 309**, 101 (1991);
A. Caldwell et al., *Design and implementation of a high-precision readout system for the ZEUS calorimeter.* Nucl. Inst. Meth. **A 321**, 356 (1992);
A. Bernstein et al., *Beam tests of the ZEUS barrel calorimeter.* Nucl. Inst. Meth. **A 336**, 23 (1993).

[21] The ZEUS Collaboration, *A Straw-Tube Tracker for ZEUS*, 1998. ZEUS-98-046.

[22] H. Uiterwaal, *The Global Second Level Trigger for ZEUS.* Ph.D. Thesis, University of Amsterdam, 1992.

[23] S.M. Fisher and P. Palazzi, *ADAMO Programmers Manual - Version 3.2.* CERN ECP and RAL, available on
`http://adamo.web.cern.ch/Adamo/programmers_manual/TOC_of_adamo.html`.

[24] R. Brun et al., GEANT3, Technical Report CERN-DD/EE/84-1, CERN, 1987.

[25] K. J. Gaemers and M. van der Horst, *The process $e^- p \to \gamma\ e^- p$ as a fast luminosity monitor for the hera collider.* Nucl. Phys. **B 316**, 269 (1989).

[26] J. Andruszków et al., *Luminosity measurement in the ZEUS experiment.* Acta Phys. Pol. **B 32**, 2025 (2001).

[27] ZEUS background working group, *Study of beam-induced backgrounds in the ZEUS detector from 2002 HERA running*, 2002. ZEUS-02-018;
ZEUS background working group. *Addendum - Study of beam-induced backgrounds in the ZEUS detector from 2002 HERA running*, 2002. ZEUS-02-020;
ZEUS background working group, *Addendum - Study of beam-induced backgrounds in the ZEUS detector from 2002 HERA running*, 2002. ZEUS-02-027.

[28] J.J. Velthuis, *Radiation hardness of the ZEUS MVD frontend chip and Strangeness production in ep scattering at HERA.* Ph.D. Thesis, University of Amsterdam, 2003.

[29] The ZEUS Collaboration, *A Microvertex Detector for ZEUS*, 1997. ZEUS-97-006.

[30] D. Dannheim et al., *Design and tests of the silicon sensors for the zeus micro vertex detector.* Preprint DESY-02-215 (hep-ex/0211026), DESY, 2002.

[31] E. Maddox, *A Kalman filter track fit for the MVD system test data.* 2002. ZEUS-02-001.

[32] T. Fusayasu and K. Tokushuku, *Analog readout modules for the ZEUS microvertex detector.* Nucl. Inst. Meth. **A 436**, 281 (1999).

[33] M. Sutton, C. Youngman, *The Global Tracking Trigger System and Architecture*, 1999. ZEUS-99-074.

[34] A. Polini, M. Sutton, S. Topp-Jorgensen, *The CTD-MVD Global-Tracking-Trigger Interface*, 1999. ZEUS-99-034.

[35] R. Hall-Wilton, M.R. Sutton, B.J. West, *The CTD-BMVD version 3.3 Global Tracking Trigger Algorithm and Performance*, 2001. ZEUS-01-039.

[36] Garfagnini, A. and Kotz, U., *The assembly of the silicon modules for the zeus micro vertex detector.* Nucl. Instrum. Meth. **A461**, 158 (2001).

[37] Matsushita, T. and Boogert, S. and Devenish, R. and Walczak, R., *Optical alignment system for the zeus micro vertex detector.* Nucl. Instrum. Meth. **A466**, 383 (2001).

[38] R.E. Kalman, *A new approach to linear filtering and prediction problems.* Transactions of the ASME- Journal of Basic Engineering **82**, 35 (1960).

[39] R. Frühwirth, *Application of kalman filtering to track and vertex fitting.* Nucl. Inst. Meth. **A 262**, 444 (1987).

[40] P. Avery, *Applied Fitting Theory V, Track Fitting Using the Kalman Filter*, 1992, available on `http://www.phys.ufl.edu/~avery/fitting.html`.

[41] E.N. Koffeman, for the ZEUS MVD group, *A silicon micro vertex detector for the ZEUS experiment*, Nucl. Inst. Meth. **A 453**, 89 (2000).

[42] E. Maddox, *A Kalman filter track fit for the ZEUS microvertex detector*, 2003, ZEUS-03-008.

[43] G.F. Hartner, *VCTRAK(3.07/04): Offline Output Information* (unpublished), ZEUS-97-064, internal ZEUS-note, 1997.

[44] G. F. Hartner, *VCTRAK Briefing: Program and Math* (unpublished), Zeus-98-058, internal ZEUS-note, 1998.

[45] P. Billoir and S. Qian, *Fast vertex fitting with a local parametrization of tracks*, Nucl. Inst. Meth. **A 311** (1992).

[46] R. Frühwirth, M. Regler, R.K. Bock, H. Grote, D. Notz, *Data Analysis Techniques for High-Energy Physics, Second Edition*, Cambridge Monographs on Particle Physics, Nuclear Physics and Cosmology, Vol. 11, Cambridge University Press, 2000.

[47] Bauerdick, L. A. T. and others, *Beam test of silicon strip sensors for the zeus micro vertex detector*, Nucl. Instrum. Meth. **A501**, 340 (2003), hep-ex/0212037.

[48] Bloch, Ingo, *The ZEUS micro-vertex detector system test: Triggering and data analysis*, 2002, DESY-THESIS-2002-001.

[49] J. Straver, *Design, Construction and Beam Tests of the High Resolution Uranium Scintillator Calorimeter for ZEUS*, Ph.D. Thesis, University of Amsterdam, 1991.

[50] T. Kohno, private communication, 2003.

[51] R. Hall-Wilton et al., *The CTD Tracking Resolution* (unpublished), ZEUS-99-024, internal ZEUS-note, 1999.

[52] ZEUS Coll., S. Chekanov et al., *Measurement of the neutral current cross-section and F_2 structure function for deep inelastic e^+p scattering at HERA*, Eur. Phys. J. **C 21**, 443 (2001), hep-ex/0105090.

[53] S. Bentvelsen, J. Engelen and P. Kooijman, *Reconstruction of (x, Q^2) and extraction of structure functions in neutral current scattering at HERA*, in *Proc. Workshop on Physics at HERA*, eds. W. Buchmüller and G. Ingelman, Vol. 1, p. 23, Hamburg, Germany, DESY, 1992;
K.C. Höger, *Measurement of x, y and Q^2 in neutral current events*, in *Proc. Workshop on Physics at HERA*, eds. W. Buchmüller and G. Ingelman, Vol. 1, p. 43, Hamburg, Germany, DESY, 1992.

Summary

The HERA collider stores protons and electrons. The protons can be accelerated up to an energy of 920 GeV and the electrons to 27.5 GeV. The electron-proton (ep) collisions take place in the centre of the ZEUS and H1 experiment.

One of the main topics studied at HERA is the structure of the proton. Analysis of the proton structure functions results in the so called parton (quark or gluon) density functions.

In ep collisions heavy quarks, named charm (c) and bottom (b) are produced. The production process is known as boson gluon fusion: $\gamma g \rightarrow c\bar{c}$ (for charm quarks). The photon (γ) is exchanged between the electron and the proton. The gluon (g) originates from the proton.

Calculations for heavy quark production are done with perturbative quantum chromo dynamics (pQCD). To extend these calculations into cross section predictions one has to rely on the parton density functions. The measurement of heavy quark production, is not only a test for QCD, but also explores the parton densities functions, in particular the gluon density.

Measurements of c and b quark production have been done with the HERA-I data sample (from the years 1995 to 2000). The measurements agree with the predictions, however the measurement uncertainties are still large. The heavy quark measurements can profit from the HERA luminosity (collision rate) upgrade. The HERA collider was upgraded during the summer of 2000.

The luminosity upgrade plan was based on an increase of the particle beam currents and the installation of new focusing magnets inside the ZEUS and H1 experiment. The expected improvement for HERA-II was at least a factor five.

During the preparations for HERA-II the ZEUS collaboration decided to upgrade the detector by building and installing a silicon microvertex detector (MVD). The aim was to improve the tracking and vertexing. With this detector it is possible to select charm and bottom decays by identifying decays which are separated by a few hundred μm from the ep collision point.

The MVD supports 712 single sided silicon strip detectors (sensors). In the barrel MVD (BMVD) 600 silicon sensors (with size 6.4 cm × 6.4 cm × 300 µm) are mounted in three layers around the beam pipe. The closest position measurement to the interaction point has been reduced from 18 cm (most inner layer central tracking detector (CTD)) to 4 cm. In the forward MVD (FMVD) 112 wedge shaped sensors are mounted on 4 disks. Each sensor can measure the position of a charged particle with a precision of 10 µm in the direction perpendicular to the strips.

Information from hits is combined to reconstruct tracks. These tracks can later be used to reconstruct the primary vertex and to find the secondary decays.

The startup of HERA-II was delayed because of many different beam related background problems. The first two years were lost in understanding and solving these problems. In October 2003 luminosity running started. Up to April 2004 a data sample of $10\,\mathrm{pb}^{-1}$ was recorded. This is a small sample in comparison with the $100\,\mathrm{pb}^{-1}$ recorded during HERA-I.

In this thesis the MVD and its performance are described in detail. A special fit algorithm has been developed to reconstruct the tracks and is based on the Kalman filter method. If the track has traversed material, multiple scattering corrections are performed. For low momentum tracks the impact parameter resolution improves significantly when these corrections are done.

After assembly and before installation the MVD was tested extensively with cosmic rays. Analysis of this cosmic ray sample showed that from the 600 barrel MVD sensors 586 were working properly. The average hit finding efficiency was 97.7%.

Cosmic rays tests were also done after installation inside ZEUS. From these data the impact parameter resolution was estimated. After the MVD geometry was calibrated, the estimated impact parameter resolution is $0.083/p_t + 0.047\,\mathrm{mm}$.

From Monte Carlo simulation of the MVD, it was shown that the track and hit finding is very efficient ($> 99\%$ in the MVD barrel region). The simulated track impact parameter resolution is $0.056/p_t + 0.018\,\mathrm{mm}$. This can be considered as the best reachable impact parameter resolution. Hence, improvements can still be made especially in the hit position reconstruction and the geometry calibration of the MVD.

This thesis ends with a look at the first HERA-II data. The decay of $D^{*\pm}$ and $D^{\pm}$ mesons have been studied. For the first time secondary vertices arising from the decay of charm mesons have been seen in ZEUS. The MVD will be a powerful tool in the future analysis of heavy quark production.

Samenvatting

HERA is een opslagring voor protonen en elektronen. De protonen kunnen versneld worden tot een energie van 920 GeV en de elektronen tot een energie van 27.5 GeV. Botsingen tussen de elektronen en protonen (ep-botsingen) vinden plaats in het centrum van het ZEUS en het H1 experiment.

Eén van de belangrijkste onderwerpen, die bij HERA bestudeerd worden, is de structuur van het proton. De analyse van de structuurfuncties van het proton resulteert in zogenaamde parton- (quark- of gluon-) dichtheidsfuncties.

In ep-botsingen worden zware quarks geproduceerd. Dit zijn c "charm" en b "bottom" quarks. Het productieproces staat bekend als boson-gluonfusie: $\gamma g \rightarrow c\bar{c}$ (voor charm quarks). Het foton (γ) wordt uitgewisseld tussen het elektron en proton. Het gluon (g) is afkomstig uit het proton.

Berekeningen voor de productie van zware quarks worden gemaakt met perturbatieve quantumchromodynamica (pQCD). Om de botsingsdoorsnede te voorspellen moet men de partondichtheidsfuncties vertrouwen. Het meten van de productie van zware quarks is niet alleen een test van QCD, maar ook een kans om meer te begrijpen van de partondichtheidsfuncties, in het bijzonder de gluondichtheid.

Metingen van c en b quarkproductie zijn gedaan met de HERA-I gegevens (afkomstig uit de jaren 1995 tot 2000). Hoewel deze metingen in overeenstemming zijn met de voorspellingen, zijn de onzekerheden van de metingen nog groot. De zware quark metingen kunnen profiteren van de verhoging van de HERA luminositeit (botsingsfrequentie). Tijdens de zomer van 2000 is de HERA botser verbeterd.

Het luminositeitsverhogingsproject was gebaseerd op het vergroten van de deeltjesstromen en de installatie van nieuwe focusseringsmagneten binnenin de ZEUS en H1 experimenten. De verwachte toename in luminositeit voor HERA-II was tenminste een factor vijf.

Tijdens de voorbereidingen op HERA-II besloot de ZEUS collaboratie om de detector te verbeteren met het bouwen en installeren van een nieuwe silicium microvertex detector (MVD). Het doel was om de spoor- en vertexreconstructie beter te maken. Met deze detector moet het mogelijk zijn om "charm" en "bottom" vervallen te selecteren door het identificeren van vervallen die slechts enkele honderden μm van het botsingspunt gescheiden zijn.

De MVD voorziet in 712 enkelzijdige silicium strip detectoren (sensoren). In de centrale ("barrel") MVD (of BMVD) zijn 600 silicium sensoren (met een afmeting van $6.4\,\text{cm} \times 6.4\,\text{cm} \times 300\,\mu\text{m}$) gemonteerd in drie lagen rond de bundelpijp. Het meest nabije meetpunt tot het interactiepunt is gereduceerd van 18 cm (binnenste laag van de centrale

sporenkamer) tot 4 cm. In de voorwaartse ("forward") MVD (of FMVD) zijn 112 wigvormige sensoren gemonteerd op 4 schijven. Elke sensor kan de positie van een geladen deeltje meten met een precisie van 10 µm in de richting loodrecht op de strips.

Om de sporen te reconstrueren wordt de informatie van de voltreffers ("hits") gecombineerd. Deze sporen kunnen later gebruikt worden on de primaire vertex te reconstrueren en om secundaire vervallen te vinden.

De aanvang van HERA-II was vertraagd vanwege de vele verschillende, aan de deeltjesbundels gerelateerde achtergrondproblemen. De eerste twee jaren waren verloren aan het begrijpen en oplossen van deze problemen. Luminositeitslevering begon in oktober 2003. Tot en met april 2004 werd $10\,\mathrm{pb}^{-1}$ aan meetgegevens opgeslagen. Dit is slechts een klein deel in vergelijking met de $100\,\mathrm{pb}^{-1}$ die tijdens HERA-I verzameld was.

In dit proefschrift worden de MVD en zijn prestaties uitgebreid beschreven. Een speciaal fit-algoritme was ontwikkeld om de sporen te reconstrueren en is gebaseerd op de Kalman filter methode. Als een spoor materiaal heeft doorkruist, dan wordt de verstrooiings- "multiple scattering" bijdrage berekend. De impactparameterresolutie verbetert significant voor sporen met lage impuls, wanneer deze bijdragen worden gebruikt in de fit.

Na het bouwen en voor de installatie werd de MVD uitgebreid getest met kosmische stralen. Analyse van deze kosmische stralen toont aan dat van de 600 BMVD sensoren er 586 naar behoren werkten. De gemiddelde efficiëntie om een hit te vinden was 97.7%.

Met de ZEUS-detector worden ook regelmatig kosmische stralen gemeten. Met deze meetgegevens werd een schatting gemaakt van de impactparameterresolutie. Nadat de geometrie van de MVD gekalibreerd was, is de geschatte impactparameterresolutie als functie van de transversale impuls $0.083/p_t + 0.047\,\mathrm{mm}$.

Met behulp van de Monte Carlo simulatie van de MVD werd aangetoond dat de sporen en treffers zeer efficiënt gevonden worden ($> 99\%$ in de centrale MVD). In de simulatie is de impactparameter-resolutie van de sporen $0.056/p_t + 0.018\,\mathrm{mm}$. Dit kan beschouwd worden als de best haalbare impactparameterresolutie. Er zijn dus nog verbeteringen mogelijk, in het bijzonder in de reconstructie van de positie van de treffers en in de kalibratie van de geometrie van de MVD.

Dit proefschrift eindigt met een beschouwing van de eerste HERA-II meetgegevens. Het verval van $D^{*\pm}$ en $D^{\pm}$ mesonen zijn bestudeerd. Voor het eerst zijn bij ZEUS secundaire vertexen gezien die afkomstig zijn van het verval van charm-mesonen. De MVD zal een krachtig middel zijn in de toekomstige analyse van de productie van zware quarks.

Acknowledgements

The work presented in this thesis would never have been accomplished without the help, support and company of many people, both at NIKHEF in Amsterdam and at DESY in Hamburg, where I have spent a large part of my PhD period.

I want to thank Henk Tiecke and Els Koffeman for involving me in every detail of the microvertex detector (MVD) project. They always worked with enthusiasm and determination on this complex project. It was nice to be a member of the MVD team. Els Koffeman also provided me the survey measurements of the MVD geometry, which I have used in this thesis.

The idea to write a Kalman filter trajectory fit for the MVD came from Paul Kooijman. I am grateful to Paul Kooijman for supporting me in this project, especially when I got stuck sometimes. The result is a computer program (kfrecon), which is written in c++. I appreciated very much the assistance of Enrico Tassi. Without his help the fitting program would not have worked together with the rest of the ZEUS software (which is in FORTRAN).

The first step towards alignment with tracks of the MVD was made by Takanori Kohno. When I used his calibration constants the MVD tracking performance improved a lot.

For the data analysis I worked together with Richard Hall-Wilton and John Loizides. They supported me in the analysis of the new HERA data, which came in much slower than expected. They were always happy to answer my questions regarding the D meson analysis.

When I was in Hamburg I enjoyed the company of my friends, especially: Damir Lelas, John Loizides, James Ferrando, Hernan Wahlberg, Antonello Sbrizzi, Ingo Bloch and Oliver Gutsche.

It was always a pleasure to work in the NIKHEF ZEUS group. I want to thank the following people for their company: Niels Tuning, Clemens Bokel, Jaap Velthuis, Sjors Grijpink, Sven Schagen, Enrico Tassi, Monica Vazquez, Nicola Coppola, Gabriel Grigorescu and Avraam Keramidas.

I want to thank my promoter Jos Engelen and co-promoter Els Koffeman for their support and many suggestions, which have improved this thesis greatly.

Verder wil ik mijn familie en vrienden bedanken voor hun gezelschap en interesse. Vooral mijn ouders ben ik dankbaar voor hun onvoorwaardelijke steun. Tenslotte wil ik Pauline bedanken voor haar steun en geduld.